UNIVERSIDAD NACIONAL AUTÓNOMA DE MÉXICO

DIVISIÓN DE ESTUDIOS DE POSGRADO
FACULTAD DE INGENIERÍA

“OPTIMACIÓN DEL MÉTODO INDIRECTO DE ELEMENTOS EN LA FRONTERA, APLICADO AL ESTUDIO DE LA PROPAGACIÓN DE ONDAS SÍSMICAS EN CONFIGURACIONES IRREGULARES”

T E S I S

Q U E P R E S E N T A

SOTERO ALEJANDRO GIL ZEPEDA

PARA OBTENER EL GRADO DE:

DOCTOR EN INGENIERÍA
(MECÁNICA DE SUELOS)

DIRECTOR DE TESIS

DR. FRANCISCO JOSÉ SÁNCHEZ SESMA

MÉXICO, D. F. **2005**

Agradecimientos

Quiero expresar mi sincero agradecimiento a todas aquellas personas de quienes he recibido su apoyo en todos los aspectos, en las ideas, consejos y sugerencias para el desarrollo de este trabajo.

Al director y asesor de los trabajos de investigación, Dr. Francisco José Sánchez Sesma, por sus enseñanzas y exigencias en el desarrollo de esta tesis, así como a los demás miembros del jurado doctoral Dr. Luís Esteva Maraboto, Dr. Javier Avilés López, Dr. Mario Gustavo Ordaz Schroeder, Dra. Sonia Elda Ruiz Gómez, Dr. Eduardo Reinoso Angulo y Dr. Efraín Ovando Shelley.

Al Dr. Francisco Luzón Martínez por haberme brindado la oportunidad de poder trabajar con él en la Universidad de Almería en España, en donde se aplicaron los trabajos de investigación realizados en el Instituto de Ingeniería de la UNAM.

A mis padres por haberme enseñado la disciplina y el ímpetu para lograr buenos objetivos. A Gretchen Gil de quien he aprendido a entender un poco de la naturaleza de la vida marina, motivándome a admirar a los primeros seres vivos que habitaron la tierra. A Dafne Gil que a pesar de su corta edad me ha enseñado a trabajar con ahínco.

Índice

Introducción

En todos los sismos las características locales, topográficas y geológicas del suelo repercuten en las condiciones espécificas del movimiento del mismo, tales como los efectos de sitio que producen variaciones especiales creando grandes movimientos y concentrar el daño severo en ciertas zonas. En los últimos años se han realizado esfuerzos significativos que han ayudado a entender tales efectos (Sánchez-Sesma, 1987; Aki, 1988; Luco et al, 1990; Sánchez-Sesma and Luzón, 1995; Sánchez-Sesma, 1996; Olsen and Archuleta, 1996; Olsen, 2000).

Se han propuesto varios métodos para estudiar la propagación de las ondas sísmicas en valles aluviales en 3D, tal es el caso del método indirecto de elementos en la frontera (IBEM por sus siglas en inglés *Indirect Boundary Elements Method*), **que permite obtener resultados tan confiables como para entender y poder calibrar otros procedimientos. Se ha logrado hacer simulaciones realistas con otros métodos, tal es el caso de las diferencias finitas. El estudio de Frankel, 1993, de la respuesta del valle de San Bernardino y de Olsen, 1995, en la ciudad de los Angeles, California.**

En este trabajo se presenta el método indirecto de elementos en la frontera 3D (IBEM) por vez primera aplicado a configuraciones completamente irregulares, haciendo factible la solución de problemas realistas y se hace énfasis en la optimación numérica con un ahorro sustancial en los procesos de cómputo tanto en velocidad de solución como en el ahorro en de memoria RAM, pudiendo resolver problemas de mayor tamaño o alcanzar la respuesta sísmica a una mayor frecuencia, ver Gil-Zepeda et al., 2002; F. Luzón et al., 2004.

En el capítulo 3 se presentan las ecuaciones del método indirecto de elementos en la frontera. En el capítulo 4 se dan los procedimientos y ecuaciones utilizadas para la discretización geométrica, como parte fundamental para poder automatizar la solución de problemas realistas, ya que en los trabajos de aplicación de los apendices A y B, la discretización geométrica en ambos casos es dinámica y se calcula con base en la variación de la frecuencia; este efecto de mallado dinámico en la discretización es también parte importante de

la optimación. En el capítulo 5 se tiene la formulación para la solución de las ecuaciones integrales utilizando el método de condensación estática de matrices de acuerdo con el arreglo de la estructura de la matriz por medio de bloques tratado en este capítulo. En los apéndices A, B y C se ofrecen algunos ejemplos de aplicación.

Capítulo 1

1. Propagación de ondas en un medio elástico

La solución a la ecuación diferencial que gobierna el movimiento ondulatorio en un sólido elástico fue presentada por S. D. Poisson en 1828, descomponiendo el desplazamiento en una parte irrotacional y una equivolumétrica.

En la descripción de la propagación de ondas elásticas en un medio continuo, elástico, homogéneo e isótropo, debe considerarse la ecuación de Navier, en ausencia de fuerzas de volumen, como:

$$\boldsymbol{\mu}\nabla^2\vec{\boldsymbol{u}} + (\boldsymbol{\lambda}+\boldsymbol{\mu})\nabla(\nabla\cdot\vec{\boldsymbol{u}}) = \boldsymbol{\rho}\frac{\partial^2\vec{u}}{\partial t^2} \tag{1}$$

Donde ∇ es el operador gradiente, $\boldsymbol{\lambda}$ y $\boldsymbol{\mu}$ son las constantes de Lamé, $\boldsymbol{\rho}$ es la densidad de masa y $\boldsymbol{u}$ es el campo de desplazamientos.

Es posible demostrar que, para un campo vectorial $\vec{\boldsymbol{A}}$ cualquiera, se verifica el teorema de Helmholtz:

$$\nabla^2\vec{\boldsymbol{A}} = \nabla(\nabla\cdot\vec{\boldsymbol{A}}) + \nabla\times(\nabla\times\vec{\boldsymbol{A}}) \tag{2}$$

Entonces, considerando que el campo de desplazamientos u también cumple dicho teorema, de la anterior ecuación se puede expresar nuevamente la ecuación de Navier como:

$$(\boldsymbol{\lambda}+\boldsymbol{2\mu})\nabla(\nabla\cdot\tilde{\mathbf{u}}) + \boldsymbol{\mu}\nabla\times(\nabla\times\tilde{\mathbf{u}}) = \boldsymbol{\rho}\frac{\partial^2\vec{u}}{\partial t^2} \tag{3}$$

Si suponemos ahora que el desplazamiento u se produce sin cambio de volumen, entonces su divergencia es cero y la ecuación de Navier queda como:

$$\begin{aligned}\nabla^2\tilde{\mathbf{u}} &= \frac{1}{\beta^2}\frac{\partial^2\vec{u}}{\partial t^2} \\ \nabla\cdot\vec{\boldsymbol{u}} &= \mathbf{0}\end{aligned} \tag{4}$$

Donde $\beta = \sqrt{(\mu/\rho)}$, es la velocidad de propagación de las ondas equivolumétricas o cortantes. En esta ecuación el vector de desplazamientos es perpendicular al vector normal al frente de onda. Este tipo de ondas recibe el nombre de ondas S, cortante o de cizalla. Por conveniencia, las ondas S se suelen dividir en dos tipos, ambas contenidas en el plano perpendicular a la dirección de la onda. Las ondas polarizadas en el plano horizontal perpendicular a la dirección vertical se definen como ondas SH, y como SV las paralelas al plano vertical. Para clarificar estos conceptos, en la figura 1.1 se muestra la polarización de la onda S en ondas SH y SV en el plano horizontal (plano formado por los ejes $y-z$) y vertical (plano formado por los ejes $x-z$), respectivamente.

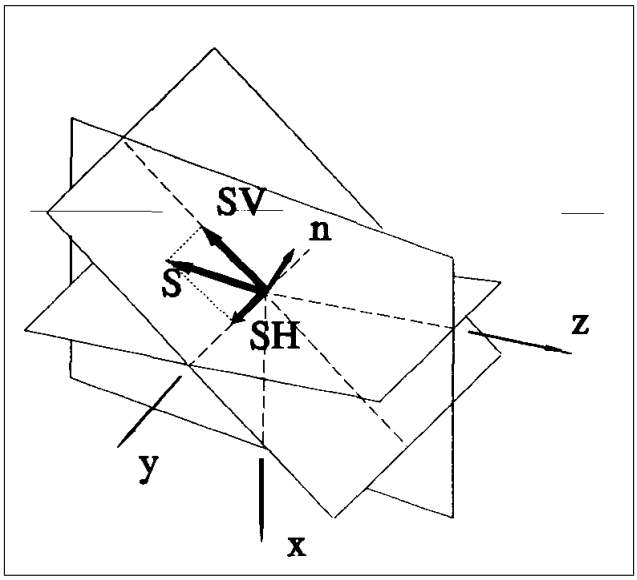

Figura 1.1; Polarización de la onda S

Supongamos ahora que el desplazamiento ocurre sin rotación de partículas, entonces el rotacional del vector desplazamiento es nulo y la ecuación de Navier se convierte en:

$$\nabla^2 \vec{\boldsymbol{u}} = \frac{1}{\alpha^2}\frac{\partial^2 \vec{u}}{\partial t^2} \qquad (5)$$
$$\nabla \times \vec{\boldsymbol{u}} = \mathbf{0}$$

Donde $\alpha = \sqrt{(\lambda + 2\mu)/\rho}$, es la velocidad de propagación de ondas compresionales o irrotacionales u ondas P. En esta ecuación el campo de desplazamientos u es paralelo a la dirección de propagación del frente de ondas. Tanto las ondas P como las S pueden observarse en los registros del movimiento del suelo ocurridos durante un terremoto.

Cuando una determinada zona está formada por la superposición de estratos con diferentes propiedades elásticas, los efectos locales que se producen ante la incidencia de ondas sísmicas se pueden estimar haciendo uso de modelos unidimensionales. Estos modelos representan normalmente un conjunto de capas planas situadas sobre un semiespacio en las que se puede hacer incidir ondas elásticas P y S. De particular interés es el método de Thompson-Haskell (Thompson, 1950; Haskell, 1953). Esta técnica fue ideada inicialmente para estudiar la propagación de ondas superficiales en medios estratificados. Este método puede englobarse dentro de la técnica que hace uso de los propagadores matriciales introducida a la sismología por Gilbert y Backus (1966), válida para cualquier tipo de onda. En el método se utiliza una matriz de propagación en la que están implícitas las condiciones de continuidad de los esfuerzos y desplazamientos en la superficie de separación de dos estratos y la condición de esfuerzos nulos en la superficie libre. Esta técnica se ha utilizado en innumerables ocasiones desde su aparición (p.e. Ordaz et al., 1992; Luzón 1992; Luzón et al., 1994), aportando una primera aproximación sobre la respuesta sísmica de un determinado lugar.

Sin embargo, en muchos casos de interés, las estructuras superficiales contienen discontinuidades laterales que pueden producir variaciones espaciales importantes del movimiento del suelo que modifican de forma drástica la respuesta sísmica del lugar.

Este tipo de efectos locales se han tratado como un problema de difracción de ondas elásticas. En este sentido se han desarrollado en las últimas décadas distintas técnicas analíticas y numéricas para la estimación de la respuesta sísmica en configuraciones geológicas complejas. La flexibilidad y versatilidad de estas técnicas se han incrementado al mismo tiempo que el desarrollo de los sistemas de cómputo, lo que ha permitido estudiar estructuras cada vez más realistas.

1.1. Difracción de ondas elásticas por irregularidades superficiales

La difracción es un fenómeno que caracteriza al movimiento ondulatorio que se presenta cuando en el camino que recorre la onda, cualquiera que sea su naturaleza, se encuentran obstáculos o aberturas con dimensiones comparables a sus longitudes de onda. De acuerdo con el principio de Huygens, los bordes del obstáculo actúan como fuentes de ondas secundarias propagándose en todas las direcciones. Así, las ondas difractadas pueden llegar a las zonas de sombra que son inaccesibles cuando se considera la propagación rectilínea de la onda incidente.

Considérese un semiespacio con una irregularidad superficial donde se hace incidir un frente de ondas elásticas como se muestra en la figura 1.2. La irregularidad difractará las ondas incidentes, y el desplazamiento producido por ambas ondas, incidentes más difractadas, deben satisfacer las ecuaciones de Navier y las condiciones de contorno en la superficie. Estas condiciones proporcionan tracciones nulas en la superficie libre. De otro lado, los campos difractados deben verificar la condición de radiación de Sommerfeld (1949), por que no permite la propagación de dichos campos desde el infinito hasta la irregularidad; es decir, las ondas difractadas deben irradiarse desde el difractor.

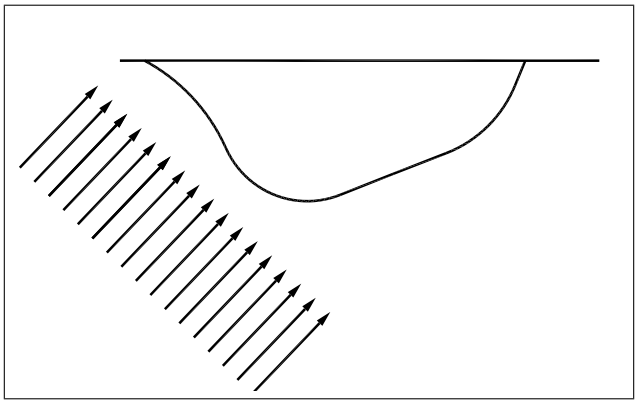

Figura 1.2; Irregularidad superficial e incidencia de ondas elásticas

Considérese ahora un semiespacio E, con una inclusión elástica R, bajo la incidencia de ondas elásticas, como se muestra en la figura 1.3. El movimiento que se produce en la superficie de esta configuración irregular está constituido

por las interferencias de las ondas incidentes con las reflejadas, las difractadas y las refractadas. Es usual considerar el movimiento en el semiespacio como la superposición de las ondas difractadas y las de campo libre:

$$u_i^E = u_i^0 + u_i^d \tag{6}$$

Donde u_i^0 es el desplazamiento de campo libre en la dirección i, es decir, la solución en el semiespacio E en ausencia de la irregularidad. En este caso, los desplazamientos de campo libre son aquellos producidos por el campo incidente más el reflejado.

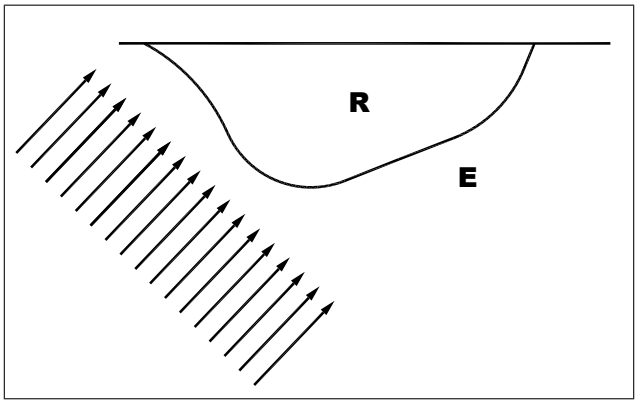

Figura 1.3; Semiespacio E e inclusión R bajo la incidencia de ondas elásticas.

Las condiciones de contorno implican que sobre la superficie libre del semiespacio E las tracciones sean nulas, es decir:

$$\boldsymbol{t_i^0 + t_i^d = 0} \tag{7}$$

Donde t_i^0 y t_i^d son las i-ésimas componentes de las tracciones correspondientes al campo libre y al campo difractado, respectivamente. Las tracciones de campo libre son las que habría en ausencia de irregularidad, por lo que $t_i^0 = 0$. Sobre la superficie libre de la inclusión R debe verificarse además que las tracciones también sean nulas

$$\boldsymbol{t_i^r = 0} \tag{8}$$

Donde t_i^r son las tracciones en la dirección i debidas a las ondas refractadas.

Las condiciones de continuidad de esfuerzos y desplazamientos en la frontera común de E y R implican:

$$\begin{aligned} \boldsymbol{u}_i^0 + \boldsymbol{u}_i^d &= \boldsymbol{u}_i^r \\ \boldsymbol{t}_i^0 + \boldsymbol{t}_i^d &= \boldsymbol{t}_i^r \end{aligned} \tag{9}$$

Las anteriores condiciones de contorno serán utilizadas más adelante, cuando se muestre la representación integral que se utiliza en esta tesis para los campos del desplazamiento. A continuación se da una revisión de los métodos que más se han usado para estimar la respuesta sísmica de irregularidades geológicas superficiales.

Capítulo 2

2. Soluciones numéricas en la propagación de ondas elásticas

A continuación se muestra una breve descripción sobre las técnicas numéricas que más aceptación han tenido en el estudio de la difracción de ondas elásticas, y se citarán las contribuciones más relevantes en este tipo de problemas.

Para hacer esta revisión se han distinguido tres grupos de métodos:

a) Métodos de dominio.

b) Teoría de rayos y haces gaussianos.

c) Métodos de contorno.

Otras revisiones del tema se pueden encontrar por ejemplo en los trabajos de Sánchez-Sesma (1987), Aki (1988) y Luco et al., (1990).

2.1. Métodos de dominio

En esta clase de esquemas numéricos, también llamados métodos directos, se propagan los campos de onda completos a través de un medio resolviendo aproximadamente la ecuación de onda o las ecuaciones de la elastodinámica, normalmente en intervalos de tiempo sucesivos. Estas técnicas se pueden clasificar en tres tipos:

a) Método de diferencias finitas.

b) Método pseudoespectral.

c) Método de elementos finitos.

Estos tipos de aproximaciones tienen un gran potencial ya que permiten el tratamiento de estructuras complejas. Las desventajas, sin embargo, también son importantes debido al excesivo tiempo y memoria que se requieren durante el cómputo.

2.1.1. Método de diferencias finitas

El método de diferencias finitas se ha usado con éxito en las últimas décadas para estudiar la propagación de ondas en medios elásticos (Alterman y Karal,

1968; Soore, 1972; Kelly et al., 1976). En esta técnica, las ecuaciones diferenciales que gobiernan el movimiento son reemplazadas por un conjunto de ecuaciones recursivas expresadas en forma de diferencias finitas. Una vez que el espacio es discretizado formando una rejilla regular, se calcula la solución en cada nodo de la rejilla en sucesivos intervalos de tiempo.

Boore (1972), usó este esquema para estudiar la propagación de ondas SH sobre una montaña. Boore et al., (1981), modelaron la respuesta de una irregularidad superficial en forma de escalón vertical bajo la incidencia de ondas P y S. Estos autores observaron que ambos tipos de ondas generaban ondas de Rayleigh, y las que aparecían con la incidencia de ondas S tenían una mayor amplitud que las producidas con ondas P. Harmsen y Harding (1981), calcularon la respuesta de una cuenca sedimentaria para la incidencia de ondas P y SV y encontraron resultados muy interesantes sobre la generación de ondas superficiales en las irregularidades laterales. En todos estos casos se trataron estructuras con geometría bidimensional. Frankel (1993), realizó una simulación, considerando una geometría tridimensional del movimiento del suelo en el Valle de San Bernardino, California, bajo los efectos de una fuente sísmica situada en Loma Prieta. Esta técnica muestra gran capacidad y robustez; sin embargo, el elevado costo en tiempo de cálculo y en uso de memoria limitan su uso, haciéndola en muchas ocasiones inviable, especialmente cuando se quieren estudiar estructuras de grandes dimensiones sobre un ancho rango de frecuencias y tiempos.

2.1.2. Método pseudoespectral

En esta técnica, también llamada de Fourier (Kosloff y Baysal, 1982), las derivadas espaciales de las ecuaciones diferenciales son evaluadas usando la transformada rápida de Fourier a lo largo de un renglón o columna de la rejilla espacial en un tiempo dado, y las derivadas temporales se calculan usando el método de diferencias finitas. Para diferenciar con respecto a las coordenadas espaciales, el renglón o columna es transformado al dominio del número de onda k (o frecuencia espacial); la multiplicación por ik, donde i es la unidad imaginaria y su transformación inversa, producen la correspondiente derivada espacial.

Para obtener buenos resultados, se requieren pocos puntos en la rejilla por longitud de onda (del orden de 4 ó 5, Fäh, 1992), lo que ha permitido el análisis de topografías bidimensionales (Tessmer et al., 1992) y tridimensionales (Reshef et al.,1988). Un trabajo para el estudio de cuencas sedimentarias es el de Ávila et al., (1993). Estos autores calculan los sismogramas sintéticos en la superficie de un valle aluvial ante la incidencia de ondas elásticas SH. Para ello, hacen una expansión multi-modal analítica que controla la variación vertical del campo asociado a la ecuación de onda.

2.1.3. Método de elementos finitos

En este método, el espacio considerado es dividido en elementos y el desplazamiento se calcula en los nodos de los mismos, donde también se aplican las fuerzas que intervienen en el problema. Una de las ventajas de esta técnica es que los elementos no tienen porqué ser iguales ni en tamaño ni en forma. Así, es posible disponer de varias regiones diferenciadas según interese en cada problema en particular. Una vez que se ha dividido el espacio, el desplazamiento en cada nodo se relaciona con las fuerzas aplicadas mediante el sistema de ecuaciones diferenciales. La integración de este sistema se puede realizar con varios esquemas. Serón et al., (1990), estudiaron cinco formas distintas desde el punto de vista de la exactitud, funcionamiento y necesidades de cada técnica en procesadores escalares y vectoriales con gran capacidad de almacenamiento. Estos autores concluyeron que uno de los métodos de integración más adecuados era el de diferencias centradas (Newmark, 1959), cuando las matrices de masa y amortiguamiento que aparecen en el sistema de ecuaciones son diagonales.

Otra de las ventajas del método de elementos finitos es la posibilidad de calcular la respuesta en configuraciones con comportamientos del suelo no lineales (Joyner y Chen, 1975; Joyner, 1975). Se ha usado para modelar estructuras tridimensionales (Toshinawa y Ohmachi, 1992; Li et al., 1992; Rial et al., 1992).

Por otro lado, la técnica presenta algunas limitaciones, ya que conforme se quiere conocer la respuesta para frecuencias más altas, es necesario dividir el espacio en más elementos, incrementando por tanto, el tiempo y la memoria de cómputo. Para evitar este problema se suele reducir el espacio imponiendo

fronteras artificiales; sin embargo, los análisis en el tiempo para estos casos deben ser acortados para evitar las reflexiones artificiales que las ondas sufren en dichas fronteras.

2.2. Teoría de rayos y haces Gaussianos

Existen algunos casos en los que el problema de la propagación de ondas se simplifica y se puede usar la técnica geométrica o de rayos. En estos métodos se realizan expansiones asintóticas para la longitud de onda $\lambda = 0$, es decir para frecuencias muy grandes. Este análisis contiene dos estados (Hanyga et al., 1985):

a) Encontrar los caminos que recorre la señal, es decir los rayos.

b) Encontrar la intensidad de la señal que se propaga a lo largo de cada rayo.

Con el uso de esta técnica se han estudiado los campos de ondas para alta frecuencia en estratos de variación lateral (Cerveny, 1985a; Chen, 1992; Pao et al., 1984), y cuencas sedimentarias bidimensionales (Hong y Helmberger, 1977; Jackson, 1971; Rial, 1984). Sánchez-Sesma et al., (1988) presenta una técnica en la que tiene en cuenta la familia completa de rayos en valles con geometría 2D. El caso de una cuenca circular tridimensional ha sido tratado para incidencia de ondas P y S por Lee y Langston (1983).

Por otro lado, en el último decenio se ha usado una extensión de la teoría de rayos basada en la combinación de esta técnica con una aproximación parabólica de la ecuación de onda (Nowack y Aki, 1984). En este esquema el sistema de rayos focoreceptor sirve de soporte para la construcción del campo de ondas. La ecuación de ondas se soluciona en coordenadas centradas, en las que se satisface localmente la aproximación parabólica en el entorno de cada rayo. En esta solución la amplitud de la onda tiene forma gaussiana alrededor del rayo central y la solución final es la superposición de los haces gaussianos correspondientes a cada rayo.

Se han presentado varias aplicaciones de esta técnica para el estudio de la propagación de ondas de alta frecuencia para estructuras bidimensionales (Cerveny y Psencik, 1983; Madariaga, 1984; George et al., 1987; Yomogida,

1985; Álvarez et al., 1989; Rodríguez-Zúñiga, 1992) y es de resaltar el trabajo de Kato et al., (1993), en el que se presentan simulaciones tridimensionales de la propagación de ondas superficiales en la cuenca sedimentaria de Kanto, Japón.

El costo de cómputo de las técnicas de rayos y sus extensiones suele ser bajo en relación a otros métodos; sin embargo, estas aproximaciones presentan otras limitaciones (Cerveny, 1985). Las soluciones que se obtienen no tienen en cuenta el fenómeno de la difracción; además, las fronteras deben ser suaves y las dimensiones de las irregularidades tienen que ser mucho más grandes que la longitud de onda característica de la onda incidente. Los métodos de rayos tampoco pueden tratar los casos de incidencia de ondas inhomogéneas, tales como ondas de Rayleigh ni las ondas reflejadas más allá del ángulo crítico.

2.3. Método de contorno

En los últimos años los métodos de contorno han gozado de gran popularidad y aceptación. En este tipo de técnicas se evita la introducción de fronteras ficticias en el medio, como ocurría con los métodos de dominio, reduciendo así las dimensiones del problema. Este hecho proporciona por lo tanto muchas ventajas durante el cómputo. Estos métodos pueden usarse a la vez con esquemas de elementos finitos (Zienkiewics et al., 1977; Khair et al, 1989; Takemiya y Tomono, 1992; Mossessian y Dravinski, 1992), con lo que la región modelada con dichos elementos puede ser de menor extensión. Los métodos de contorno engloban, principalmente, tres técnicas basadas en:

a) El uso de sistemas completos de soluciones (Herrera, 1981).

b) La representación del número de onda discreto (Aki y Lamer, 1970; Bouchon y Aki, 1977).

c) El uso de ecuaciones integrales (Brebbia, 1978; Cole et al., 1978).

2.3.1. Métodos que usan sistemas completos de soluciones

Estos tipos de métodos están basados en que se puede encontrar la solución de un problema a partir de la combinación lineal de funciones linealmente independientes y cada una de ellas satisface la ecuación diferencial que representa el problema.

Los coeficientes de dicha combinación se calculan mediante la imposición de las condiciones de contorno de cada caso en estudio.

En problemas de propagación de ondas elásticas, las ecuaciones diferenciales que deben considerarse son las de Navier. Las condiciones de contorno implican tracciones nulas en las superficies libres y la continuidad de desplazamientos y tracciones en las superficies de separación de dos medios distintos. Estos requisitos ayudan a encontrar los coeficientes de la combinación lineal de soluciones simples y estos se pueden calcular con un esquema de mínimos cuadrados cuando su número no coincide con el de las condiciones de contorno. Esta técnica se ha utilizado para resolver problemas de difracción elástica debida a cañones (Sánchez-Sesma, 1978; Sabina et al., 1979; Wong, 1982; England et al., 1980; Sánchez-Sesma et al., 1985), cordilleras (Sánchez-Sesma y Esquivel, 1980; Sánchez-Sesma et al., 1982), y cuencas sedimentarias (Sánchez-Sesma y Esquivel, 1979; Dravinski, 1982; Sánchez-Sesma et al., 1988) con varias geometrías bidimensionales y con distintos tipos de onda incidente. Con esta aproximación se han tratado también estructuras tridimensionales (Sánchez-Sesma, 1983; Sánchez-Sesma et al., 1984, 1985, 1989; Pérez-Rocha y Sánchez-Sesma, 1991) con simetría acimutal para la incidencia de ondas P, SV y de Rayleigh.

2.3.2. Método del número de onda discreto

En esta técnica (Aki y Lamer, 1970), el campo de ondas se expresa como una superposición de ondas planas, incluyendo las ondas inhomogéneas, propagándose en todas las direcciones desde la frontera del espacio elástico con amplitudes complejas desconocidas. El movimiento total se obtiene mediante la integración sobre el número de onda horizontal. Esta integral es reemplazada por una suma infinita bajo la hipótesis de periodicidad horizontal de la irregularidad. La truncación de ésta a una suma finita y la aplicación de las condiciones de contorno en el dominio del número de onda, conduce a un sistema de ecuaciones lineales para las amplitudes desconocidas.

Este método ha sido extendido al dominio del tiempo (Bouchon, 1973; Bard y Bouchon, 1980) y se ha estudiado la difracción debida a cañones (Bouchon, 1973), cordilleras (Bouchon, 1973; Bard, 1982; Bard y Tucker, 1985; Geli et

al., 1988), y depósitos sedimentarios (Bard y Bouchon, 1980; Bard y Bouchon, 1985; Bard y Gariel, 1986) con geometría bidimensional bajo la incidencia de distintos tipos de ondas elásticas.

La técnica se ha extendido también a geometrías tridimensionales (Niwa y Hirose, 1985) para distintas formas de cuencas sedimentarias bajo la incidencia de ondas P, S y Rayleigh (Horike et al., 1990; Horike y Takeuichi, 1992; Kuribayashi et al., 1992; Ohori et al., 1992; Uebayashi et al., 1992; Jiang et al., 1993).

Esta técnica se muestra eficiente en el cálculo computacional y expresa correctamente el campo de desplazamientos. Sin embargo, está limitada al estudio de irregularidades de pendiente suave y a frecuencias no muy altas.

2.3.3. Solución con ecuaciones integrales

Este método está basado en el hecho de que el campo de ondas admite una representación integral en términos de elementos sobre las fronteras del espacio considerado. Con la discretización de dicha frontera y con las condiciones de contorno, se genera un sistema lineal de ecuaciones integrales. Hay varias formas de tratar esta aproximación, una de ellas es la formulación directa, llamada así porque las incógnitas del problema son los valores del desplazamiento y las tracciones. Wong y Jennings (1975) y Zhang y Chopra (1991), usaron esta formulación para estudiar la respuesta sísmica de cañones de forma bidimensional y tridimensional, respectivamente. Por otra parte, en la versión indirecta las incógnitas son las densidades de fuerzas y momentos en cada elemento-fuente.

Esta técnica se ha combinado con el método del número de onda discreto, que se ha usado para calcular las funciones de Green que aparecen en la representación integral. Así se han estudiado algunos problemas de difracción de ondas elásticas con la formulación directa (Campillo y Bouchon, 1985; Kawase, 1988; Kawase y Aki 1989; Bouchon et al., 1989; Campillo et al., 1990) y con la indirecta (Hisada et al., 1992, 1994). Con este procedimiento, la integración a lo largo del contorno hace desaparecer las singularidades de las funciones de Green cuando coinciden la posición de la fuente y el punto de observación del desplazamiento o la tracción. Aún así, el cálculo de dichas funciones de Green tiene un costo computacional muy elevado.

En esta tesis se hace uso de una técnica alternativa que utiliza la versión indirecta de la representación. Esta técnica está basada en el hecho de que cuando las funciones de Green son analíticas, las singularidades en la posición de la fuente son integrables (Brebbia, 1978). De esta manera se pueden situar las fuentes en la frontera (fuentes de capa simple) y considerar sus efectos de una forma más apropiada, a la vez que se elimina la incertidumbre sobre la localización de las fuentes como ha ocurrido en otros trabajos (Sánchez-Sesma y Rosenblueth, 1979; Sánchez-Sesma y Esquivel, 1979; Dravinski, 1982; Wong, 1982; Dravinski y Mossessian, 1987), donde las singularidades se situaron fuera de la región de interés. Por otro lado, con esta técnica se pueden aprovechar las ventajas que supone contar con expresiones analíticas de las funciones de Green.

Con este método se ha obtenido la respuesta sísmica de cañones y cordilleras (Sánchez-Sesma y Campillo, 1991, 1993) y de cuencas sedimentarias irregulares (Ramos Martínez y Sánchez-Sesma, 1991; Sánchez-Sesma et al., 1992, 1993 a; Ramos-Martínez et al., 1993; Luzón et al., 1993 a, 1993 b) con geometría bidimensional. También se ha tratado la difracción de ondas elásticas por cordilleras y cañones (Mossessian y Dravinski, 1989, 1992; Zhang y Chopra, 1991; Pedersen et al., 1994 a, 1994 b; Luzón et al., 1995; Luzón y Sánchez-Sesma, 1995), cuencas sedimentarias (Sánchez-Sesma y Luzón, 1995), cuencas sedimentarias configuraciones irregulares (Gil-Zepeda et al., 2002; , Luzón et al., 2003)

Capítulo 3

3. El método indirecto de elementos en la frontera

3.1. Introducción

En este capítulo se muestra la formulación indirecta del método de elementos en la frontera. Esta técnica está basada en la representación integral de los campos de ondas elásticas usando fuentes de capa simple en la frontera. Esta aproximación es llamada indirecta debido a que se tienen que obtener las densidades de fuerza en el contorno del dominio, considerado como un paso intermedio. Las ondas difractadas son construidas en la frontera a partir de la cual aquellas se irradian. Por lo tanto, este método puede ser entendido como una adaptación numérica del Principio de Huygens. Cuando se consideran las condiciones de contorno para esfuerzos y desplazamientos, se llega a un sistema de ecuaciones integrales para las fuentes situadas en la frontera. Después se usa un esquema de discretización basado en la integración numérica y analítica de las funciones de Green exactas para desplazamientos y tracciones en problemas bi y tridimensionales.

3.2. Representación integral usando fuentes en la frontera

Considérese el espacio tridimensional y una superficie continua S, finita o infinita. El sistema de referencia y la notación para desplazamientos que se usan en éste y en los siguientes capítulos se ilustran en la figura 3.1 para el caso de una topografía irregular que representa una montaña. Las coordenadas $X_1(x)$ y $X_2(y)$ forman el plano de la superficie libre del problema, mientras que el eje $X_3(z)$ representa la profundidad; $u(u_1), v(u_2)$ y $z(u_3)$ representan los desplazamientos producidos en cualquier punto en las direcciones $X(x_1), Y(x_2)$ y $Z(x_3)$, respectivamente. Si un material elástico ocupa dicho espacio, el campo de desplazamientos, despreciando fuerzas de volumen, se puede escribir en términos de una integral de frontera de capa simple, en notación indicial, como:

$$\boldsymbol{u}_i\ (\boldsymbol{x}) = \int_S \boldsymbol{\phi}_j(\boldsymbol{\xi})\boldsymbol{G}_{ij}(\boldsymbol{x},\boldsymbol{\xi})\,\boldsymbol{dS}_\xi \tag{10}$$

donde $u_i(x)$ es la iésima componente del desplazamiento en el punto x; $G_{ij}(x,\xi)$ es la función de Green del espacio completo; esto es, el desplazamiento en la dirección i en el punto x debido a la aplicación de una fuerza unitaria en la dirección j en el punto ξ.

$\phi_i(\xi)$ es la densidad de fuerza en la dirección j, por lo tanto, $\phi_i(\xi)dS$ es una distribución de fuerzas sobre la frontera. Los subíndices en la diferencial indican la variable espacial sobre la que se lleva a cabo la integral. Esta integral de capa simple que puede ser obtenida a partir de la identidad de Somigliana (Sánchez-Sesma y Campillo, 1991), ha sido estudiada por Kupradze (1963) desde el punto de vista de la teoría del potencial cuando demostró que el campo de desplazamientos es continuo a través de S si $\phi_i(\xi)$ es continuo a lo largo de S.

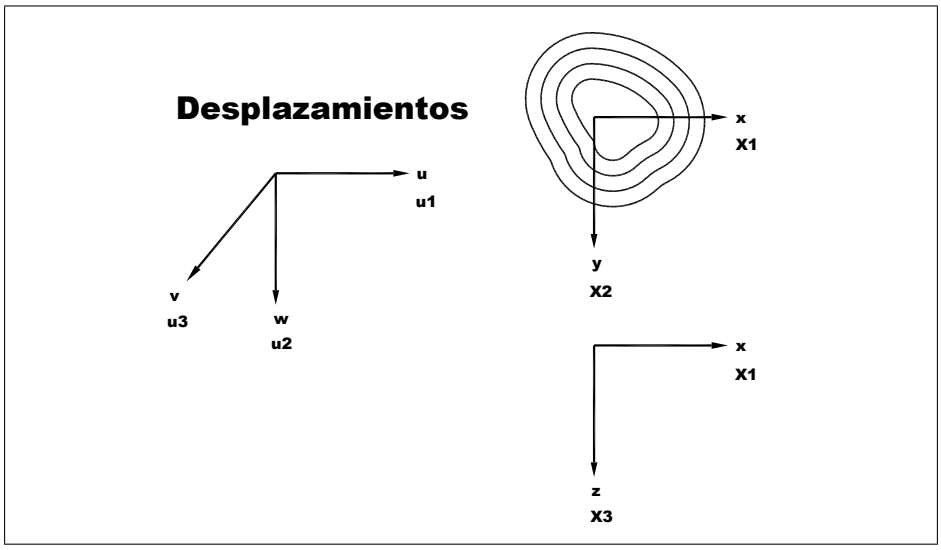

Figura 3.1: Sistema de coordenadas en una montaña 3D y notación usada para los desplazamientos.

La representación integral de la ecuación 10, permite el cálculo de los esfuerzos y las tracciones por aplicación directa de la ley de Hooke, a excepción de las singularidades en la frontera, esto es, cuando x ξ. Con base en consideraciones de equilibrio alrededor de la frontera es posible escribir para x sobre S, que

$$\boldsymbol{t}_i(\boldsymbol{x}) = \boldsymbol{c}\boldsymbol{\phi}_i(\boldsymbol{x}) + \int_S \boldsymbol{\phi}_j(\boldsymbol{\xi})\boldsymbol{T}_{ij}(\boldsymbol{x},\boldsymbol{\xi})\boldsymbol{dS}_\xi \tag{11}$$

donde Ti es la iésima componente de la tracción en la frontera, c = 0.5 si x se aproxima a S por dentro de la región y c = -0.5 si x se aproxima a S desde fuera de la región; $T_{ij}(x,\xi)$ es la función de tracción de Green. Es decir, la tracción en la dirección i en el punto x sobre la frontera con normal $n(x)$ con la suposición de que el vector apunta hacia fuera si x está en S debido a la aplicación de una fuerza unitaria en la dirección j, en el punto ξ. El primer término del lado derecho de la ecuación se anula si x no está sobre S. Este resultado fue obtenido por Kupradze (1963). Las ecuaciones 10 y 11 forman la base de esta aproximación y permiten una interpretación directa de las cantidades físicas involucradas.

3.3. Difracción de ondas elásticas

En este párrafo se presentan los sistemas de ecuaciones integrales que se obtienen como resultado de considerar las condiciones de contorno en desplazamientos y tracciones, con la anterior representación integral. Se tienen en cuenta los casos de difracción debida a cuencas sedimentarias y la debida a topografías.

3.3.1. Difracción por ondas debida a estructuras topográficas superficiales

Considérese un semiespacio elástico E en cuya superficie se sitúa una irregularidad topográfica superficial como la mostrada en la figura 3.2. El movimiento del terreno en esta configuración irregular proviene de interferencias constructivas y destructivas de los campos de onda incidentes, reflejados y difractados. El movimiento total en el semiespacio es la superposición del campo difractado con la solución de campo libre:

$$\boldsymbol{u}_i^E = \boldsymbol{u}_i^0 + \boldsymbol{u}_i^d \tag{12}$$

siendo u_i^0 el desplazamiento de campo libre, es decir, la solución en el semiespacio en ausencia de la irregularidad y que para este caso es la suma del campo incidente más el reflejado. El campo de ondas difractado por la superficie libre es descrito como la radiación de fuentes secundarias distribuidas por toda la superficie. Con la representación integral el campo difractado puede escribirse como:

$$\boldsymbol{u}_i^d(\boldsymbol{x}) = \int_{\partial E} \boldsymbol{\phi}_j(\boldsymbol{\xi}) \boldsymbol{G}_{ij}(\boldsymbol{x}, \boldsymbol{\xi}) d\boldsymbol{S}_\xi \tag{13}$$

Las condiciones de contorno implican tracciones libres en la superficie libre por lo que:

$$\boldsymbol{t}_i^0 + \boldsymbol{t}_i^d = \boldsymbol{0} \tag{14}$$

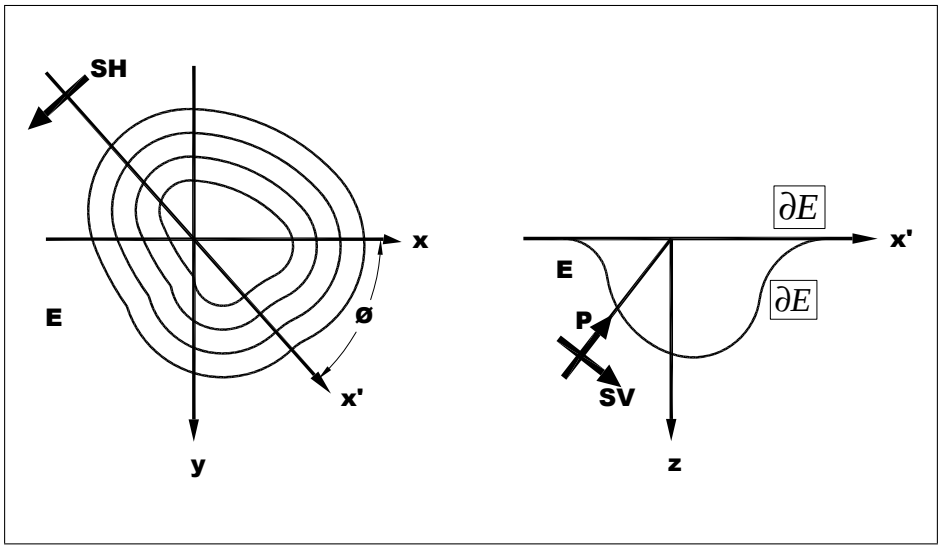

Figura 3.2: Irregularidad topográfica superficial en un semiespacio E e incidencia de ondas elásticas P y S.

entonces, utilizando la ecuación 11 esta condición puede ser expresada como:

$$\mathbf{0{,}5}\boldsymbol{\phi}_i\,(\boldsymbol{x}) + \int_{\partial E} \boldsymbol{\phi}_j(\boldsymbol{\xi})\,\boldsymbol{T}_{ij}(\boldsymbol{x},\boldsymbol{\xi})\,\boldsymbol{dS}_\xi = -\boldsymbol{t}_i^0 \tag{15}$$

la cual resulta ser una ecuación integral de Fredhohm de segunda especie para las fuentes en la frontera. Es decir, aquellas que producen el campo difractado. Las ecuaciones 13 y 15 constituyen un sistema de ecuaciones integrales para las fuentes en la frontera. Estas expresiones serán discretizadas a lo largo de una porción finita de la frontera ∂E, que incluye la topografía y las partes laterales planas correspondientes a la frontera libre.

3.3.2. Difracción por ondas debidas a una inclusión elástica

Considérese una inclusión elástica R como puede ser el caso de un valle homogéneo, que yace sobre un semiespacio también elástico E, como se muestra en la figura 3.3. Dicho sistema está sujeto a la incidencia de ondas elásticas P y S. Las fronteras de la superficie libre en las regiones E y R son llamadas $\partial_1 E$ y $\partial_1 R$, respectivamente. La interfase $\partial_2 E$ y $\partial_2 R$ es la frontera común entre ambos medios. El movimiento del terreno en esta configuración irregular proviene de interferencias constructivas y destructivas de los campos de onda incidentes: Reflejados, difractados y refractados. El movimiento total en el semiespacio E, es la superposición del campo difractado con la solución de campo libre:

$$\boldsymbol{u}_i^E = \boldsymbol{u}_i^0 + \boldsymbol{u}_i^d \tag{16}$$

Siendo $u_i^{(0)}$el desplazamiento de campo libre; es decir, la solución en el semiespacio en ausencia de la irregularidad. De acuerdo con la representación integral del desplazamiento introducida anteriormente, el campo difractado puede escribirse a partir de la ecuación 10 como:

$$\boldsymbol{u}_i^d\,(\boldsymbol{x}) = \int_{\partial E} \boldsymbol{\phi}_j^E(\boldsymbol{\xi})\boldsymbol{G}_{ij}^E(\boldsymbol{x},\boldsymbol{\xi})\,d\boldsymbol{S}_\xi \tag{17}$$

Donde los superíndices de la integral indican la región de validez.

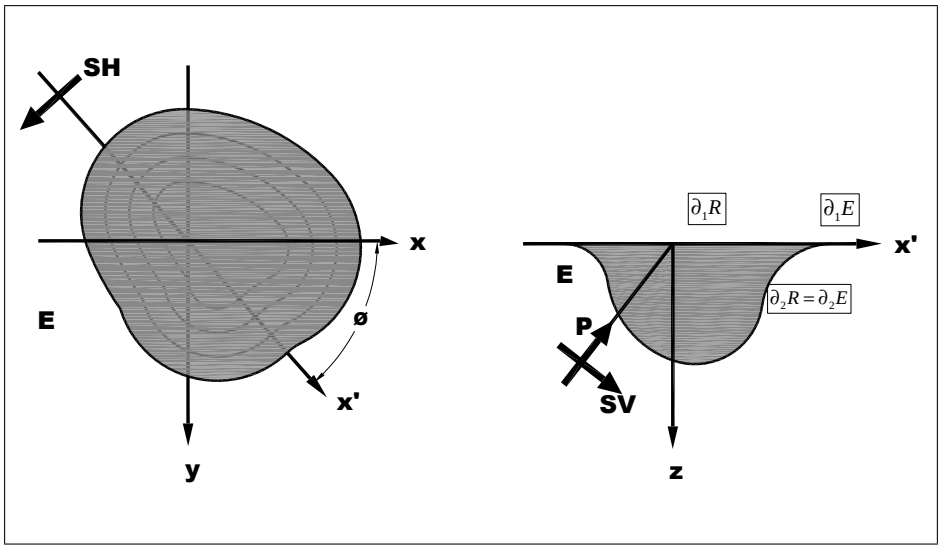

Figura 3.3: Inclusión elástica R en un semiespacio E e incidencia de ondas P y S

El campo refractado en la inclusión R se puede escribir como:

$$\boldsymbol{u}_i^r\,(\boldsymbol{x}) = \int_{\partial R} \boldsymbol{\phi}_j^R(\boldsymbol{\xi})\boldsymbol{G}_{ij}^R(\boldsymbol{x},\boldsymbol{\xi})\,d\boldsymbol{S}_\xi \tag{18}$$

Las condiciones de contorno implican tracciones nulas en la superficie libre por lo que:

$$\boldsymbol{t}_i^0 + \boldsymbol{t}_i^d = \boldsymbol{0} \qquad \text{en} \qquad \boldsymbol{\partial}_1\boldsymbol{E} \tag{19}$$

$$\boldsymbol{t}_i^r = \boldsymbol{0} \qquad \text{en} \qquad \boldsymbol{\partial}_1\boldsymbol{R} \tag{20}$$

entonces, utilizando la ecuación 11, estas condiciones pueden ser expresadas como:

$$\mathbf{0{,}5}\boldsymbol{\phi}_i^E(\boldsymbol{x}) + \int_{\partial E} \boldsymbol{\phi}_j^E(\boldsymbol{\xi})\, \boldsymbol{T}_{ij}^E(\boldsymbol{x},\boldsymbol{\xi})\, d\boldsymbol{S}_\xi = \mathbf{0} \tag{21}$$

$$-\mathbf{0{,}5}\boldsymbol{\phi}_i^R(\boldsymbol{x}) + \int_{\partial R} \boldsymbol{\phi}_j^R(\boldsymbol{\xi})\, \boldsymbol{T}_{ij}^R(\boldsymbol{x},\boldsymbol{\xi})\, d\boldsymbol{S}_\xi = \mathbf{0} \tag{22}$$

En la ecuación 21 se ha considerado que las tracciones de campo libre sobre $\partial_1 E$ son nulas. En la interfaz $\partial_2 E = \partial_2 R$, la continuidad de desplazamientos y tracciones implica que:

$$\boldsymbol{u}_i^0 + \boldsymbol{u}_i^d = \boldsymbol{u}_i^r \tag{23}$$

$$\boldsymbol{t}_i^0 + \boldsymbol{t}_i^d = \boldsymbol{t}_i^r \tag{24}$$

y estas condiciones pueden expresarse como:

$$\int_{\partial E} \boldsymbol{\phi}_j^E(\boldsymbol{\xi})\, \boldsymbol{G}_{ij}^E(\boldsymbol{x},\boldsymbol{\xi})\, d\boldsymbol{S}_\xi - \int_{\partial E} \boldsymbol{\phi}_j^R(\boldsymbol{\xi})\, \boldsymbol{G}_{ij}^R(\boldsymbol{x},\boldsymbol{\xi})\, d\boldsymbol{S}_\xi = -\boldsymbol{u}_i^0 \tag{25}$$

$$\mathbf{0{,}5}(\boldsymbol{\phi}_i^E(\boldsymbol{x}) + \boldsymbol{\phi}_i^R(\boldsymbol{x})) + \int_{\partial E} \boldsymbol{\phi}_j^E(\boldsymbol{\xi})\, \boldsymbol{T}_{ij}^E(\boldsymbol{x},\boldsymbol{\xi})\, d\boldsymbol{S}_\xi - \int_{\partial R} \boldsymbol{\phi}_j^R(\boldsymbol{\xi})\, \boldsymbol{T}_{ij}^R(\boldsymbol{x},\boldsymbol{\xi})\, d\boldsymbol{S}_\xi = -\boldsymbol{t}_i^0 \tag{26}$$

Las ecuaciones 17, 18, 21, 22, 25, 26 constituyen un sistema de ecuaciones integrales para fuentes en la frontera, es decir aquellas que producen los campos difractados y refractados. Estas expresiones serán discretizadas a lo largo de una porción finita de la frontera ∂E, que incluye la interfase común entre ambas regiones y las partes laterales planas correspondientes a la frontera libre, y sobre ∂R, de acuerdo a la definición de cada integral.

3.4. Discretización

Para resolver los anteriores sistemas de ecuaciones integrales es necesario discretizarlos. Estas integrales recorren la superficie del contorno del espacio

elástico, por lo que esta discretización está basada en la de la superficie de la frontera. La discretización de una superficie no es un problema fácil aunque existen distintos algoritmos para ello (George, 1991). La elección del esquema de discretización depende del problema y de la formulación matemática a - usar. Por ejemplo, en muchas aplicaciones se usan elementos triangulares para discretizar superficies (Manolis y Beskos, 1988; Brebbia y Domínguez, 1992).

En este trabajo se utilizan dos esquemas distintos dependiendo de si el problema es bi o tridimensional. Para el caso 2D, la superficie se construye con segmentos iguales rectilíneos de longitud ΔS con pendientes distintas. En la figura 3.4 se muestra un ejemplo de este tipo de discretización con la distribución de fuentes sobre todo el contorno en una irregularidad topográfica superficial. Para poder integrar las funciones de Green, es necesario conocer el valor de ΔS y el vector normal n correspondientes a cada elemento. Para el caso bidimensional, cada longitud ΔS y cada valor normal se conocen desde la misma construcción de las fronteras por elementos.

Para el caso 3D se utiliza un esquema simplificado y se usan círculos de varios tamaños para discretizar las superficies de tal forma que cubren aproximadamente toda la frontera. Esta elección puede parecer un tanto burda, sin embargo, permite una formulación simple y una implementación relativamente fácil. Esta opción ha sido guiada por el hecho de que las integrales de las funciones de Green sobre circunferencias se pueden obtener fácilmente.

La discretización en estructuras 3D se ha realizado dividiendo las superficies en distintas bandas y rellenando cada una con circunferencias. Los radios de éstas se han tomado de tal forma que la suma de todas sus superficies sea igual a la de cada banda. El problema que no es fácil de resolver. A continuación es el asignar a cada elemento su correspondiente vector normal n.

Geometrías superficiales que admiten representación analítica. De esta manera se ha podido calcular el vector normal n a cada elemento a partir del vector normal a la superficie analítica en el punto ξ, sobre el que se sitúa la circunferencia. En futuros análisis se estudiarán técnicas de elementos finitos para discretizar superficies con geometrías no analíticas.

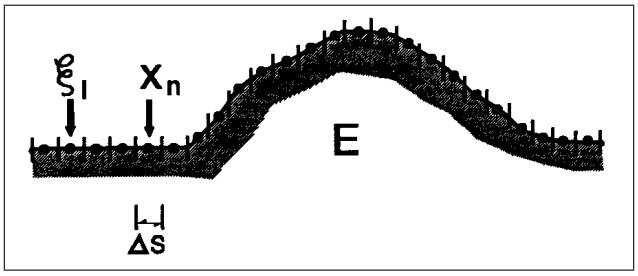

Figura 3.4: Discretización de la superficie de una irregularidad topográfica superficial bidimensional en segmentos rectilíneos con pendientes distintas.

En la figura 3.5 se muestra la distribución de elementos sobre la superficie de un cañón semiesférico. En la perspectiva a) aparece el plano $x - y$, que corresponde a la vista desde arriba de la superficie libre. También se muestran sombreados los elementos de la primera de las bandas de la superficie libre plana. En la perspectiva b) se muestra el perfil del plano $x - z$ con los vectores normales representados en algunos de los elementos; en este caso los vectores normales de los elementos situados en el interior de la cuenca semiesférica están dirigidos hacia el origen de coordenadas.

El número de elementos en los que se dividen las fronteras depende de la frecuencia y de las dimensiones de la estructura en estudio. Para tener una discretización con la que se obtengan resultados fiables, es necesario que haya un número mínimo de elementos por longitud de onda λ. Así, conforme se aumenta la frecuencia de interés, λ disminuye y es necesario un número mayor de elementos, lo que encarece el costo computacional. Con esta técnica se han hecho varias pruebas y se ha comprobado que usando cuatro elementos por longitud de onda se obtienen muy buenos resultados.

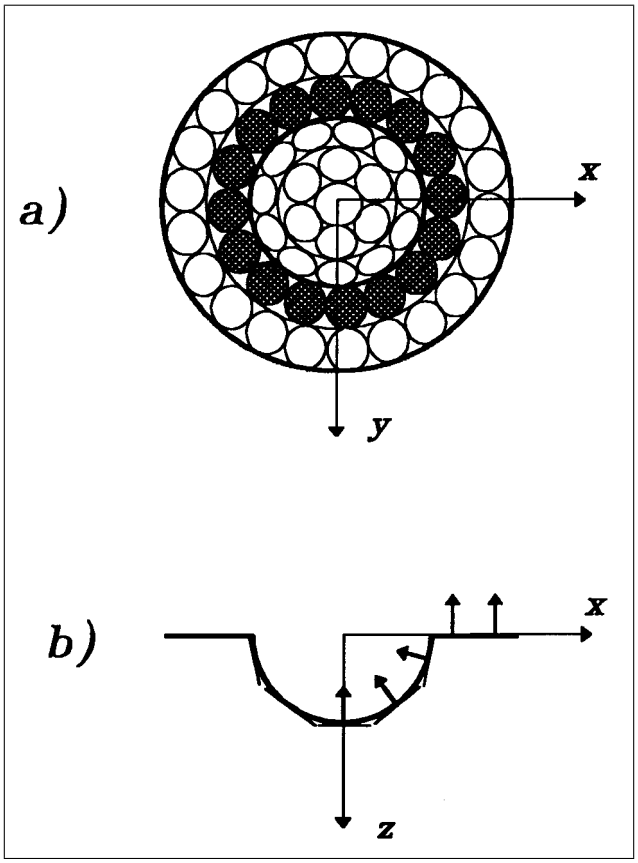

Figura 3.5: Cañón semiesférico tridimensional. a) Vista desde arriba y distribución de elementos en la superficie. Se muestran sombreados los círculos correspondientes a una banda. b) perfil del plano $x - z$ con los vectores normales representados en algunos de los elementos.

En la discretización que se va a llevar a cabo, se ha asumido que las densidades de fuerza $\phi_j(\xi)$ son constantes sobre cada uno de los elementos que forman la frontera. Cada elemento tendrá una superficie ΔS_1, (o longitud ΔS_1 para el caso bidimensional) y estará centrado en el punto ξ_1 apropiado. A continuación se muestra la discretización de las ecuaciones integrales para los dos casos que estamos tratando: estructuras topográficas superficiales y cuencas sedimentarias. El sistema de ecuaciones integrales a resolver en cada problema es distinto, debido a las diferentes condiciones de contorno que aparecen en cada uno de ellos.

3.4.1. Discretización en estructuras topográficas superficiales

Notemos como M el número de elementos que existen en la parte plana del semiespacio E y L como el número de elementos en la superficie irregular no plana de la topografía. Entonces el número total de elementos de frontera N será igual a $M + L$ y el número de incógnitas $\phi_j(\xi)$(con $j = 1, 2, 3$ Y $1 = 1, ..., N$) será de $3M + 3L$, que coincide con el número de ecuaciones. La ecuación 15 se puede representar entonces como:

$$\sum_{l=1}^{N} \boldsymbol{\phi}_j(\boldsymbol{\xi}_l)\boldsymbol{t}_{ij}(\boldsymbol{x}_n, \boldsymbol{\xi}_l) = -\boldsymbol{t}_i^0(\boldsymbol{x}_{n)}) \qquad \boldsymbol{n = 1, ..., N} \tag{27}$$

Donde

$$\boldsymbol{t}_{ij}(\boldsymbol{x}_n, \boldsymbol{\xi}_l\ ) = \frac{1}{2}\boldsymbol{\delta}_{ij}\boldsymbol{\delta}_{nl} + \int_{\Delta S_l} \boldsymbol{T}_{ij}(\boldsymbol{x}_n, \boldsymbol{\xi}_l)\boldsymbol{dS}_{\xi} \tag{28}$$

Estas integrales se pueden calcular numéricamente usando integración gaussiana (Abramowitz y Stegun, 1972), excepto cuando $n = 1$. En este caso se tiene que:

$$\boldsymbol{t}_{ij}(\boldsymbol{x}_n, \boldsymbol{\xi}_n\ ) = \frac{1}{2}\boldsymbol{\delta}_{ij} \tag{29}$$

debido a que la única contribución de aquella ecuación proviene del término de la delta de Krönecker para n= l. La contribución del tensor de tracciones de Green T_{ij} es nula para los elementos circulares planos (3D) y segmentos rectos (2D) como ocurre en este trabajo. De hecho, de las expresiones para las tracciones de Green se puede verificar que, bajo estas circunstancias, tal parte del integrando es una función singular sobre el elemento y su valor principal de Cauchy es cero. El valor para t_{ij} en la ecuación 29 se puede interpretar como la mitad de la fuerza unitaria aplicada en el punto, es decir, que la fuerza se distribuye simétricamente en los dos medios sin importar su dirección de aplicación. De hecho, este resultado corresponde con la solución estática (Sánchez-Sesma y Campillo, 1991).

El sistema de ecuaciones integrales discretizadas se puede representar como $M\phi = t$, donde M es la matriz de coeficientes, t es el vector de términos independientes (solución de tracciones libres) y ϕ es el vector de las densidades de fuerza (incógnitas). Éste es un sistema de ecuaciones lineales con coeficientes

complejos que se puede resolver haciendo una descomposición de la matriz de coeficientes $M = L.U$, donde la matriz L sólo tiene elementos distintos de cero en la diagonal y por debajo de ésta y la matriz U en la diagonal y por arriba (Press et al, 1992). Una vez resuelto este sistema de ecuaciones lineales se conocen los valores de $\phi_j(\xi_l)$, con los que se puede calcular el campo difractado en los puntos x de interés según la versión discretizada de la ecuación 13, es decir según:

$$\boldsymbol{u_i^d}\ (\boldsymbol{x}) = \sum_{l=1}^{N} \boldsymbol{\phi_j(\xi_l) g_{ij}(x, \xi_l)} \tag{30}$$

Donde

$$\boldsymbol{g_{ij}(x, \xi_l}\ ) = \int_{\Delta S_l} \boldsymbol{G_{ij}(x, \xi)\, dS_\xi} \tag{31}$$

Estas integrales también se pueden calcular numéricamente con integración gaussiana, excepto cuando el punto x está en las proximidades de ξ_j. Para el caso bidimensional Sánchez-Sesma y Campillo (1991), obtuvieron expresiones analíticas a partir de las series ascendentes de las funciones de Bessel que aparecen en las funciones de Green. Para el caso tridimensional y cuando coinciden x_n con el centro del elemento circular de radio R, se puede demostar que:

$$\int_{\Delta S_l} \boldsymbol{G_{ij}(x, \xi)\, dS_\xi} = \frac{1}{4}[(\boldsymbol{F}_2 + \boldsymbol{F}_1)\boldsymbol{\delta_{ij}} + (\boldsymbol{F}_2 - \boldsymbol{F}_1)\boldsymbol{n_i n_j}] \tag{32}$$

Donde se ha integrado usando coordenadas polares locales; F_K para $k = 1, 2$, es la integral desde 0 hasta R de las funciones f_K que aparecen en las correspondientes funciones de Green y $n_i = i$-ésima componente del vector normal al elemento. Considerando series de potencias hasta el término cúbico de las exponenciales que aparecen en las funciones f_1 y f_2 es posible mostrar que:

$$\boldsymbol{F}_1 = \boldsymbol{R}\left[1 - \frac{i}{6}\left(2 + \left(\frac{\beta}{\alpha}\right)^3\right)kR - \frac{1}{18}\left(2 + \left(\frac{\beta}{\alpha}\right)^4\right)k^2R^2 + \frac{i}{24}\left(\frac{\beta}{\alpha}\right)^5 k^3R^3\right] \tag{33}$$

$$\boldsymbol{F}_2 = \boldsymbol{R}\left[\frac{1 + \left(\frac{\beta}{\alpha}\right)^2}{2} - \frac{i}{6}\left(2 + \left(\frac{\beta}{\alpha}\right)^3\right)kR - \frac{1}{18}\left(2 + \left(\frac{\beta}{\alpha}\right)^4\right)k^2R^2 + \frac{i}{24}k^3R^3\right] \tag{34}$$

3.4.2. Discretización en cuencas sedimentarias

Notemos como M el número de elementos que existen en la parte plana del semiespacio E (figura 3.3), L como el número de elementos en la interfaz común del semiespacio E y la región R, y K el número de elementos de la superficie libre de la región R. Entonces el número total de elementos de frontera N será igual a $M + 2L + K$. El número de incógnitas $\phi_j(\xi)$ será de $3M + 6L + 3K$, que coincide con el número de ecuaciones. Las ecuaciones 21 y 22 se pueden discretizar entonces como:

$$\sum_{l=1}^{N} \boldsymbol{\phi}_j^E(\boldsymbol{\xi}_l)\boldsymbol{t}_{ij}^E(\boldsymbol{x}_n, \boldsymbol{\xi}_l) = \boldsymbol{0} \tag{35}$$

$$\sum_{l=1}^{N} \boldsymbol{\phi}_j^R(\boldsymbol{\xi}_l)\boldsymbol{t}_{ij}^R(\boldsymbol{x}_n, \boldsymbol{\xi}_l) = \boldsymbol{0} \tag{36}$$

donde

$$\boldsymbol{t}_{ij}^E(\boldsymbol{x}_n, \boldsymbol{\xi}_l\,) = \frac{1}{2}\boldsymbol{\delta}_{ij}\boldsymbol{\delta}_{nl} + \int_{\Delta S_l} \boldsymbol{T}_{ij}^E(\boldsymbol{x}, \boldsymbol{\xi})\, d\boldsymbol{S}_\xi \tag{37}$$

$$\boldsymbol{t}_{ij}^{R}(\boldsymbol{x}_n, \boldsymbol{\xi}_l) = -\frac{1}{2}\boldsymbol{\delta}_{ij}\boldsymbol{\delta}_{nl} + \int_{\Delta S_l} \boldsymbol{T}_{ij}^{R}(\boldsymbol{x}, \boldsymbol{\xi})\, d\boldsymbol{S}_{\xi} \tag{38}$$

y las ecuaciones 25, 26 como:

$$\sum_{l=1}^{M+L} \boldsymbol{\phi}_j^{E}(\boldsymbol{\xi}_l)\boldsymbol{g}_{ij}^{E}(\boldsymbol{x}_n, \boldsymbol{\xi}_l) - \sum_{l=1}^{L+K} \boldsymbol{\phi}_j^{R}(\boldsymbol{\xi}_l)\boldsymbol{g}_{ij}^{R}(\boldsymbol{x}_n, \boldsymbol{\xi}_l) = -\boldsymbol{u}_i^{0}(\boldsymbol{x}_n) \tag{39}$$

$$\sum_{l=1}^{M+L} \boldsymbol{\phi}_j^{E}(\boldsymbol{\xi}_l)\boldsymbol{t}_{ij}^{E}(\boldsymbol{x}_n, \boldsymbol{\xi}_l) - \sum_{l=1}^{L+K} \boldsymbol{\phi}_j^{R}(\boldsymbol{\xi}_l)\boldsymbol{t}_{ij}^{R}(\boldsymbol{x}_n, \boldsymbol{\xi}_l) = -\boldsymbol{t}_i^{0}(\boldsymbol{x}_n) \tag{40}$$

donde

$$\boldsymbol{g}_{ij}^{H}(\boldsymbol{x}_n, \boldsymbol{\xi}_l) = \int_{\Delta S_l} \boldsymbol{G}_{ij}^{H}(\boldsymbol{x}_n, \boldsymbol{\xi})\, d\boldsymbol{S}_{\xi} \tag{41}$$

$$\boldsymbol{t}_{ij}^{H}(\boldsymbol{x}_n, \boldsymbol{\xi}_l) = \frac{1}{2}\boldsymbol{\delta}_{ij}\boldsymbol{\delta}_{nl} + \int_{\Delta S_l} \boldsymbol{T}_{ij}^{H}(\boldsymbol{x}_n, \boldsymbol{\xi})\, d\boldsymbol{S}_{\xi} \tag{42}$$

con H igual a E o R dependiendo de la región en la que se esté integrando. Las integrales en las que aparecen las funciones y tracciones de Green se calculan como en el caso de topografías.

Una vez que se conocen los valores de $\phi_j(\xi_l)$ resolviendo el sistema de ecuaciones lineales obtenido, se calculan los desplazamientos en la dirección i del punto x del semiespacio E como:

$$\boldsymbol{u}_i^{0}(\boldsymbol{x}) + \boldsymbol{u}_i^{d}(\boldsymbol{x}) = \boldsymbol{u}_i^{0}(\boldsymbol{x}) + \sum_{l=1}^{M+L} \boldsymbol{\phi}_j^{E}(\boldsymbol{\xi}_l)\boldsymbol{g}_{ij}^{E}(\boldsymbol{x}, \boldsymbol{\xi}_l) \tag{43}$$

donde

$$\boldsymbol{g}_{ij}^{E}(\boldsymbol{x},\boldsymbol{\xi}_l\,) = \int_{\Delta S_l} \boldsymbol{G}_{ij}^{E}(\boldsymbol{x},\boldsymbol{\xi})\,\boldsymbol{dS}_{\xi} \tag{44}$$

y los desplazamientos en la dirección i del punto x en la región R como:

$$\boldsymbol{u}_i^r\ (\boldsymbol{x}) = \sum_{l=1}^{L+K} \boldsymbol{\phi}_j^R(\boldsymbol{\xi}_l)\boldsymbol{g}_{ij}^R(\boldsymbol{x},\boldsymbol{\xi}_l) \tag{45}$$

donde

$$\boldsymbol{g}_{ij}^{R}(\boldsymbol{x},\boldsymbol{\xi}_l\,) = \int_{\Delta S_l} \boldsymbol{G}_{ij}^{R}(\boldsymbol{x},\boldsymbol{\xi})\,\boldsymbol{dS}_{\xi} \tag{46}$$

Las anteriores integrales se calculan numéricamente con integración gaussiana, excepto en las proximidades de ξ_l, donde se obtienen expresiones analíticas como en el caso de topografías.

3.5. Respuesta sísmica en función del tiempo, el pulso de Ricker

Como se ha visto, el método indirecto de elementos en la frontera puede proporcionar la respuesta de una estructura geológica ante la incidencia de ondas elásticas en cualquier punto x. Esta respuesta que viene expresada en el dominio de la frecuencia, es la función de transferencia de dicha estructura respecto al campo de ondas incidentes.

Considérese una configuración geológica arbitraria en la que introducimos una determinada vibración $e(t)$ donde t indica que estamos en el dominio del tiempo. Esta estructura proporcionará una salida $s(t)$ (figura 3.6). La salida obtenida en nuestro caso corresponde al movimiento del suelo. En general,

dicha salida se puede obtener aplicando a la entrada un operador H, que representa la estructura geológica, de tal forma que:

$$\boldsymbol{s(t) = H[e(t)]} \tag{47}$$

Para caracterizar a la estructura, se define la función de respuesta impulsional $h(t)$. Esta función representa la salida si la entrada es un impulso unitario $\delta(t)$. Entonces $s(t)$ se puede expresar como la convolución de la entrada $e(t)$ con la función de la respuesta impulsional $h(t)$.

$$\boldsymbol{s(t) = e(t) * h(y)} \tag{48}$$

Si calculamos las transformadas de Fourier de ambos lados de la anterior ecuación tenemos:

$$\boldsymbol{S(\omega) = E(\omega)H(\omega)} \tag{49}$$

donde ω es la frecuencia angular y $S(\omega), E(\omega),$ y $H(\omega)$ son las funciones complejas en el dominio de la frecuencia transformadas de $s(t), e(t)$ y $h(t)$, respectivamente. La función $H(\omega)$ que se obtiene mediante:

$$\boldsymbol{H(\omega) = \frac{S(\omega)}{E(\omega)}} \tag{50}$$

se define como la función de transferencia de la estructura geológica, con la que una vez conocida se puede tener la salida utilizando la ecuación 49 con una determinada entrada dada. Es posible obtener $E(\omega)$ a partir de $e(t)$ empleando el algoritmo de la transformada rápida de Fourier FFT (Rikitake et al, 1987). Utilizando el mismo algoritmo se puede calcular la salida en función del tiempo $s(t)$ a partir de $S(\omega)$ con la transforada inversa.

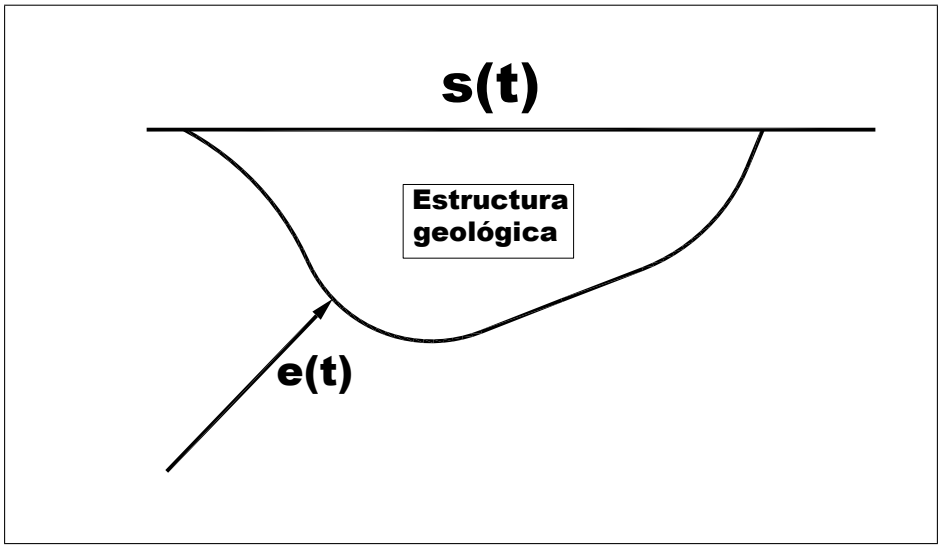

Figura 3.6: Señal temporal de la entrada y salida en una estructura geológica arbitraria.

En muchos de los ejemplos que se van a realizar en esta tesis se va a utilizar como señal de entrada un pulso de Ricker (Riker, 1977). Este pulso ha sido usado ampliamente en problemas de difracción de ondas elásticas (Kawase, 1988); Sánchez-Sesma et al., 1988, 1989, 1993; Kawase y Aki, 1989; Horike et al., 1990; Sánchez-Sesma y Campillo, 1991; Takemiya y Tomono, 1992; Pedersen et al., 1994 a, 1994 b; Sánchez-Sesma y Luzón, 1995) y su expresión viene dada en el tiempo por:

$$\text{Amplitud}(\boldsymbol{t})\ (\boldsymbol{a}^2 - \frac{1}{2})\boldsymbol{e}^{-a^2}\ ,\ \text{donde} \quad \boldsymbol{a} = \frac{\pi(t - t_s)}{t_p} \tag{51}$$

donde t_p es el período característico del pulso y t_s es el tiempo de retraso. La representación gráfica del pulso de Ricker es función del tiempo, y de la frecuencia se muestra en la figura 3.7.

Cuando se trata con una onda de la forma $e^{i(kx-\omega t)}$, como es el caso considerado aquí, se puede tener en cuenta la atenuación en la propagación reemplazando la frecuencia y el número de onda por valores complejos (Aki y Richards, 1980). Entonces la frecuencia y el número de onda k_0 se transformarán como:

$$\boldsymbol{\omega} = \boldsymbol{\omega}_0 - \boldsymbol{i}\,\frac{|\omega_0|}{2Q_t} \tag{52}$$

$$k = k_0 - i\,\frac{|k_0|}{2Q_x} \tag{53}$$

donde Q_x y Q_t son los factores de amortiguamiento espacial y temporal, respectivamente. Otras formas de introducir el amortiguamiento espacial y temporal, junto con una detallada discusión, se pueden encontrar en Aki y Richards (1980).

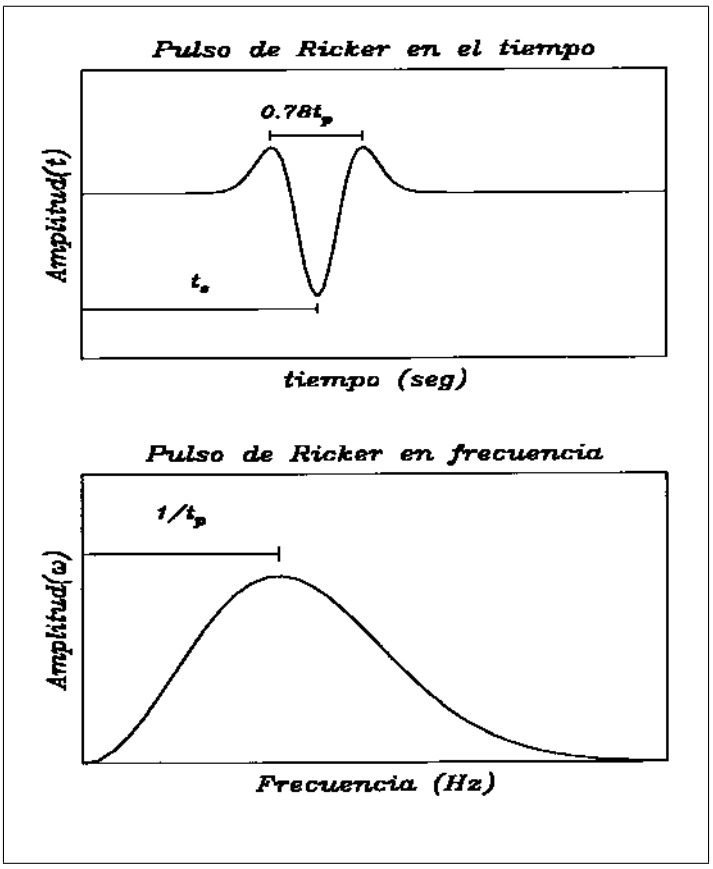

Figura 3.7: Pulso de Richter en el tiempo y frecuencia

Capítulo 4

4. Discretización geométrica

4.1. Datos (x, y, z)

Para iniciar la discretización de una topografía o un valle aluvial, es imprescindible contar con las coordenadas de un buen número de puntos que correspondan a la superficie en estudio. Estos puntos estarán referidos a un sistema carteciano y representados por (x, y, z), ordenada, abscisa y cota respectivamente. Entre mayor número de puntos exista mejor será representada la superficie.

4.2. Contornos

Los contornos son líneas que recorren una superficie en el espacio con igual cota "z". Para poder lograr un contorno, es necesario contar con las coordenadas (x, y, z) de los puntos del inciso anterior, aparte de los métodos numéricos para la interpolación detallada de la superficie, tal como es el caso de cubic splines que van uniendo los puntos consecutivamente con segmentos de línea que satisfacen las condiciones de posición en un punto inicial y uno final, así como los ángulos de entrada y salida respectivamente, en cada segmento de línea para que realmente exista continuidad en cada uno de los puntos que intervienen en cada contorno, la ecuación cúbica que debe satisfacer cada intervalo esta dada por la siguiente expresión:

$$\boldsymbol{y = a_i(x - x_i)^3 + b_i\,(x - x_i)^2 + c_i\,(x - x_i) + d_i} \tag{54}$$

Si S_i es la pendiente de continuidad entre el intervalo n y $n-1$, así como el intervalo i-ésimo en la dirección x se denomina como h_i.

$$\boldsymbol{h_i = x_{i+1} - x_i} \tag{55}$$

Los coeficientes a_i, b_i, c_i, d_i pueden ser calculados con las siguientes expresiones:

$$\boldsymbol{a_i} = \frac{S_{i+1} - S_i}{6h_i} \tag{56}$$

$$\boldsymbol{b_i} = \frac{S_i}{2} \tag{57}$$

$$\boldsymbol{c_i} = \frac{y_{i+1} - y_i}{h_i} - \frac{2h_iS_i + h_iS_{i+1}}{6} \tag{58}$$

$$\boldsymbol{d_i} = \boldsymbol{y_i} \tag{59}$$

en estas ecuaciones todo es conocido excepto los valores de S, estos pueden calcularse por medio de ecuaciones simultáneas, suponiendo que las condiciones de las pendientes en las fronteras sean $S_1 = 0$ y $S_n = 0 \quad \therefore \quad S_i$ se calcula con la siguiente ecuación:

$$\begin{bmatrix} \boldsymbol{2(h_1 + h_2)} & & & & & \\ \boldsymbol{h_2} & \boldsymbol{2(h_2 + h_3)} & \cdots & & & \\ & \vdots & \ddots & \boldsymbol{h_{n-2}} & & \\ & & \boldsymbol{h_{n-2}} & \boldsymbol{2(h_{n-3} + h_{n-2})} & \boldsymbol{h_{n-1}} & \\ & & & \boldsymbol{h_{n-1}} & \boldsymbol{2(h_{n-2} + h_{n-1})} & \end{bmatrix} \begin{bmatrix} \boldsymbol{S_2} \\ \mathbf{S_3} \\ \vdots \\ \boldsymbol{S_{n-2}} \\ \boldsymbol{S_{n-1}} \end{bmatrix}$$

$$= \begin{bmatrix} \frac{y_4 - y_3}{h_3} - \frac{y_3 - y_2}{h_2} \\ \frac{y_5 - y_4}{h_4} - \frac{y_4 - y_3}{h_3} \\ \vdots \\ \frac{y_{n-1} - y_{n-2}}{h_{n-1}} - \frac{y_{n-2} - y_{n-3}}{h_{n-2}} \\ \frac{y_n - y_{n-1}}{h_n} - \frac{y_{n-1} - y_{n-2}}{h_{n-1}} \end{bmatrix} \tag{60}$$

s conocidas se pued**de tal manera que los valores de S son ahora conocidos y sustituyendo en las ecuaciones 56, 57, 58 y 59. De igual manera con los valores calculados de a_i, b_i, c_i, d_i y sustituyendo en la ecuación 54 se observa que es posible calcular cualquier número de puntos intermedios en ese intervalo.**

4.3. Generación de cotas con elementos equiespaciados en "x" y "y"

De igual manera que en el inciso anterior, se utiliza la interpolación por medio de cubic splains sobre el plano xy, en los planos xz y yz, finalmente se obtiene una matriz de cotas "z" en donde no es necesario guardar las matrices "x" y "y", basta conocer los valores iniciales mínimos $x_{\text{mín}}$, $y_{\text{mín}}$ y los valores de Δx, Δy de tal manera que si se desea saber cualquier punto de coordenada discreta i, j en la matriz "z", las coordenadas serán:

$$\boldsymbol{x_i} = \boldsymbol{x_{\text{mín}} + (i-1)\Delta x} \tag{61}$$

$$\boldsymbol{y_j} = \boldsymbol{y_{\text{mín}} + (j-1)\Delta y} \tag{62}$$

$$\boldsymbol{z_{ij}} = \boldsymbol{(x_i, y_j) = [x_{\text{mín}} + (i-1)\Delta x, \;\; x_i = y_{\text{mín}} + (j-1)\Delta y]} \tag{63}$$

Al final de este proceso se tiene una malla reticular tan fina como uno lo requiera y esto dependerá de la frecuencia máxima según el problema de que se trate.

4.4. Integración numérica de la superficie

Puesto que todos los puntos discretos tienen coordenadae calcular la superficie en cada Δx y Δy, figura 4.1.

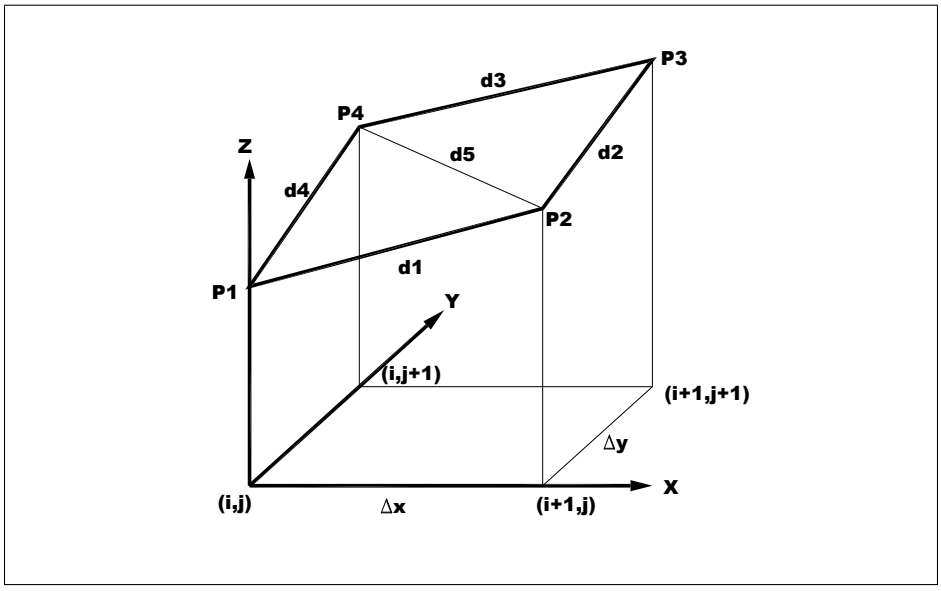

Figura 4.1; Cuadrilátero sobre la superficie del cuerpo en estudio y su proyección en el plano xy.

De la figura 4.1 se observa que las coordenadas en cada uno de los puntos están definidas por:

$$\boldsymbol{P}_1(\boldsymbol{x}_{i,j},\ \boldsymbol{y}_{i,j},\ \boldsymbol{z}_{i,j}) \tag{64}$$

$$\boldsymbol{P}_2(\boldsymbol{x}_{i+1,j},\ \boldsymbol{y}_{i+1,j},\ \boldsymbol{z}_{i+1,j}) \tag{65}$$

$$\boldsymbol{P}_3(\boldsymbol{x}_{i+1,j+1},\ \boldsymbol{y}_{i+1,j+1},\ \boldsymbol{z}_{i+1,j+1}) \tag{66}$$

$$\boldsymbol{P}_4(\boldsymbol{x}_{i,j+1},\ \boldsymbol{y}_{i,j+1},\ \boldsymbol{z}_{i,j+1}) \tag{67}$$

Sabiendo las coordenadas de cada uno de los puntos del cuadrilátero, entonces las distancias d_1, d_2, d_3, d_4 y d_5 son:

$$\boldsymbol{d}_1 = \sqrt{(x_{i+1,j}-x_{i,j})^2+(y_{i+1,j}-y_{i,j})^2+(z_{i+1,j}-z_{i,j})^2} \tag{68}$$

$$\boldsymbol{d}_2 = \sqrt{(x_{i+1,j+1}-x_{i+1,j})^2+(y_{i+1,j+1}-y_{i+1,j})^2+(z_{i+1,j+1}-z_{i+1,j})^2} \tag{69}$$

$$\boldsymbol{d}_3 = \sqrt{(x_{i,j+1}-x_{i+1,j+1})^2+(y_{i,j+1}-y_{i+1,j+1})^2+(z_{i,j+1}-z_{i+1,j+1})^2} \tag{70}$$

$$\boldsymbol{d}_4 = \sqrt{(x_{i,j+1}-x_{i,j})^2+(y_{i,j+1}-y_{i,j})^2+(z_{i,j+1}-z_{i,j})^2} \tag{71}$$

$$\boldsymbol{d}_5 = \sqrt{(x_{i,j+1}-x_{i+1,j})^2+(y_{i,j+1}-y_{i+1,j})^2+(z_{i,j+1}-z_{i+1,j})^2} \tag{72}$$

De tal manera que el área de cada triángulo está definida por:

$$\boldsymbol{S}_1 = \frac{d_1 + d_4 + d_5}{2} \tag{73}$$

$$\boldsymbol{S}_2 = \frac{d_2 + d_3 + d_5}{2} \tag{74}$$

$$\boldsymbol{A}_1 = \sqrt{S_1(S_1 - d_1)(S_1 - d_4)(S_1 - d_5)} \tag{75}$$

$$\boldsymbol{A}_2 = \sqrt{S_2(S_2 - d_2)(S_2 - d_3)(S_2 - d_5)} \tag{76}$$

$$\boldsymbol{A}_t = A_1 + A_2 \tag{77}$$

En donde el área total del cuadrilátero es A_t para cada intervalo $\Delta x,\ \Delta y$

4.5. Transformación de áreas equivalentes de rectángulos a círculos

Sea A_c = área de un círculo, r = radio del círculo, A_e = es el área de un rectángulo equivalente y se requieren cuatro círculos alineados correspondientes para que ocupen un espacio de una longitud de onda λ a una velocidad de propagación β y a una frecuencia f, entonces $\lambda = 8r$ por lo tanto $r = \frac{\lambda}{8} = \frac{\beta}{8f}$. Sí $A_c = \pi r^2$ y el área rectangular formado por cuadriláteros es $A_e = n^2 \Delta x \Delta y$, de tal manera que se trata de elementos equiespaciados, entonces $\Delta x = \Delta y$, por lo tanto $A_e = (n\Delta x)^2$ entonces el área equivalente de rectángulos a círculos es:

$$(\boldsymbol{n\Delta}_x)^2 = \boldsymbol{\pi r^2} = \boldsymbol{\pi}\ \frac{\beta^2}{64f^2} \tag{78}$$

$$\boldsymbol{r} = \frac{n\Delta_x}{\sqrt{\pi}} \tag{79}$$

$$\boldsymbol{n} = \sqrt{\pi}\frac{\beta}{8f\Delta x} \tag{80}$$

De tal manera que el número de cuadrilateros que se requiere en la discretización es $n = \sqrt{\pi}\frac{\beta}{8f\Delta x}$ donde n es el número de cuadrilateros en x, y otro tanto en y equivalentes al área del círculo necesario para garantizar una buena discretización del problema en estudio.

La discretización de elementos circulares resulta más simple cuando la superficie coincide con el semiespacio si el radio aproximado es definido como $r_a = \frac{\beta}{8f_{\text{máx}}}$ y el número de anillos se define como $n_L = int(\frac{r_{\text{máx}}}{2r})$, donde $r_{\text{máx}}$ es el radio del anillo máximo, entonces el radio del círculo exacto es $r_c = \frac{r_{\text{máx}}}{2n_L+1}$.

El área del anillo i ésimo es $A_i = 8(i)\pi r_c^2$, para $1 \leqslant i \leqslant n_L$, el número de círculos en el anillo i ésimo será $nC_i = 8(i)$, entonces los centroides de cada círculo quedan perfectamente definidos con las siguientes ecuaciones:

$$\boldsymbol{X}\boldsymbol{c}_{ij} = \boldsymbol{2r}\cos\left(\frac{\pi}{8(i)}(j-1)\right) \tag{81}$$

$$\boldsymbol{Y}\boldsymbol{c}_{ij} = \boldsymbol{2r}\sin\left(\frac{\pi}{8(i)}(j-1)\right) \tag{82}$$

para $1 \leqslant i \leqslant n_L$, $1 \leqslant j \leqslant nC_i$, donde i es i ésimo anillo y j es el j ésimo círculo en el anillo i, vease el semiespacio en la figura 4.2

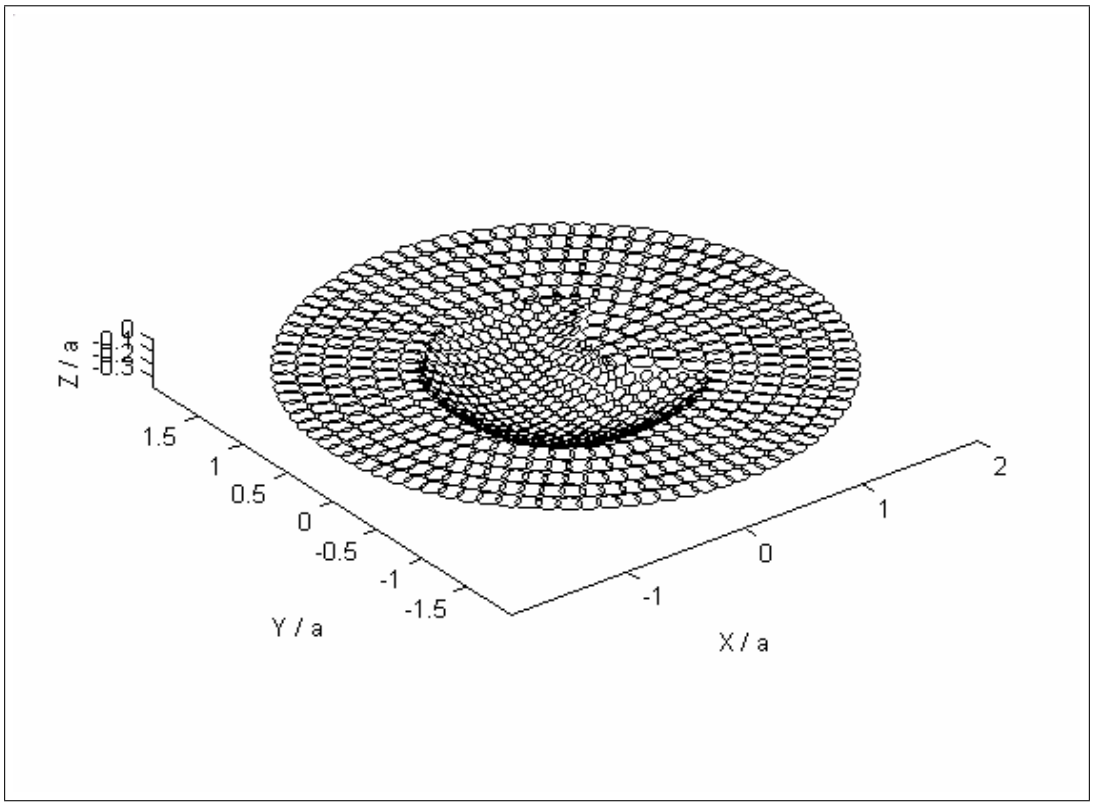

Figura 4.2; Discretización con elementos circulares se aprecia el valle aluvial y el semiespacio.

4.6. Cálculo de los centroides y la orientación de los elementos circulares

Los centroides de cada círculo pueden ser facilmente calculados con las siguientes expresiones.

$$\boldsymbol{X}_c = \frac{\sum_{i=1}^{n} \bar{x}_i A_i}{\sum_{i=1}^{n} A_i}; \qquad \boldsymbol{Y}_c = \frac{\sum_{i=1}^{n} \bar{y}_i A_i}{\sum_{i=1}^{n} A_i}; \qquad \boldsymbol{Z}_c = \frac{\sum_{i=1}^{n} \bar{z}_i A_i}{\sum_{i=1}^{n} A_i} \tag{83}$$

La orientación de los elementos circulares pueden ser calculados obteniendose la normal al plano del círculo equivalente mencionado en el inciso anterior. Si la ecuación del plano es:

$$\boldsymbol{z = ax + by + c} \tag{84}$$

o también puede ser expresado como:

$$\boldsymbol{f(x, y, z) = ax + by + c - z} \tag{85}$$

entonces es posible expresar

$$\frac{\partial f(x,y,z)}{\partial x} = \boldsymbol{a} \tag{86}$$

$$\frac{\partial f(x,y,z)}{\partial y} = \boldsymbol{b} \tag{87}$$

$$\frac{\partial f(x,y,z)}{\partial z} = \boldsymbol{-1} \tag{88}$$

Si $k \bigtriangledown f(x, y, z) = \hat{n}$ **donde** $\hat{n}$ **es el vector unitario normal al plano, entonces** $k^2(1 + a^2 + b^2) = 1$ **de tal manera que:**

$$\boldsymbol{k} = \frac{1}{\sqrt{1+a^2+b^2}} \tag{89}$$

$$\boldsymbol{n}_x = \boldsymbol{ak} \tag{90}$$

$$\boldsymbol{n}_y = \boldsymbol{bk} \tag{91}$$

$$\boldsymbol{n}_z = \boldsymbol{-k} \tag{92}$$

Para poder obtener los valores correspondientes de a, b y c, se requiere tener por lo menos tres puntos para que así pueda quedar definido el plano; sin embargo, en nuestros problemas de discretización tenemos un número mayor de puntos que se encuentran en el círculo en estudio, de tal manera que la ecuación 84 se puede expresar como:

$$\begin{bmatrix} \boldsymbol{x}_1 & \boldsymbol{y}_1 & \mathbf{1} \\ \boldsymbol{x}_2 & \boldsymbol{y}_2 & \mathbf{1} \\ \boldsymbol{x}_3 & \boldsymbol{y}_3 & \mathbf{1} \\ \vdots & \vdots & \vdots \\ \boldsymbol{x}_n & \boldsymbol{y}_n & \mathbf{1} \end{bmatrix} \begin{Bmatrix} \boldsymbol{a} \\ \boldsymbol{b} \\ \boldsymbol{c} \end{Bmatrix} = \begin{Bmatrix} \boldsymbol{z}_1 \\ \boldsymbol{z}_2 \\ \boldsymbol{z}_3 \\ \vdots \\ \boldsymbol{z}_n \end{Bmatrix} \tag{93}$$

Si la ecuación 93 se premultiplica por la matriz traspuesta de la primera parte, entonces se tiene la siguiente ecuación:

$$\begin{bmatrix} \sum_{i=1}^{n} (\boldsymbol{x}_i)^2 & \sum_{i=1}^{n} (\boldsymbol{x}_i \boldsymbol{y}_i) & \sum_{i=1}^{n} (\boldsymbol{x}_i) \\ \sum_{i=1}^{n} (\boldsymbol{x}_i \boldsymbol{y}_i) & \sum_{i=1}^{n} (\boldsymbol{y}_i)^2 & \sum_{i=1}^{n} (\boldsymbol{y}_i) \\ \sum_{i=1}^{n} (\boldsymbol{x}_i) & \sum_{i=1}^{n} (\mathbf{y}_i) & \boldsymbol{n} \end{bmatrix} \begin{Bmatrix} \boldsymbol{a} \\ \boldsymbol{b} \\ \boldsymbol{c} \end{Bmatrix} = \begin{Bmatrix} \sum_{i=1}^{n} (\boldsymbol{x}_i \boldsymbol{z}_i) \\ \sum_{i=1}^{n} (\boldsymbol{y}_i \boldsymbol{z}_i) \\ \sum_{i=1}^{n} (\boldsymbol{z}_i) \end{Bmatrix} \tag{94}$$

Resolviendo esta ecuación como simultánea, el vector unitario normal queda bien definido

$$\hat{\boldsymbol{n}} = (\boldsymbol{ak}\,,\ \boldsymbol{bk}\,,\ \boldsymbol{-k}) \tag{95}$$

Un ejemplo de la orientación de estos elementos circulares en la discretización de la cuenca de Granada, España, se puede observar en la siguiente figura 4.3.

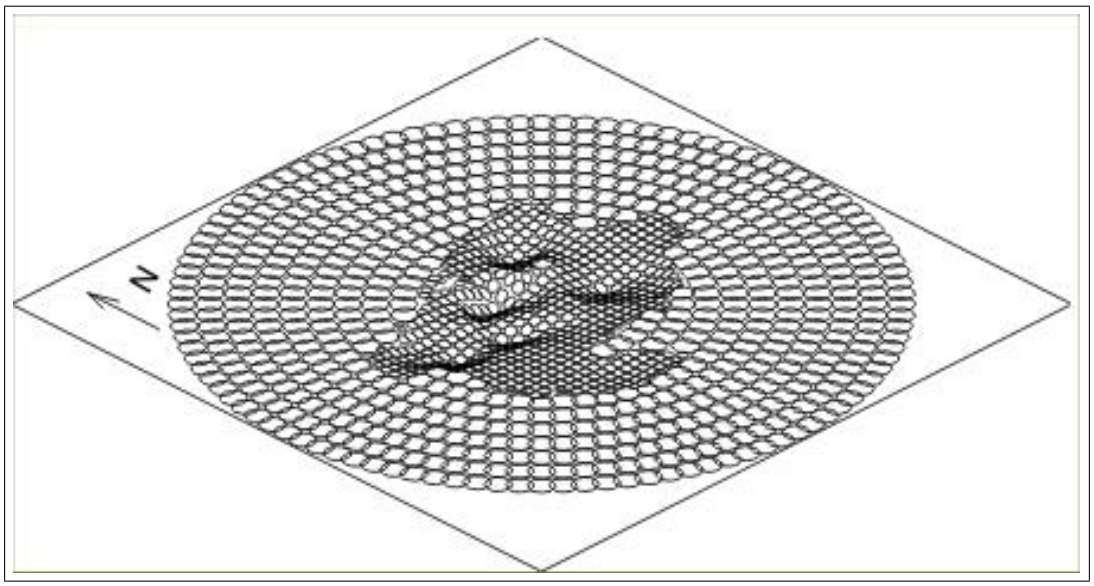

Figura 4.3; Cuenca de Granada, España

Capítulo 5

5. Formulación para la solución de las ecuaciones integrales

Varios métodos se han desarrollado usando ecuaciones integrales en la frontera para simular la propagación de ondas sísmicas para una geológia compleja, Hatayama y Fujiwara (1998). Una reducción importante y relativamente fácil se puede encontrar en el artículo de Sánchez-Sesma (1996). Un factor común en todos estos métodos de simulación, es que requieren de la solución de grandes sistemas de ecuaciones lineales para poder expresar las condiciones de frontera. El tamaño de estos sistemas es bastante considerable y está en función al tamaño de la geometria del valle en estudio y a la frecuencia máxima a la que se desea llegar a simular la propagación de ondas sísmicas. En el caso de problemas realistas en configuraciones irregulares se necesitó investigar a fondo la estructura de la composición matricial de estos sistemas con el objeto de economizar los recursos de cómputo, tanto en velocidad como en la capacidad de memoria RAM. Aquí la principal forma de resolver el problema fue con el algoritmo de condensación estática de matrices y aunque se intentaron otras alternativas, no se obtubierón mejores resultados.

De las ecuaciones 43 a la 46, resumiendo un valle aluvial en un semiespacio si la región exterior se denomina como E y la parte ocupada por el valle aluvial por la región R y suponiendo una excitación armónica, los desplazamientos refractados dentro de la cuenca se expresan como:

$$\boldsymbol{u}_i^r\ (\boldsymbol{x}) = \int_{S_R} \boldsymbol{\phi}_j^R(\boldsymbol{\xi}) \boldsymbol{G}_{ij}^R(\boldsymbol{x}, \boldsymbol{\xi})\, \boldsymbol{dS}_\xi \tag{96}$$

Donde $G_{ij}^R(x, \xi)$ es la función de Green en la región elástica R. Esta función es el desplazamiento producido en la dirección i en x, debido a la aplicación de una fuerza lineal armónica en el punto ξ en la dirección j . Esta ecuación puede ser obtenida a partir de la identidad de Somigliana (Sánchez-Sesma y

Campillo, 1991). En el caso de ondas difractadas en el campo libre se expresa de la siguiente manera:

$$\boldsymbol{u_i(x) = u_i(x)^0 + u_i\,(x)^d + \int\limits_{S_E} \phi_j^E(\xi)\, G_{ij}^E(x,\xi)\, dS_\xi} \tag{97}$$

Donde $u_i(x)^{(0)}$ está asociado con el campo libre, $u_i(x)^{(d)}$ es el desplazamiento de las ondas difractadas; por otra parte las tracciones pueden ser obtenidas directamente de la aplicación de la ley de Hooke y por las consideraciones de equilibrio alrededor e interior de las frontera.

$$\boldsymbol{t_i(x) = k\phi_i\,(x) + \int\limits_{S} \phi_j(\xi)\, T_{ij}(x,\xi)\, dS_\xi} \tag{98}$$

Donde $T_{ij}(x,\xi)$ es la función de la tracción de Green; k es igual a cero si x no está en la frontera e igual a 1/2 o -1/2 si x tiende a la frontera por dentro o fuera de espacio relativamente. Las condiciones de frontera tanto para la región E como R quedan determinadas de la siguiente forma:

Para los desplazamientos

$$\boldsymbol{u_i^r(x) = u_i^0(x) + u_i^d(x)} \tag{99}$$

$$\boldsymbol{\int\limits_{S_R} \phi_j^R(\xi)\, G_{ij}^R(x,\xi)\, dS_\xi = u_i^0\,(x) + \int\limits_{S_E} \phi_j^E(\xi)\, G_{ij}^E(x,\xi)\, dS_\xi} \tag{100}$$

Para las tracciones

$$\boldsymbol{t_i^r(x) = t_i^0(x) + t_i^d(x)} \tag{101}$$

$$\boldsymbol{k\phi_i^R\,(x) + \int\limits_{S_R} \phi_j^R(\xi)\, T_{ij}^R(x,\xi)\, dS_\xi = t_i^0(x) + k\phi_i^E\,(x) + \int\limits_{S_E} \phi_j^E(\xi)\, T_{ij}^E(x,\xi)\, dS_\xi} \tag{102}$$

para las tracciones de la superficie libre y el semiespacio

$$\boldsymbol{t}_i^0(\boldsymbol{x}) + \boldsymbol{t}_i^d(\boldsymbol{x}) \quad = \mathbf{0} \tag{103}$$

$$\boldsymbol{t}_i^0(\boldsymbol{x}) + \boldsymbol{k}\boldsymbol{\phi}_i^E\,(\boldsymbol{x}) + \int_{S_E} \boldsymbol{\phi}_j^E(\boldsymbol{\xi})\boldsymbol{T}_{ij}^E(\boldsymbol{x},\boldsymbol{\xi})\,d\boldsymbol{S}_\xi \quad = \quad \mathbf{0} \tag{104}$$

Para la superficie libre exterior

$$\boldsymbol{t}_i^r(\boldsymbol{x}) \quad = \mathbf{0} \tag{105}$$

$$\boldsymbol{k}\boldsymbol{\phi}_i^R\,(\boldsymbol{x}) + \int_{S_R} \boldsymbol{\phi}_j^R(\boldsymbol{\xi})\boldsymbol{T}_{ij}^R(\boldsymbol{x},\boldsymbol{\xi})\,d\boldsymbol{S}_\xi \quad = \quad \mathbf{0} \tag{106}$$

5.1. Discretización de la superficie

Si se considera M, L y K como el número de elementos en la discretización, la parte plana del semiespacio E, la interface común compartida por los espacios E y R, finalmente la superficie libre de la región R, respectivamente. Es claro que el número total de ecuaciones es de $3M + 6L + 3K$, con el mismo número de incognitas ${\phi_i}^{R,E}$. Si suponemos que las densidades de fuerza ${\phi_i}^{R,E}$ son constantes sobre cada uno de los elementos de frontera de tal manera que los desplazamientos pueden expresarse donde $N = M + L$

$$\boldsymbol{u}_i^d(\boldsymbol{x}) \quad = \quad \sum_{l=1}^{N} \boldsymbol{\phi}_j^E(\boldsymbol{\xi}_l)\boldsymbol{g}_{ij}^E(\boldsymbol{x},\boldsymbol{\xi}_l) \tag{107}$$

$$\boldsymbol{g}_{ij}^E(\boldsymbol{x},\boldsymbol{\xi}_l) \quad = \quad \int_{\Delta S_l} \boldsymbol{G}_{ij}^E(\boldsymbol{x},\boldsymbol{\xi}_l)\,d\boldsymbol{S}_\xi \tag{108}$$

Las tracciones como:

$$\boldsymbol{t}_i^d(\boldsymbol{x}) \quad = \quad \sum_{l=1}^{N} \boldsymbol{\phi}_i^E(\boldsymbol{x}) + \int_{S_E} \boldsymbol{\phi}_j^E(\boldsymbol{\xi})\, \boldsymbol{T}_{ij}^E(\boldsymbol{x},\boldsymbol{\xi})\, d\boldsymbol{S}_\xi \tag{109}$$

$$\boldsymbol{t}_{ij}^E(\boldsymbol{x}_n,\boldsymbol{\xi}_l) \quad = \boldsymbol{k}\boldsymbol{\delta}_{ij}\boldsymbol{\delta}_{nl} + \int_{\Delta S_l} \boldsymbol{T}_{ij}^R(\boldsymbol{x}_n,\boldsymbol{\xi}_l)\, d\boldsymbol{S}_\xi \tag{110}$$

La ecuación 109 puede calcularse numéricamente con integración Gaussiana, excepto donde $x_n = \xi_l$, en tal caso se tiene:

$$\boldsymbol{t}_{ij}^E(\boldsymbol{x}_n,\boldsymbol{\xi}_l) = \boldsymbol{k}\boldsymbol{\delta}_{ij} \tag{111}$$

de manera compacta todas estas ecuaciones se concentran en el sistema de ecuaciones siguiente:

$$\sum_{l=1}^{N} \boldsymbol{\phi}_j^E(\boldsymbol{\xi}_l)\boldsymbol{t}_{ij}^E(\boldsymbol{x},\boldsymbol{\xi}_l) = \boldsymbol{0} \tag{112}$$

$$\sum_{l=1}^{N} \boldsymbol{\phi}_j^E(\boldsymbol{\xi}_l)\boldsymbol{t}_{ij}^E(\boldsymbol{x},\boldsymbol{\xi}_l) - \sum_{l=1}^{N} \boldsymbol{\phi}_j^R(\boldsymbol{\xi}_l)\boldsymbol{t}_{ij}^R(\boldsymbol{x},\boldsymbol{\xi}_l) = -\boldsymbol{t}_i^0(\boldsymbol{x}) \tag{113}$$

$$\sum_{l=1}^{N} \boldsymbol{\phi}_j^E(\boldsymbol{\xi}_l)\boldsymbol{g}_{ij}^E(\boldsymbol{x},\boldsymbol{\xi}_l) - \sum_{l=1}^{N} \boldsymbol{\phi}_j^R(\boldsymbol{\xi}_l)\boldsymbol{g}_{ij}^R(\boldsymbol{x},\boldsymbol{\xi}_l) = -\boldsymbol{u}_i^0(\boldsymbol{x}) \tag{114}$$

$$\sum_{l=1}^{N} \boldsymbol{\phi}_j^R(\boldsymbol{\xi}_l)\boldsymbol{t}_{ij}^R(\boldsymbol{x},\boldsymbol{\xi}_l) = \boldsymbol{0} \tag{115}$$

Esta forma fue usada por Sánchez-Sesma y Luzón, (1995), con la que obtuvieron las expresiones analíticas de las funciones de Green y la estructura de este sistema de ecuaciones se puede observar en la figura 5.1

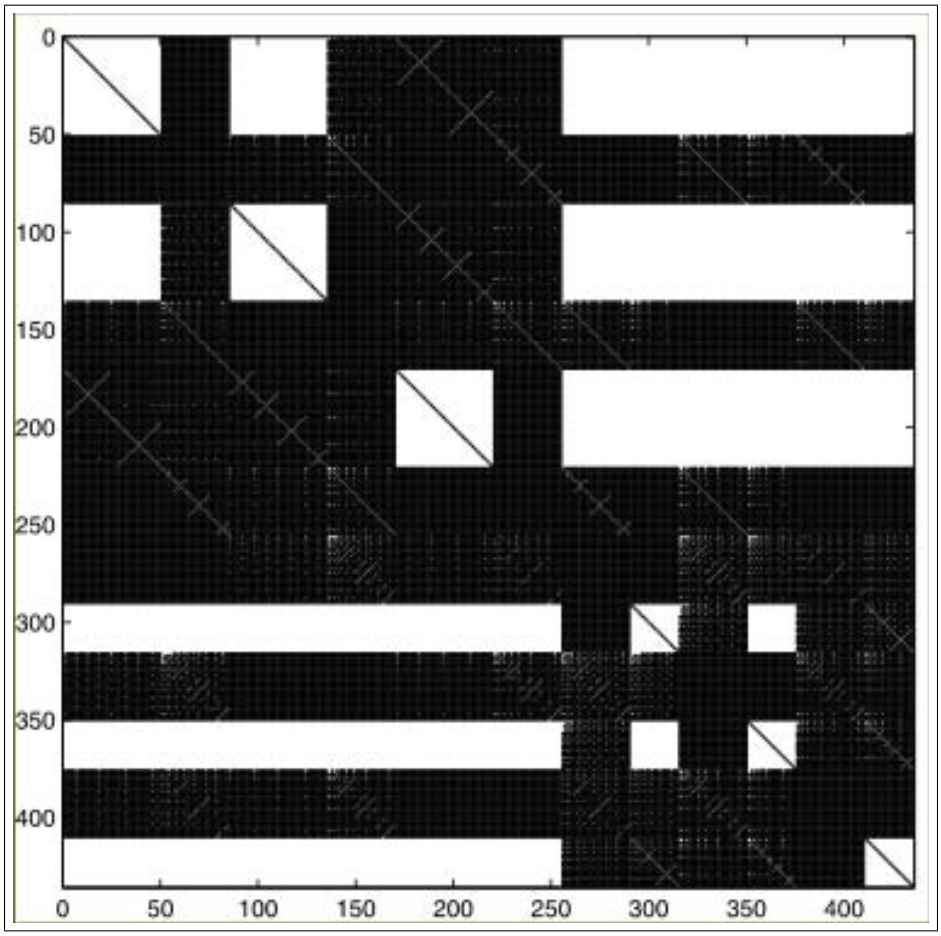

Figura 5.1; Estructura de matriz original

5.2. Condensación estática de matrices

Haciendo cambios de renglones y columnas utilizando las reglas del álgebra lineal, fue posible encontrar una nueva estructura de esta matriz y queda de la siguiente manera, figura 5.2

En este nuevo formato se puede apreciar la matriz con bloques perfectamente definidos incluyendo bloques completamente vacíos, lo cual facilita sustancialmente la solución de este sistema de ecuaciones lineales utilizando el método de condensación estática, si esta matriz se subdivide en 16 submatrices entonces puede quedar representada de la siguiente forma:

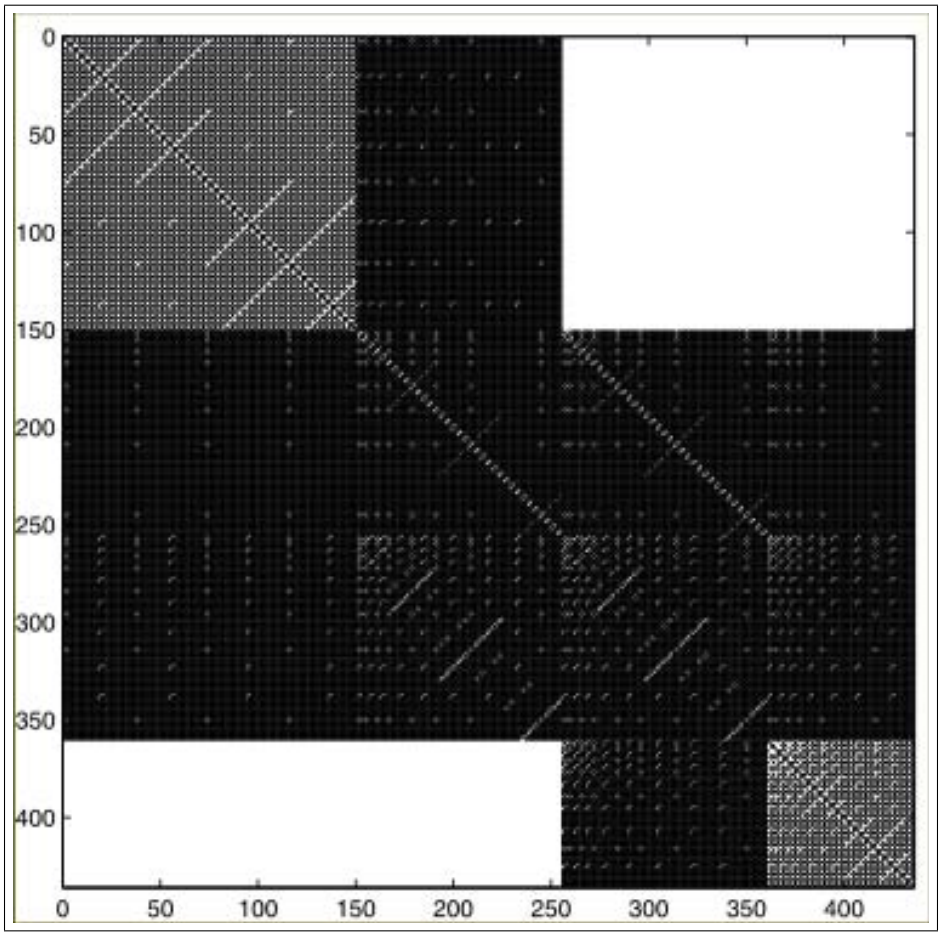

Figura 5.2; Estructura de matriz arreglada

$$\begin{bmatrix} \boldsymbol{T}_{M_E M_E} & \boldsymbol{T}_{M_E L_E} & \mathbf{0}_{M_E L_R} & \mathbf{0}_{M_E M_E} \\ \boldsymbol{T}_{L_E M_E} & \boldsymbol{T}_{L_E L_E} & \boldsymbol{T}_{L_E L_R} & \boldsymbol{T}_{L_E K_E} \\ \boldsymbol{G}_{L_R M_E} & \mathbf{G}_{L_R L_E} & \boldsymbol{G}_{L_R L_R} & \boldsymbol{G}_{L_R K_R} \\ \mathbf{0}_{K_R M_E} & \mathbf{0}_{K_R L_E} & \boldsymbol{T}_{K_R L_R} & \boldsymbol{T}_{K_R K_R} \end{bmatrix} \begin{Bmatrix} \phi_{M_E} \\ \boldsymbol{\phi}_{L_E} \\ \boldsymbol{\phi}_{L_R} \\ \phi_{K_R} \end{Bmatrix} = \begin{Bmatrix} \mathbf{0}_{M_E} \\ -\boldsymbol{t}_{L_E} \\ -\boldsymbol{u}_{L_R} \\ \mathbf{0}_{K_R} \end{Bmatrix} \tag{116}$$

Donde $0_{M_E L_R}$, $0_{M_E M_E}$, $0_{K_R M_E}$, $0_{K_R L_E}$ son matrices nulas, la ecuación anterior puede resolverse con nuevos y más pequeños sistemas de ecuaciones:

$$[T_{M_E M_E}]\,[P_1] = [T_{M_E L_E}] \tag{117}$$

$$[T_{K_R K_R}]\,[P_2] = [T_{K_R L_R}] \tag{118}$$

donde $[P_1]$ y $[P_2]$ son incógnitas que pueden resolverse como ecuaciones simultáneas, ahora es posible expresar:

$$\begin{aligned}
[Q_{11}] &= [T_{L_E L_E}] - [P_1]\,[T_{L_E M_E}] && (119)\\
[Q_{12}] &= [T_{L_E L_R}] - [P_2]\,[T_{L_E K_R}] && (120)\\
[Q_{21}] &= [G_{L_R L_E}] - [P_1]\,[G_{L_R M_E}] && (121)\\
[Q_{22}] &= [G_{L_R L_R}] - [P_2]\,[G_{L_R K_R}] && (122)
\end{aligned}$$

Donde $[Q_{11}]$, $[Q_{12}]$, $[Q_{21}]$, $[Q_{22}]$ son matrices que fácilmente pueden calcularse de tal manera que se tiene un nuevo sistema de ecuaciones:

$$\begin{bmatrix} \boldsymbol{Q}_{11} & \boldsymbol{Q}_{12} \\ \boldsymbol{Q}_{21} & \boldsymbol{Q}_{22} \end{bmatrix} \begin{Bmatrix} \boldsymbol{\phi}_{L_E} \\ \boldsymbol{\phi}_{L_R} \end{Bmatrix} = \begin{Bmatrix} -\boldsymbol{t}_{L_E} \\ -\boldsymbol{u}_{L_R} \end{Bmatrix} \tag{123}$$

resolviendo el sistema, entonces ϕ_{L_E} y ϕ_{L_R} son conocidos, finalmente pueden calcularse las últimas incógnitas con las siguientes ecuaciones:

$$\begin{aligned}
\{\phi_{M_E}\} &= -[P_1]\,\{\phi_{L_E}\} && (124)\\
\{\phi_{K_R}\} &= -[P_2]\,\{\phi_{L_R}\} && (125)
\end{aligned}$$

Para la solución de estas ecuaciones es posible escribir un programa de computadora en donde el almacenamiento de las matrices sea de tipo virtual, es decir no hace falta guardar las matrices, es mejor calcular los coeficientes de las mismas cada vez que se necesite y de esta manera existe un buen ahorro de memoria RAM, y así es posible resolver problemas realistas a una frecuencia mayor comparado con la solución con métodos tradicionales. Este algoritmo fue utilizado para resolver los problemas realistas de los apéndices A y B en las cuencas de Granada y Zafarraya respectivamente.

Conclusiones

Debido a los trabajos de optimación numérica realizados en esta tesis, ha sido posible llevar a cabo la simulación sísmica 3D bajo la incidencia de ondas planas en configuraciones completamente irregulares realistas en las cuencas de Granada y Zafarraya, España, permitiendo que los algorítmos aquí presentados sean fácilmente adaptados a la programación en paralelo utilizando memoria dinámica y en muchos de los casos se presenta almacenamiento de matrices virtuales, es decir se calculan, pero no se guardan ni en memoria RAM ni en memoria ROM, obteniéndose una velocidad de proceso aún mayor, ya que la tecnología en cuanto al almacenamiento de datos no ha avanzado sustancialmente. Es por ello que resulta más eficiente calcular y recalcular cuantas veces se necesite una información en lugar de almacenarla y posteriormente leerla, pues los procesos electróncos y numéricos de cálculo resultan más veloces y eficientes.

En los apéndices A y B se tienen los resultados publicados de las cuencas de Granada y Zafarraya, en donde se concluye que los sistemas lineales de ecuaciones al reordenarse adecuadamente intercambiando filas y columnas respectivamente en una matriz compuesta por bloques bien definidos, en donde cuatro bloques quedan definidos como nulos, los que pueden ser completamente eliminados de todo cálculo; se observa que la utilización de la condensación estática de las matrices es más eficiente y estable que los métodos iterativos como es el caso del gradiente conjugado y el gradiente biconjugado, siendo esto eficiente para frecuencias muy bajas, pero en cuanto las frecuencias van en aumento estos métodos resultan con una convergencia sumamente lenta, llegando a un punto donde la solución ya no es factible, lo cual no sucede con la condensación estática de matrices que siempre utiliza soluciones directas y exactas hasta donde llega la precisión del sistema de cómputo. Con este modelo se permite utilizar los mismos recursos computacionales a frecuencias más altas, poniendo enfacis en los problemas 3D.

En el caso de la cuenca de Granada, se analizaron los resultados tanto en el dominio de la frecuencia como en el del tiempo y para el rango de frecuencias que fue posible calcular, se ha observado que los efectos de sitio más relevantes son debido a amplificaciones locales producidos dentro de los sedimentos. Para

las ondas SH, el factor de amplificación se incrementa a valores cerca de diez veces la amplitud de la onda incidente para ciertas frecuencias específicas. Por otra parte, para el periodo característico considerado en este trabajo para la incidencia de ondad P con un pulso de Ricker, las amplificaciones en ciertos tiempos específicos y posiciones llegan a ser de ocho. En general, para la incidencia de ondas planas consideradas en este trabajo, los niveles de amplificación no son muy grandes debido al contraste de impedancia entre los sedimentos y la roca (2.5) es relativamente bajo.

En el caso de la cuenca de Zafarraya, utilizando los mismos procedimientos anteriores, se encontró que para la incidencia de ondas SH produce importantes amplitudes en los receptores localizados al sur del modelo en los tres componentes del movimiento; por ejemplo, algunos desplazamientos observados en el movimiento radial son aproximadamente iguales al valor máximo esperado para la componente transversal cuando un modelo 1D de la cuenca de Zafarraya es usado. Los sismogramas calculados para ondas incidentes SV muestran que el movimiento horizontal (transverso y radial) es amplificado enormemente tanto en amplitud como en duración en los receptores, donde las profundidades de la cuenca son mayores. Algunas de las ondas que han producido el incremento en la duración son interpretadas como ondas superficiales y sus reflecciones en las orillas de la cuenca, las que producen patrones característicos de polarización mostrando la particular rotación en los planos horizontal y radial.

Finalmente, una de las más importantes concluciones que se obtuvieron, es que un modelo simple en 3D nos permite encontrar interesantes efectos de sitio que podrían influir en el movimiento sismico de las cuencas de Granada y Zafarraya. Estos resultados pueden ser preliminares, pues indican que es necesario tomarlos en cuenta en las características 3D de la naturaleza de estas cuencas y que deben estimular futuras investigaciones.

Una de las limitantes encontradas en este trabajo es sin duda cuando se desea alcanzar grandes frecuencias, ya que las necesidades de cómputo se incrementan de manera cuadrática o en el caso de cuencas muy grandes, como lo ha sido la cuenca de Granada con un diámetro promedio de 52 km, solamente se llegó a una frecuencia máxima de 0.312 Hz.

Bibliografía

Abramowitz M, Stegun IA. Handbook of mathematical functions. New York: Dover:1972.

Aki, K., (1988). Local site effects on strong ground motion, in Earthquake Engineering and Soil Dynamics II-Recent Advances in Ground Motion Evaluation, ed. J. Lawrence Von Thun, American Society of Civil Engineering, 103-155.

Aki, K., Larner K.L.. Surface motion of a layered medium having an irregular interface due to incident plane SH waves. J Geophys Res 197; 75: 1921 - 41.

Aki K., Richards P.G.. Quiantitative seismology. Theory methods. San Francisco: W. H. Freeman; 1980.

Bard, P.-Y., and M. Bouchon, (1980). The seismic response of sediment-filled valleys. Part 1. The case of incident SH waves, Bulletin of the Seismological Society of America. 70, 4, 1263-1286.

Bard, P.Y., and M. Bouchon, (1980). The seismic response of sediment-filled valleys. Part 2. The case of incident P and SV waves, Bulletin of the Seismological Society of America. 70: 1921-41.

Beskos, D.E., Boundary element methods in dynamic analysis. Applied Mechanics Review. 1987; 40:1 - 23.

Beskos, D.E., Boundary element methods in dynamic analysis. Part II (1986 -1996) Applied Mechanics. Review. 1997; 50:149 - 97.

Bouchon, M., Campillo M., Gaffet S., A boundary integral equation - dicrete wavenumber representation method to study wave propagation in multilayered media having irregular interfaces. Geophysical Journal International. 1989; 54:1134 - 40.

Bravo M.A., Sánchez-Sesma F.J., Chávez-García, F.J., Ground motion on stratified alluvial deposits for incident SH waves. Bulletin of the Seismological Society of America. 1988; 78: 436 - 50.

Canas, J. A., F. De Miguel, F. Vidal, and G. Alguacil, (1988). Anelastic Rayleigh wave attenuation in the Iberian Peninsula, Geophysical Journal International. 95, 391-396.

Chávez-García, F.J., J. Castillo and W.R. Stephenson, (2002). 3D site effects: a thorough analysis of a high.quality dataset. Bulletin of the Seismological Society of America. 92, 1941-1951.

Chirlaque, M., Díaz, M., García, A.J., García, E., Guillén, F., Jiménez, J.C., (1987). Estudio geoeléctrico del polje de Zafarraya. Facultad de Ciencias, Departamento de Geodinámica. University of Granada, Spain, 129 pp. In spanish.

De Miguel, F., F. Vidal, G. Alguacil, and J.M. Guirao, (1989). Spatial and energetics trends of the microearthquakes activity in the central Betics, Geodinamica Acta, 3, 87-94.

Frankel, A., (1993). Three-dimensional simulations of ground motions in the San Bernardino Valley, California, for hypothetical earthquakes on the San Andreas fault, Bulletin of the Seismological Society of America. 83, 1020-1041.

Frankel, A., and W. Stephenson, (2000). Three-dimensional simulations of ground motions in the Seattle region for earthquakes in the Seattle fault zone, Bulletin of the Seismological Society of America. 90, 1251-1267.

García Dueñas, V., and J. C. Balanyá, (1986). Estructura y naturaleza del arco de Gibraltar. Maleo-Bol. Inf. Sociedad Geológica de Portugal 2, 23. In Spanish.

Gil-Zepeda, S. A, Luzón, F., Aguirre, J., Morales, J., Sánchez-Sesma, F. J., and Ortiz, C., 3D Seismic Response of the deep basement-structure of the Granada basin (Southern Spain), Bulletin of the Seismological Society of America. 2002; Vol 92; No 6: 2163 - 2176.

Gil-Zepeda, S. A, Montalvo-Arrieta, J. C., Vai, R., Sánchez-Sesma, F. J., A hibrid indirect boundary element–discrete wave number method applied to simulate the seismic response of stratified alluvial valleys. Soil Dynamics and Earthquake Engineering, 2003; 23:77 -86.

Haskell N.A., Dispersion of surface waves on multilayered media. Bulletin of the Seismological Society of America. 1953; 43: 17 - 34.

Hatayama, K., and H. Fujiwara, (1998). Excitation of secondary Love and Rayleigh waves in a three-dimensional sedimentary basin evaluated by the direct boundary element method with normal modes, Geophysical Journal International. 133,2, 260-278.

Hill, J., H., Benz, M., Murphy, and G.T. Schuster, (1990). Propagation and resonance of SH waves in the Salt Lake Valley, Utah. Bulletin of the Seismological Society of America. 80, 23-42.

Horike, M., (1985). Inversion of phase velocity of long-period microtremors to the S-wave-velocity structure sown to the basement in urbanized areas. Journal Physics of Earth. 33, 59-96.

Ibáñez, J., J. Morales, F. De Miguel, F. Vidal, G. Alguacil, and A. Posadas, (1991). Effect of a sedimentary basin on

estimations of Q_c and Q_{Lg}. Physics of Earth Planet International. 66, 244-252.

Ibáñez, J.M., C. Bottari, J.A. Esquivel, J. Morales, and G. Alguacil, (2001). Magnitude-intensity relations for instrumental and historical (IX-XIX century) earthquakes in south Spain. Tectonical and seismic hazard implications. Bulletin of the Seismological Society of America. (submitted).

Kagawa, T., and Group for Spanish-Japanese joint work on microzonation of Granada basin (1996). Microtremor array observation in the Granada basin, Southern Spain. Homenaje en Honor del Profesor Fernando de Miguel Martínez. Eds. F. Vidal, M. Espinar y J.A. Esquivel. Universidad de Granada, pp.287-304. In Spanish

Kawase, H, Aki, K., A study on the response of a soft basin for incident, S, P and Rayleigh waves with special refenrence to the log duration observed in Mexico City. Bulletin of the Seismological Society of America. 1989; 54: 1134 - 40.

Kawase, H., Time-domain response of a semicircular canyon for incident SV, P and Rayleigh waves calculated by the discrete wavenumber boundary element Method. Bulletin of the Seismological Society of America. 1988; 78: 1415 - 37.

Kouoh-Bille, L., Sánchez-Sesma, FJ, Wirgin, A., Response resonante d'u'une montagne cylindrique a une onde sismique SH. CR Acad Sci Paris 1991;312(II): 849 - 54.

Kupradze, V. D., Dynamical problems in elasticity. In; Sneddon IN, Hill R, editors. Progress in solid mechanics, Vol III. Amsterdam: North Holland; 1963.

Luzón, F., (1995). Determinación de la respuesta sísmica de estructuras geológicas superficiales mediante el método indirecto de elementos en la frontera, Ph. D. thesis, University of Granada, Spain. In spanish.

Luzón, F., F. J. Sánchez-Sesma, J. L. Rodríguez-Zúñiga, A. M. Posadas, J. M. García, J. Martín, M. D. Romacho, and M. Navarro, (1997). Diffraction of P, S and Rayleigh waves by three-dimensional topographies, Geophysical Journal International. 129, 571-578.

Luzón, F., F.J. Sánchez-Sesma, A. Gil-Zepeda, A. Posadas and M. Navarro, (1999). Seismic response of 3D topographical irregularities under incoming elastic waves from point sources, Physics Chem. Earth (A), 24, 3, 231-234.

Luzón, F., L. Ramírez, F.J. Sánchez-Sesma, and A. Posadas, (2001). Simulation of the seismic response of sedimentary basins with vertical constant-gradient of velocity. Pure Applied Geophysics. Submitted.

Luzón, F., Gil-Zepeda, A., Sánchez-Sesma, F.J., (2004). Three-dimensional simulation of ground motion in the Zafarraya Basin (Southern Spain) up to 1.335 Hz under incident plane waves. Geophysical Journal International,156; 584 - 594.

Manolis, G. D., Beskos, D. E., Boundary elemnt methods in elastodynamics. London: Unwin Hyman Ltd: 1988.

Morales, J., F. Vidal, F. De Miguel, G. Alguacil, A. Posadas, J. Ibáñez, Guzmán and Guirao, (1990). Basement structure of the Granada basin, Betic Cordilleras, Southern Spain, Tectonophysics 177, 337-348.

Morales, J., (1991). Caracterización de la respuesta sísmica local en las cuencas de Granada (España) y Ciudad Guzmán (México) mediante el análisis espectral de microterremotos y terremotos. PhD Thesis. University of Granada (Spain), 276 pp. In Spanish.

Morales, J., F. Vidal, J. Peña, G. Alguacil and J. Ibáñez, (1991). Microtremor study in the sediment filled basin of Zafarraya, Granada (Southern Spain), Bulletin of the Seismological Society of America. 81, 687-693.

Morales, J., K., Seo, T., Samano, J. A., Peña, J., Ibáñez, and Vidal, F., (1993). Site response on seismic motion in the Granada basin (Southern Spain) based on microtremor measurement, Journal of Physics of Earth. 41, 221-238.

Morales, J., S. K. Singh, and M. Ordaz, (1996). Analysis of Granada, Spain earthquake of 24 june, 1984 (M = 5) with emphasis on seismic hazard in the Granada basin, Tectonophysics 257, 253-263.

Norma de Construcción Sismorresistente NCSE-94, (1995). Boletín Oficial del Estado, February 8. Ministerio Obras Públicas, Transportes y Medio Ambiente, 3935-3980. In Spanish.

Olsen, K. B., (2000). Site amplification in the Los Angeles basin from three-dimensional modeling of ground motion. Bulletin of the Seismological Society of America. 90, 6B, S77-S94.

Olsen, K. B., and R. J. Archuleta, (1996). Three-dimensional simulation of earthquakes on the Los Angeles fault system. Bulletin of the Seismological Society of America. 86, 575-596.

Olsen, K. B., J.C. Pechmann, and G.T. Schuster, (1995). Simulation of 3D elastic wave propagation in the Salt Lake basin. Bulletin of the Seismological Society of America. 85, 1688-1710.

Ortiz-Alemán, C., F. J. Sánchez-Sesma, J. L. Rodríguez-Zúñiga, and F. Luzón, (1998). Computing topographical 3D site effects using a fast IBEM/Conjugate gradient approach, Bulletin of the Seismological Society of America. 88, 393-399.

Papageorgiou, A. S., Kim, J., Study of the propagation and amplification of seismic waves in Caracas Valley with reference to the 29 july 1967 earthquake: SH waves. Bulletin of the Seismological Society of America. 1991; 81: 2214 -33.

Press, W.H., Teukolsky, S.A., Vetterling, W. T., and Flannery, B. P., (1992). Numerical recipes in Fortran. The art of scientific somputing. Cambridge University Press, New York.

Ramos-Martínez, J., Simulación numérica de la respuesta sísmica de valles aluviales. MSc Thesis, Institute of Geophysics, UNAM; 1992.

Reicherter, K. R., (2001). Paleoseismologic advances in the Granada basin (Betic cordilleras, Southern Spain). Acta Geológica Hispánica 36 (3/4), 278-281.

Reicherter, K., Jabaloy, A., Galindo-Zaldívar, J., Becker-Heidmann, P., and Reiss, S., (2002). Holocene palaeoseismic history of the Central Betic Cordilleras (S-Spain). Conference on Environmental Catastrophes and Recoveries in the Holocene, Brunel University, London (abstract).

Ricker, N. H., (1977). Transient waves in visco-elastic media, Elsevier Scientific Publishing Co., Amsterdam, Holland.

Rovelli, A. , L. Scognamiglio, F. Marra, and A. Caserta, (2001). Edge-diffracted 1-sec surface waves observed in a small-size intramountain basin (Colfiorito, Central Italy). Bulletin of the Seismological Society of America. 91, 1581-1866.

Rodríguez Fernández, C., C. Sanz de Galdeano, and J. Fernández, (1989). Genesis and evolution of the Granada Basin (Betic Cordillera, Spain). International Symposium on Intermontane Basins. Geology & Resources, Chiang Mai, Thailand, 294-305.

Sánchez-Sesma, F. J., Campillo, M., (1991). Diffraction of P, SV, and Rayleigh waves by topographic features: A Boundary Integral Formulation, Bulletin of the Seismological Society of America. 81, 2234-2253.

Sánchez-Sesma, F.J., J. Ramos-Martínez and M. Campillo, (1993). An indirect boundary element method applied to simulate the seismic response of alluvial valleys for incident P, S and Rayleigh Waves, Earth Engineering Structural Dynaics. 422, 279-295.

Sánchez-Sesma, F. J., and F. Luzón, (1995). Seismic response of three dimensional alluvial valleys for incident P, S and Rayleigh waves, Bulletin of the Seismological Society of America. 85, 269-284.

Sánchez-Sesma, F. J., (1996). Strong ground motion and site effects, in computer analysis of earthquake resistant structures, D. E. Beskos and S.A. Anagnostopoulos (Editors), Computer Mechanics Publications, Southampton, 200-229.

Sánchez-Sesma, F. J., Site effects on strong ground motion. Soil Dynamics Earthquake Engineering. 1987; 6: 124 - 32.

Sánchez-Sesma, F. J., Luzón, F., Seismic response of three-dimensional alluvial valleys for incident P, S and Rayleigh waves. Bulletin of the Seismological Society of America. 1995; 85:269, see also p. 284.

Sanz de Galdeano, C., and J.A. Vera, (1992). Stratigraphic record and paleogeographical context of the Neogene basins in the Betic Cordillera, Spain, Basin Research 4, 21-36.

Schenková, Z., Zahradník, J., (1996). Interpretation of the microtremor spectra at the Zafarraya basin, southern Spain. Soil Dynamics Earthquake Engineering, 15, 69-73.

Webster AG. Partial differential equations in mathematical physics. New York: Dover; 1955.

Vidal, F., (1986). Sismotectónica de la región Béticas-Mar de Alborán. PhD Thesis. University of Granada (Spain), 450 pp. In Spanish.

Zahradnik, J,. Simple elastic finite-difference scheme. Bulletin of the Seismological Society of America. 1995; 85: 1879 - 87.

Apéndice A

Respuesta sísmica 3D de la estructura del basamento profundo de la cuenca de Granada (Sur de España).

La Cuenca de Granada está localizada en el sureste de España, en un área de alta sismicidad en la Peninsula Ibérica. Esta sismicidad es debida, en parte, a los efectos de amplificación del movimiento del suelo local que ha sido observado en varias localizaciones de esta cuenca. En este trabajo, se ha utilizado el Método Indirecto de Elementos en la Frontera (IBEM por sus siglas en inglés Indirect Boundary Elements Method), para calcular la respuesta sísmica tridimensional a gran profundidad de la estructura de la Cuenca de Granada bajo la incidencia de ondas P y ondas planas S que provienen del sur, se han analizado los resultados tanto en el dominio de la frecuencia como en el tiempo, y para un rango de frecuencias entre 0 y 0.312 Hz, los efectos de sitio más relevantes son las amplificaciones locales producidas por los sedimentos, los patrones de amplificaciones observados de los desplazamientos para ondas incidentes SH son los más altos en las localizaciones en donde la cuenca tiene mayor profundidad. Para las ondas P y SV, los snapshots muestran los efectos de amplificación en las componentes radial y vertical, cuando las ondas cruzan directamente la Cuenca de Granada.

Bulletin of the Seismological Society of America, Vol. 92, No. 6, pp. 2163–2176, August 2002

3D Seismic Response of the Deep Basement Structure of the Granada Basin (Southern Spain)

by S. Alejandro Gil-Zepeda, Francisco Luzón, Jorge Aguirre, José Morales, Francisco J. Sánchez-Sesma, and Carlos Ortiz-Alemán

Abstract The Granada Basin is located in the southeast of Spain, in the central sector of the Betic Cordilleras, in an area of high seismic hazard in the Iberian Peninsula. This hazard is due, in part, to local ground-motion amplification effects that have been observed at various locations in this basin. In this work, we use the indirect boundary element method (IBEM) to compute the three-dimensional (3D) seismic response of the deep structure of the Granada Basin for incident *P*- and *S*-plane waves coming from the south. We have analyzed the results in both frequency and time domains, and for the range of frequencies that we have been able to compute (between 0 and 0.312 Hz), the most relevant site effects are the local amplifications produced inside the sediments. Generally speaking, the observed amplification patterns of the displacements for incident *SH* waves are the highest at those locations where the basin is deeper. For *P* and *SV* waves, the "snapshots" show the amplification effects of both radial and vertical components, when the direct waves cross the Granada Basin. The amplification levels, with respect to the amplitude of the incident wave, are not so large, because the impedance contrast between the sediments and the bedrock (equal to 2.45) is relatively low. Moreover, two perpendicular receiver profiles are used to analyze the wave propagation, and we have observed the propagation of phases that can be identified as surface waves along the two profiles. The Rayleigh waves propagate with more energy on the forward direction (from south to north) of the incident body wave.

Introduction

Local effects due to geological site conditions can lead to significant spatial and temporal variations of seismic ground motion, which can contribute to large structural damage during moderate to large earthquakes. Local site response has received significant attention in the past two decades, and its characterization has been performed by using both experimental and numerical analysis techniques (see, e.g., Aki, 1988, and Sánchez-Sesma, 1996). In recent years, numerical codes have been developed to deal with the seismic wave propagation in three-dimensional (3D) models (see e.g., Sánchez-Sesma and Luzón, 1995). The most realistic simulations to date are those of finite differences. In particular, 3D geometries have been considered for some sedimentary basins around the world: Olsen and Archuleta (1996) and Olsen (2000) used finite differences to simulate the ground motion in the Los Angeles Basin; Olsen *et al.* (1995) studied the propagation of *P* waves in the Salt Lake Basin; and recently, Frankel and Stephenson (2000) computed the ground motions in the Seattle region with the finite-difference method. In these and other works that used 3D realistic structures, some common phenomena, such as the generation of surface waves and localized resonances, have been observed. However, amplification patterns are generally different and are not quantitatively "portable" from one basin to another. The seismic response of each 3D basin has its own amplification levels and its own wave-motion response inside and outside the sediments. The response depends strongly on the properties of the basin, such as impedance contrast, wave velocities, and geometry of the structure. Of course, the location of the source and its rupture parameters also have significant influence in the response.

In this work, we study the seismic response of the deep structure of the Granada Basin (Fig. 1), which is located in one of the regions with the highest hazard level in the Iberian Peninsula, as shown in the Spanish seismic building code (Norma de Construcción Sismoresistente NCSE-94, 1995). Available historical records indicate that in the last 2000 years, different parts of the south of the Iberian Peninsula have been affected by major earthquakes with MSK intensities from VII to X (Reicherter, 2001). From recent history,

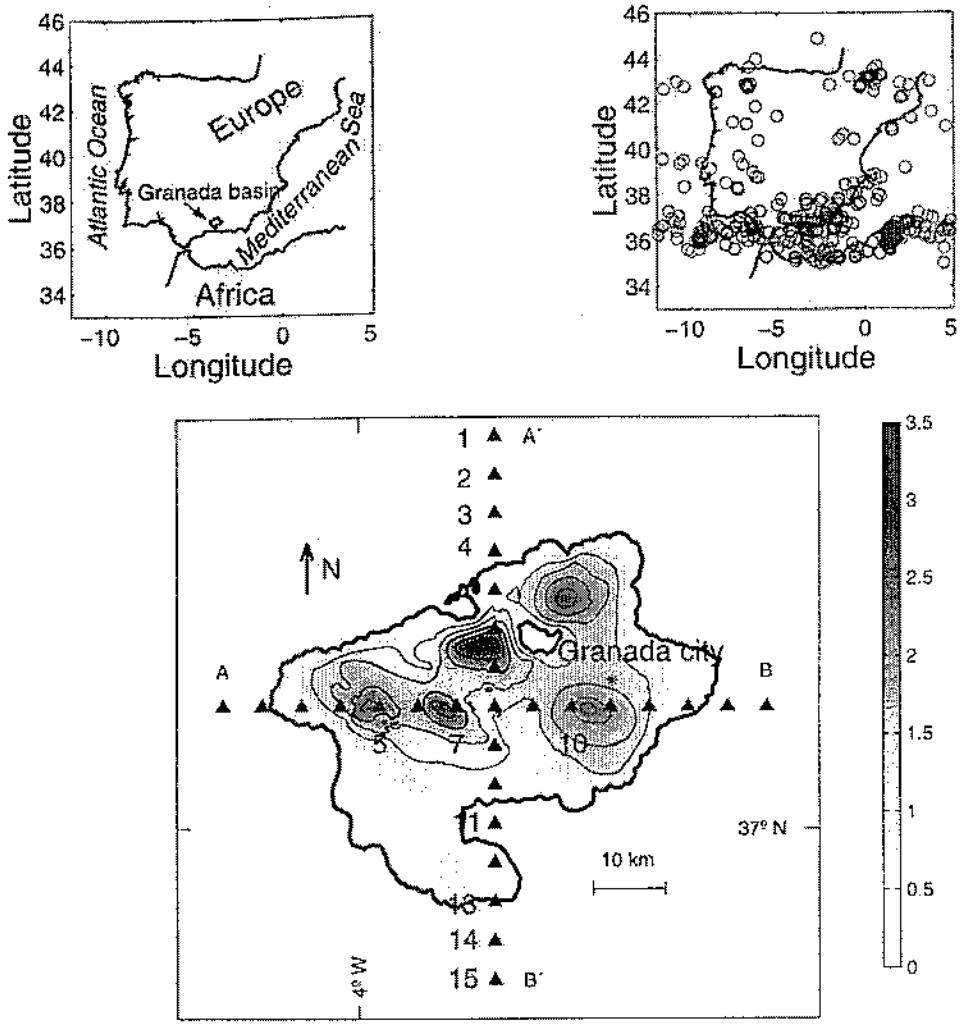

Figure 1. (Upper left): Map showing the location of the Granada Basin (Upper right): Map showing the epicenters (circles) of the region for earthquakes with magnitudes ≥4 in the period 1970–2001. (Bottom): Depth to the basement of the Granada Basin, with the locations of receivers in the profiles A–B and A′–B′. The contours have an interval of 600 m; darker shading indicates greater depth of the sediment–basement boundary. The units of the depth scale bar are in km.

the epicenters of the region for earthquakes with magnitudes ≥4 from the year 1970 to 2001 are presented in Fig. 1. Large amplifications that can be attributed to site effects have been observed in the basin (Morales, 1991). To analyze the response of the deep basement structure, we studied the amplification patterns and the snapshots of particle displacements in the free surface of a model of the Granada Basin. We also use profiles A–B and A′–B′ (Fig. 1) to illustrate part of the effects of the sedimentary basin by means of synthetic seismograms and their corresponding polarigrams. The bulk of southern Spain's seismicity comes from the intercontinental collision of Africa and Eurasia; thus, an elevated number of earthquakes are produced south of the Granada Basin. Therefore, we use incident *P* and *S* waves coming from the south as the source input to the basin for the work presented here.

The Granada Basin

The Granada Basin is located in the southeast of Spain, in the central sector of the Betic Cordilleras mountain range. It is one of the larger intramountain Neogene–Quaternary basins of the Betic ranges. Geologically, the Granada Basin is bounded to the north and to the west by sub-Betic domain materials, mainly Jurassic and Cretaceous carbonate sedimentary series belonging to the Sub-Iberic paleomargin, and to the south and east by Alpujarrides metamorphic units (schists, phyllites, and quartzites of Palaeozoic and Triassic age and marbles of the Triassic period) of the Alborán domain (García Dueñas and Balanyá, 1986). The geologic evolution of this big basin has been the subject of previous studies (see, e.g., García Dueñas and Balanyá, 1986; Rodríguez Fernández *et al.*, 1989; Morales *et al.*, 1990; Sanz de Galdeano and Vera, 1992, Reicherter, 2001).

Southern Spain has the highest seismic hazard in the Iberian Peninsula, as shown in the maximum horizontal acceleration map for a return period of 500 years (Norma de Construcción Sismoresistente NCSE-94, 1995). The contribution of seismicity to the hazard is a consequence of the lithosphere collision between the Euroasiatic and African plates on a regional scale. The Granada Basin has the highest level of microseismic activity (magnitude <3.5) in the Iberian Peninsula (De Miguel *et al.*, 1989). Most of the seismic energy is released by earthquakes with magnitudes <5.0; however, catastrophic earthquakes have occurred in the past. In fact, the destructive Andalusian earthquake of 25 December 1884 (I_0 = X) occurred near Alhama de Granada, located in the south of the Granada Basin, producing great damage throughout the region (Vidal, 1986). Furthermore, J. M. Ibáñez *et al.* (unpublished results, 2001) estimated a maximum intensity–magnitude relationship for historical earthquakes in the south of Spain and found great magnitudes of ~6.5–7.0 inside the Granada Basin (e.g., the Andalusian earthquake of 25 December 1884 with M_{Imax} 6.8; the Granada earthquake in June 1431, with M_{Imax} 6.5), and outside of it (e.g., the Baza earthquake of 3 September 1531 with M_{Imax} 6.5 located ~80 km northeast of Granada city; the Almería earthquake of 22 September 1522 with M_{Imax} 6.8, located 100 km southeast of Granada city; the Málaga earthquake of January 1494 with M_{Imax} 6.5 located ~100 km southwest of Granada city).

The 3D basement structure of the Granada Basin was established by Morales *et al.* (1990) by means of an analysis and interpretation of gravity and seismic-reflection data. In this basin (see Fig. 1), there are important depocenters with depths >3000 m. The characteristic surficial dimensions of the sedimentary deposits are ~60 km × 45 km. From the point of view of seismic hazard, local effects in the Granada Basin have been studied by using microtremors (Morales *et al.*, 1993), and coda and *Lg* waves (Ibáñez *et al.*, 1991). Moreover, Morales *et al.* (1996) used one small event, with magnitude M_w 5, as an empirical Green's function to obtain the synthetic records of a possible magnitude M_w 7.0 earthquake at various locations in the basin. The effect of the geological site conditions was reflected in the synthesized seismograms in which the peak ground acceleration reached values of ~250 cm/sec^2. The Sa_{max} of the simulated seismograms, ~0.8*g*, also pointed out the importance of site effects in the Granada Basin in the ground motion induced by moderate earthquakes.

Velocity and density 1D profiles for various zones of the Granada Basin were derived by Kagawa *et al.* (1996), using the vertical-component records from a seismometer array and the dispersion characteristics of Rayleigh waves from microtremors as proposed by Horike (1985). In our computations, we use the properties calculated by Kagawa *et al.* (1996), in which the bedrock has a mass density of 2.7 g/cm^3 and velocities of 5 and 3.2 km/sec for *P* and *S* waves, respectively. Although there is a thick, irregular surface layer with *S*-wave velocities as low as 516 m/sec, we assume homogeneous basin sediments with mean values for the elastic properties because we are interested, in principle, in the seismic response of the deep structure of the sediments. Therefore, we set the values of 2.2 g/cm^3 for mass density and 3.1 and 1.6 km/sec for *P* and *S*-wave velocities, respectively, inside the basin. To account for inelastic attenuation, we have assumed quality factors (Q) without depth or frequency dependence of 150 for both *P* and *S* waves in bedrock and of 100 for both waves inside the basin. These values have been assumed, based on the models of Q for *S* waves at depth proposed for southern Spain by Canas *et al.* (1988), who used a generalized inversion technique applied to the attenuation of Rayleigh waves.

Method and Discretization

We use the indirect boundary element method (IBEM) to compute the seismic response of the deep structure of the Granada Basin. In the IBEM, which is based on the so-called single-layer-boundary integral representation of displacements and tractions, the problems of diffraction and refraction of elastic waves are formulated in terms of boundary force densities. The boundary conditions of continuity of displacements and tractions between regions and those of null tractions at free surfaces, once discretized, lead to a system of linear equations in which the unknowns are the force densities of the boundary sources. Therefore, the method can be regarded as a numerical realization of Huygens' principle, in which the secondary sources are located on the surface boundaries. Details on this technique, in which the discretization of surfaces is achieved using circular elements and its implementation, can be found in Sánchez-Sesma and Luzón (1995).

Sánchez-Sesma and Luzón (1995) presented various examples of using the IBEM and solving the linear system of equations with the classic LU decomposition (see, e.g., Press *et al.*, 1992). However, in dealing with larger, more realistic 3D problems, some additional difficulties arise. In these calculations, to keep a reasonable ratio between the minimum wavelength and size of elements, the dimension of the coefficient matrix grows approximately with the square of frequency, and therefore the computational requirements can be too large for problems of practical interest. In a recent article, Ortiz-Alemán *et al.* (1998) overcame the problem by using threshold criteria to convert the full matrix into a sparse one and then using the biconjugate gradient method together with an iterative scheme to solve the linear system of equations. To test their approach, they satisfactorily reproduced the results of Luzón *et al.* (1997), who studied the diffraction of *P*, *S*, and Rayleigh waves by 3D topographic surfaces. On the other hand, use of the analytic Green's functions of a homogeneous full space, as is done in this work, implicitly limits the technique when the response for higher frequencies is wanted in a 3D layered basin. Nevertheless, with this technique and with the appropriate Green's functions, it is still possible, for example, to take into account a

layered structure or a medium with a velocity gradient, as has been done by F. Luzón *et al.* (unpublished results, 2001) in alluvial basins with 2D geometry with a vertical gradient of velocity.

In this work, we chose to deal with the linear system of equations obtained in the IBEM somewhat differently. We use a partitioned matrix instead of the full matrix, as did Sánchez-Sesma and Luzón (1995). We reordered rows and columns of the matrix to have block matrices and found that the system has a particular structure that can be easily constructed as

$$\begin{bmatrix} \mathbf{T}_{M_E M_E} & \mathbf{T}_{M_E L_E} & \mathbf{0}_{M_E L_R} & \mathbf{0}_{M_E K_R} \\ \mathbf{T}_{L_E M_E} & \mathbf{T}_{L_E L_E} & \mathbf{T}_{L_E L_R} & \mathbf{T}_{L_E K_R} \\ \mathbf{G}_{L_R M_E} & \mathbf{G}_{L_R L_E} & \mathbf{G}_{L_R L_R} & \mathbf{G}_{L_R K_R} \\ \mathbf{0}_{K_R M_E} & \mathbf{0}_{K_R L_E} & \mathbf{T}_{K_R L_R} & \mathbf{T}_{K_R K_R} \end{bmatrix} \begin{Bmatrix} \varphi_{M_E} \\ \varphi_{L_E} \\ \varphi_{L_R} \\ \varphi_{K_R} \end{Bmatrix} = \begin{Bmatrix} \mathbf{0}_{M_E} \\ -\mathbf{t}_{L_E} \\ -\mathbf{u}_{L_R} \\ \mathbf{0}_{K_R} \end{Bmatrix} \quad (1)$$

in which each term in the expression represents a submatrix block or a subvector. The submatrix $\mathbf{T}_{I_A J_B}$ and $\mathbf{G}_{I_A J_B}$ are related with the traction and displacement Green's functions, respectively, where I and J can be M (number of elements in the free surface of the half-space E), L (number of elements at the shared interface between the half-space E and inclusion R), or K (number of elements in the free surface of the inclusion R), and in which A and B refer to the domains E or R. The subvectors $\mathbf{t}_{I_A}$ and $\mathbf{u}_{I_A}$ are the tractions and displacements due to the free field, that is, those produced by the wave field in the absence of any irregularity, which includes incident and reflected waves by the half-space free surface. The blocks $\mathbf{0}_{M_E L_R}$, $\mathbf{0}_{M_E K_R}$, $\mathbf{0}_{K_R M_E}$, and $\mathbf{0}_{K_R L_E}$ are zero blocks, and subvectors $\mathbf{0}_{M_E}$ and $\mathbf{0}_{K_R}$ are zero vectors. It is easy to see that when applying the matrix static condensation approach, the linear system of equations displayed previously becomes several small linear systems of equations that can be solved using less memory than the original system. By taking out the zero blocks from the computations, the final solution spends a minor time but preserves the same accuracy as the formulation applied by Sánchez-Sesma and Luzón (1995). The static condensation approach is based on an implicit factorization of the coefficient matrix by taking advantage of the location of the zero blocks near the upper right and lower-left corners of the system. Considering the first and fourth block rows of the system, we can write

$$[\mathbf{T}_{M_E M_E}][\mathbf{P}_1] = [\mathbf{T}_{M_E L_E}] \quad (2)$$

$$[\mathbf{T}_{K_R K_R}][\mathbf{P}_2] = [\mathbf{T}_{K_R L_R}] \quad (3)$$

where $[\mathbf{P}_1]$ and $[\mathbf{P}_2]$ are unknown intermediate matrices that can be solved as a set of simultaneous equations. Then,

$$\begin{aligned} [\mathbf{Q}_{11}] &= [\mathbf{T}_{L_E L_E}] - [\mathbf{P}_1][\mathbf{T}_{L_E M_E}] \\ [\mathbf{Q}_{12}] &= [\mathbf{T}_{L_E L_R}] - [\mathbf{P}_2][\mathbf{T}_{L_E K_R}] \\ [\mathbf{Q}_{21}] &= [\mathbf{G}_{L_R L_E}] - [\mathbf{P}_1][\mathbf{G}_{L_R M_E}] \\ [\mathbf{Q}_{22}] &= [\mathbf{G}_{L_R L_R}] - [\mathbf{P}_2][\mathbf{G}_{L_R K_R}] \end{aligned} \quad (4)$$

where $[\mathbf{Q}_{11}]$, $[\mathbf{Q}_{12}]$, $[\mathbf{Q}_{21}]$, and $[\mathbf{Q}_{22}]$ are intermediate matrices that can be easily computed and yield a new compact system of linear equations at one fourth the size of the original system, which can be expressed as follows:

$$\begin{bmatrix} \mathbf{Q}_{11} & \mathbf{Q}_{12} \\ \mathbf{Q}_{21} & \mathbf{Q}_{22} \end{bmatrix} \begin{Bmatrix} \varphi_{L_E} \\ \varphi_{L_R} \end{Bmatrix} = \begin{Bmatrix} -\mathbf{t}_{L_E} \\ -\mathbf{u}_{L_R} \end{Bmatrix} \quad (5)$$

After solving this system, φ_{L_E} and φ_{L_R} are known force density vectors. So, the final step in the algorithm consists in the computation of the only unknown force density vectors, φ_{M_E} and φ_{K_R}, as follows:

$$\begin{aligned} \{\varphi_{M_E}\} &= -[\mathbf{P}_1]\{\varphi_{L_E}\} \\ \{\varphi_{K_R}\} &= -[\mathbf{P}_2]\{\varphi_{L_R}\} \end{aligned} \quad (6)$$

In contrast to the threshold-biconjugate gradient approach by Ortiz-Alemán *et al.* (1998) that works well for a relatively low frequency, our scheme has no implicit truncation errors, and thus, it is stable at higher frequencies for both alluvial valleys and topographies. The computations are done in a very efficient computer program in FORTRAN 90 with dynamic memory that does not waste any extra resources. In this way, it is possible to compute, in the same computer and with the same 3D problem, the solution corresponding to approximately twice the frequency calculated with the classic form using the full matrix in the IBEM.

Moreover, we dynamically discretized all surfaces in the model. To do this, we computed a discrete grid for every frequency analyzed, in such a way that we always have at least 4.5 boundary elements per wavelength of S waves in each region. For the irregular surfaces, we constructed a grid formed by rectangular elements that cover the complete surface. After this, each planar rectangular element of the grid is assumed to be a circle with the same surface as that of the rectangular element. On the other hand, in the flat boundaries, that is, in the free surfaces of the half-space and the basin, the elements are distributed with constant distances from the origin of our local coordinate system, forming different adjacent rings. The total surface of a ring is equal to the sum of the surfaces of all of the elements of the ring. The flat free surface of the bedrock was discretized up to a radial distance of 55 km from the origin of our coordinate system, which is located at the common point that is shared by both profiles A–B and A′–B′, in the centre of the basin. In Fig. 2, an example of the distribution of boundary elements of the basement can be seen for a frequency of 0.149 Hz.

Results

We used the IBEM in the frequency domain, and we have computed the basin's response for 77 frequencies from 0 up to 0.312 Hz, for incident P, SV, and SH plane waves propagating from the south. The frequency of 0 Hz corresponds to the case where no inclusion exists, that is, the solution of the half-space.

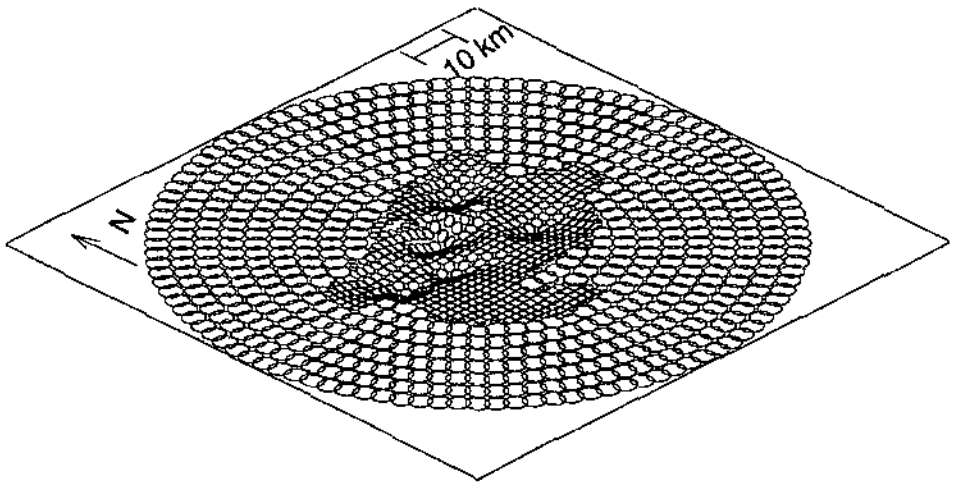

Figure 2. Example of discretization of the sediment–basement boundary for the frequency of 0.149 Hz.

The first results that we present show the influence of the deep structure of the Granada Basin on the amplification patterns for incident *SH* plane waves at various frequencies. We have selected incident angles of 0° and 60° with respect to the vertical. These results can be seen in Fig. 3 and 4, respectively, for the E–W (transverse motion), N–S (radial motion), and vertical components of displacement. For the sake of comparison, in both figures the amplification patterns are displayed at the same frequencies (0.149, 0.198, 0.248, and 0.312 Hz). We can clearly observe in both figures, even for relatively low frequencies, the amplifications produced by the deep structure of the Granada Basin. In fact, for the E–W component, the basin produces large amplifications for the chosen frequencies. In particular, for a vertical incidence (Fig. 3), the amplification reaches to nearly 10 times the amplitude of the incident source wave, in the frequency of 0.312 Hz, at various basin locations. For the same component of displacement outside the basin, the amplitude of the observed motion is about two times the incident one, as expected. For N–S and vertical motions, the amplification pattern is very interesting. Generally speaking, the maximum levels of the displacement are produced at those places where the depths of the basin are greater, that is to say, at the known depocenters. On the other hand, these maximum levels increase with frequency for both incidences, 0° and 60°. For both vertical incidence and the N–S component, the displacement amplitudes reach values larger than 5.

These effects, which cannot be obtained using 1D or 2D numerical modeling, correspond to the 3D nature of the deep basement of the Granada Basin. Fig. 5 shows the comparison of the 1D and 3D response for vertically incident *SH* waves at various receivers across the basin. The 1D solution corresponds to the model of a single layer over a half-space, with the same thickness as that of the depth of the basement at each station. The selected stations (5, 7, and 10) on profile A–B are next to the depocenters, with basement depths of 2295 m, 1908 m, and 1744 m, respectively. The 3D response of the Granada Basin is more complex than the 1D, even at low frequency, as can be observed in Fig. 5. In the transverse displacement, the amplitude levels of the 1D and 3D responses at receivers 7 and 10 are quite similar, but on the other hand, the resonant frequency in the complete 3D solution at station 7 is slightly shifted to 0.2338 Hz. At station 5, the response is different in both the amplification level and the frequency content. In fact, the 1D solution predicts an amplification of 4.91 at a frequency of 0.1743 Hz, whereas the complete 3D response has an amplitude near 7 at 0.2480 Hz.

For the radial and vertical components, the response is completely different. Whereas the amplitudes in the 1D models are equal to zero in all cases, for the 3D case, these displacements are comparable to the amplitude of the incident wave only at lower frequencies. Moreover, in the radial motion at station 10, the 3D amplification is two times the incident one at frequencies near 0.3 Hz.

Analysis of Wave Propagation

In this section, we compute the seismic response in the time domain by using an incident Ricker wavelet (Ricker, 1977). In our computations, we used a characteristic period of $t_p = 6.5$ sec and a time lag of $t_s = 40$ sec. This pulse represents the input motion, which has a waveform that runs from $\mathbf{u}_{\min} = -0.4432$ to $\mathbf{u}_{\max} = 1$ displacement unit, as shown in Fig. 6. With the aim of studying the main characteristics of elastic wave propagation within our Granada Basin model, we use *P*- and *SV*-plane waves coming from the south, with an incident angle of 30° relative to the vertical.

In the case of the incident *P*-wave source, we computed the time response from the various frequencies studied by using Fourier synthesis. Approximately 18 sec of the radial (N–S) displacements are depicted in Fig. 7 by means of

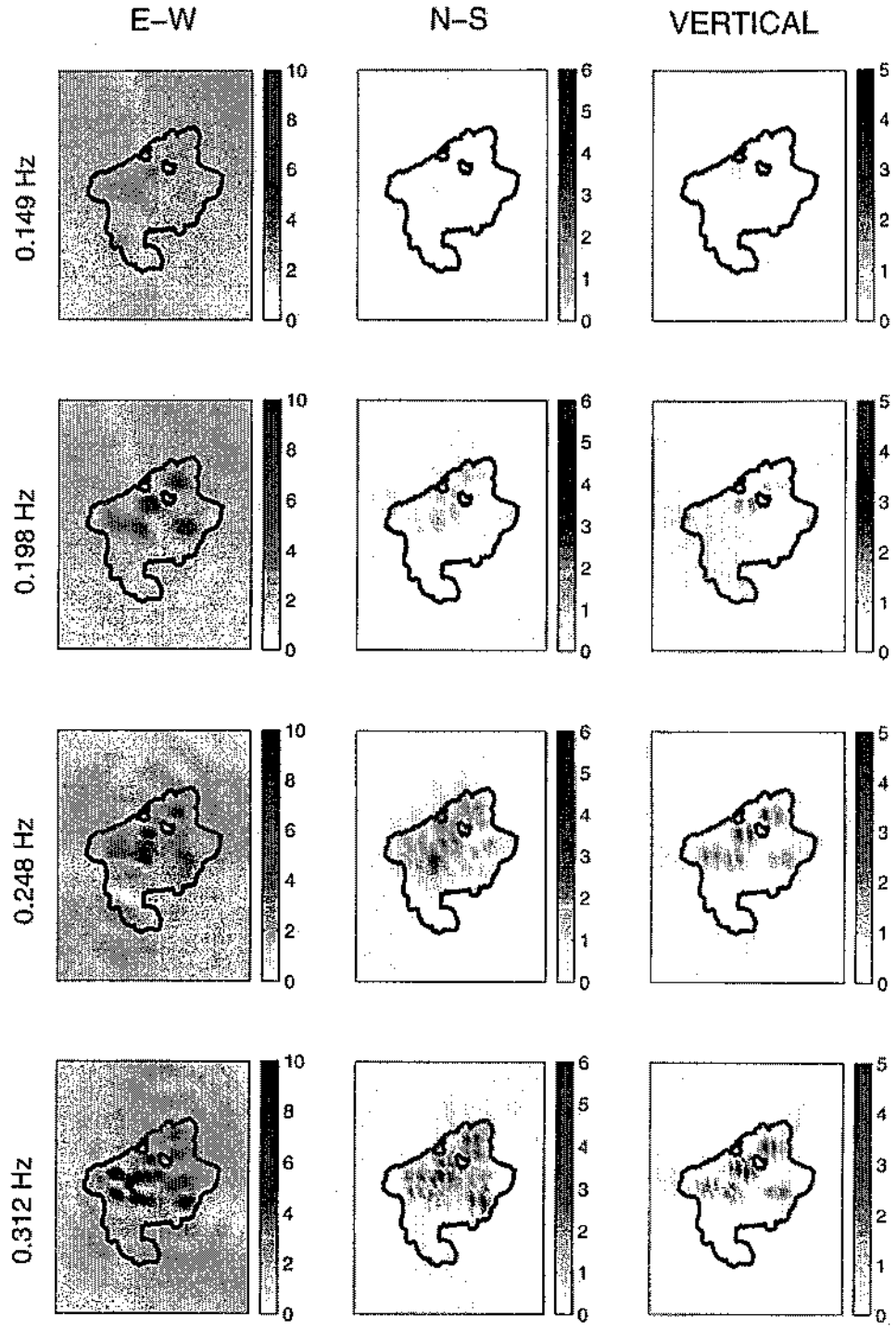

Figure 3. Amplifications, relative to the amplitude of the incident wave, of the three components of displacement at various frequencies in the Granada Basin for an *SH* wave coming from the south and with vertical incidence. The zero-depth contour of the basin is shown for reference.

snapshots at different times. Note that displacements observed at the free surface for this component are in the range from -1.8 to 2 displacement units, as shown on the scale bar, whereas the incident motion produced by the Ricker pulse in the N–S component ranges from $\mathbf{u}_{\min}(\text{N–S}) = \sin 30 \cdot \mathbf{u}_{\min} = -0.2216$ to $\mathbf{u}_{\max}$ (N–S) $= \sin 30 \cdot \mathbf{u}_{\max} = 0.5$ displacement units, that is, in some times and positions, the amplification produced is ~8. The *P* wave arrives after 36.8826 sec in the shallower part of basin to the south. These first displacements, represented with negative (dark shades)

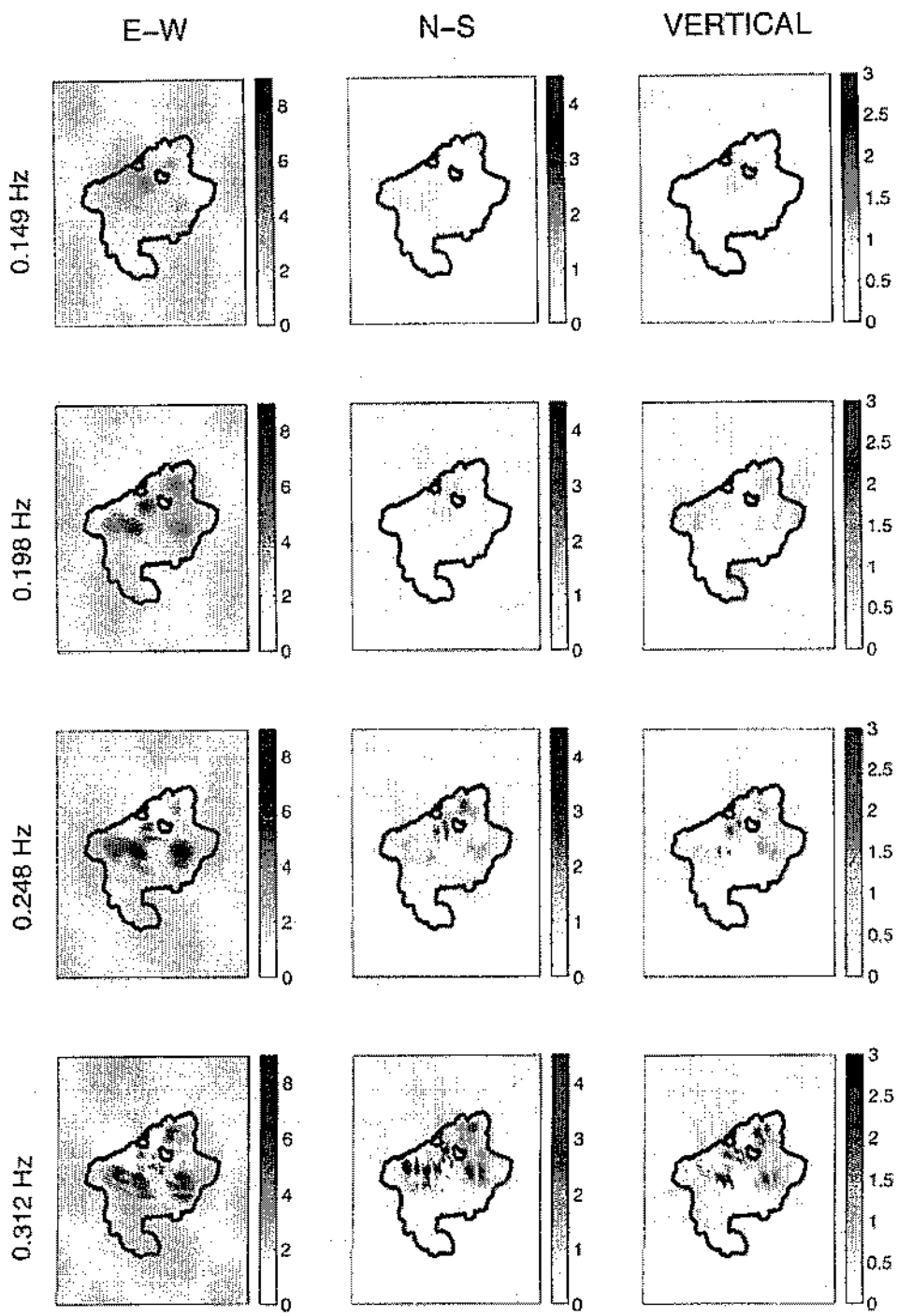

Figure 4. Same as Fig. 3, but for an *SH* wave coming from the south and with an incident angle of 60° with respect to the vertical.

amplitudes inside and outside the sediments, do not produce any remarkable effects. Nevertheless, after a time of 40.0898 sec, the direct wave begins to be amplified, as can be seen at this time (dark shades inside the basin) and in the following snapshot (light shades inside the basin). While the incident wave is traveling through the basin, the strongest ground motion is found at sites where the basin is deeper. This effect is more prominent for the radial component than for the vertical one (not shown). After the direct wave departs from the northern part of the model ($t = 46.5041$ sec), the mechanical energy that remains trapped inside the basin continues producing displacements at the free surface. As before, the major displacements for $t > 46.5041$ sec are observed again at the locations above the deepest parts of the

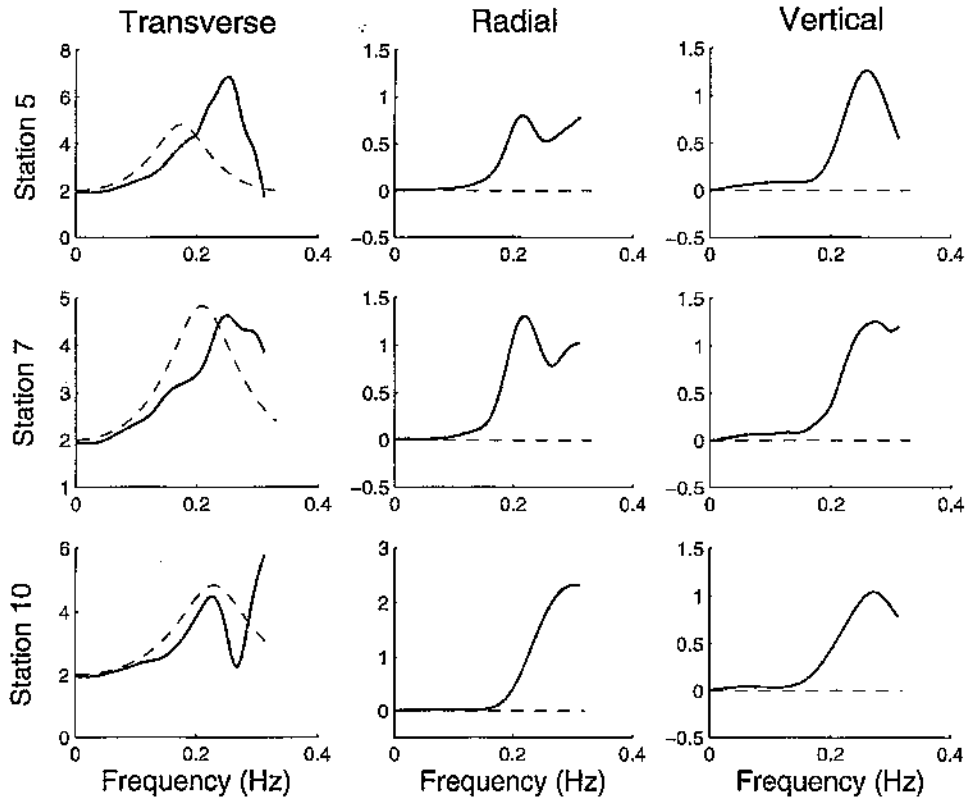

Figure 5. 1D (dashed line) and 3D (solid line) seismic responses for vertically incident *SH* waves at stations 5, 7, and 10 of the profile A–B shown in Fig. 1.

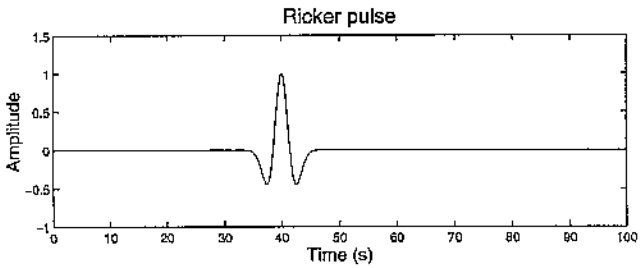

Figure 6. Incident Ricker pulse used in our study. The characteristic period is of $t_p = 6.5$ sec and the time lag, of $t_s = 40$ sec.

basin and are more significant on the N–S component presented in Fig. 7.

Results for the radial displacements produced by an incident *SV*-wave source are shown in Fig. 8. The snapshots are given for the same times used for the *P*-wave simulation. For this incident wave, the displacements observed at the free surface for the N–S component are in the range of -1.8 to 2.4 displacement units, whereas the incident motion in the N–S component ranges from $\mathbf{u}_{\min}(\text{N–S}) = \cos 30 \cdot \mathbf{u}_{\min} = -0.3838$ to $\mathbf{u}_{\max}(\text{N–S}) = \cos 30 \cdot \mathbf{u}_{\max} = 0.8660$ displacement units. The motion begins to be amplified inside the basin after 40.0898 sec, and the amplification is more important in the following times when the direct wave crosses our model of the Granada Basin. This has been observed in both radial and vertical components. After this, the energy is trapped inside the structure, producing displacements that can be observed from $t = 46.5041$ sec and subsequent times, when the direct wave exits from the northern part of the basin.

A small quantity of energy is generated at the edges of the basin. This cannot be well observed in the snapshots of Fig. 8, because the amplitudes of these displacements are low in comparison with the motion produced by the incident wave field. This small quantity of energy can be better observed in Fig. 9, where we present the synthetic seismograms of vertical (V), radial (R), and tangential (T) components of displacement at the receivers along the profiles A–B and A′–B′ of Fig. 1. The ground motion inside the sedimentary basin is generally more complex than observed in hard rock, as shown on the tangential component of both profiles where no direct wave exists. Comparing this component on both profiles, we see that the one corresponding to the profile A–B presents a more complicated pattern than the displacement of profile A′–B′. This is probably because profile A–B crosses various depocenters of the Granada Basin, whereas profile A′–B′ crosses only one. Note also that there are more stations inside the basin on profile A–B. Nevertheless, the characteristics of the propagating phases within the basin, which can be seen on the tangential components, are differ-

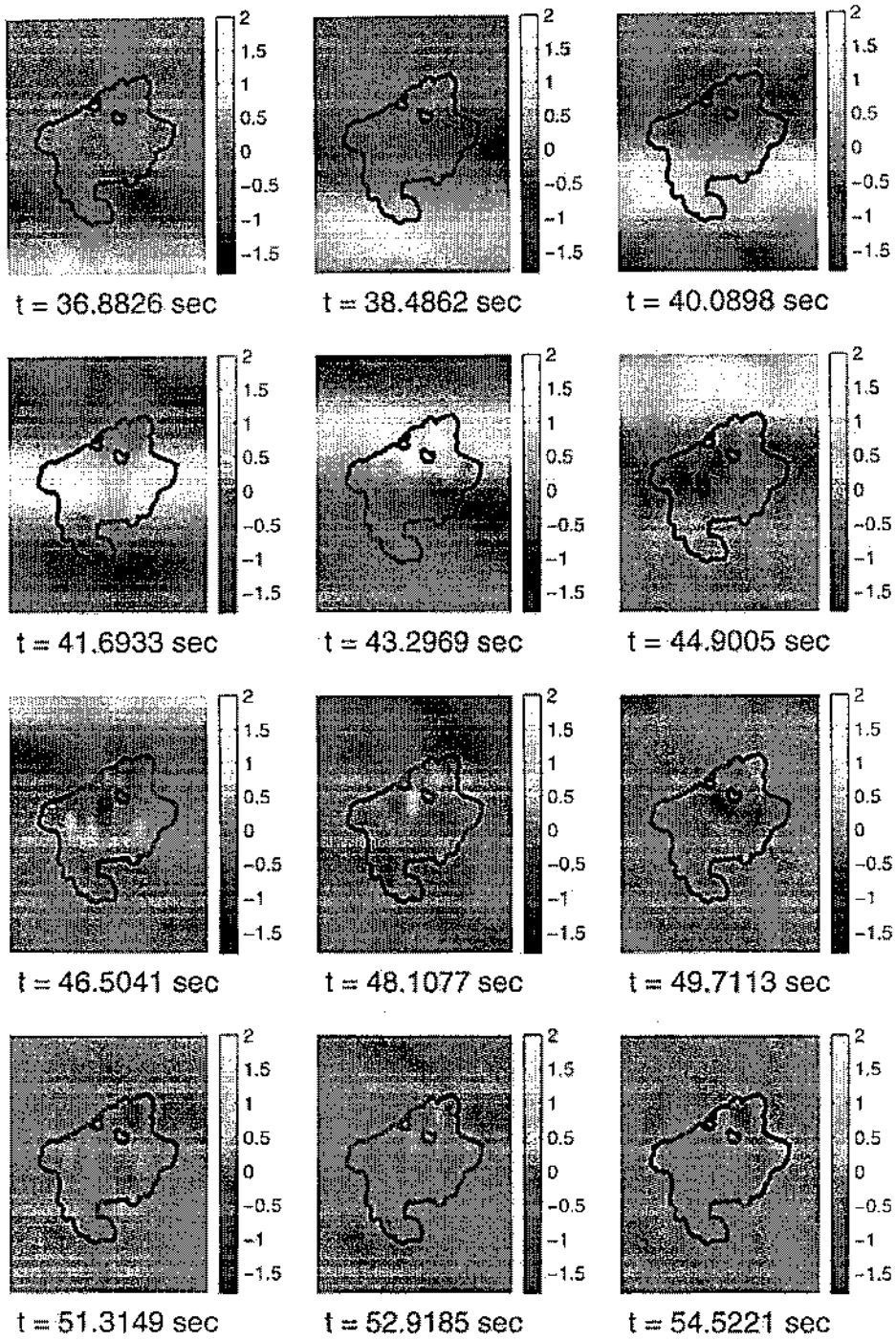

Figure 7. Radial (N–S) displacement snapshots of wave propagation in the Granada Basin for a simulation with a *P* wave propagating from the south and with an incident angle of 30° with respect to the vertical. Light (dark) shading depicts positive (negative) particle displacement. The zero-depth contour of the basin is shown for reference.

ent. Whereas on A–B the propagation of a phase identified as a Rayleigh wave is observed, the corresponding wave that travels on A′–B′ can be identified as a Love wave. On the other hand, the emission of waves radiated outside the Granada Basin is observed as well on the vertical and radial components of the A′–B′ profile. These waves propagate with more energy on the forward direction (from south to north) of the incident body wave. These can be identified as Rayleigh waves by means of the results given in Fig. 10, where we present the polarigrams in the radial–vertical plane for the incidence *SV* waves at the 15 receivers on profile A′–B′. These polarigrams display the variation in the displace-

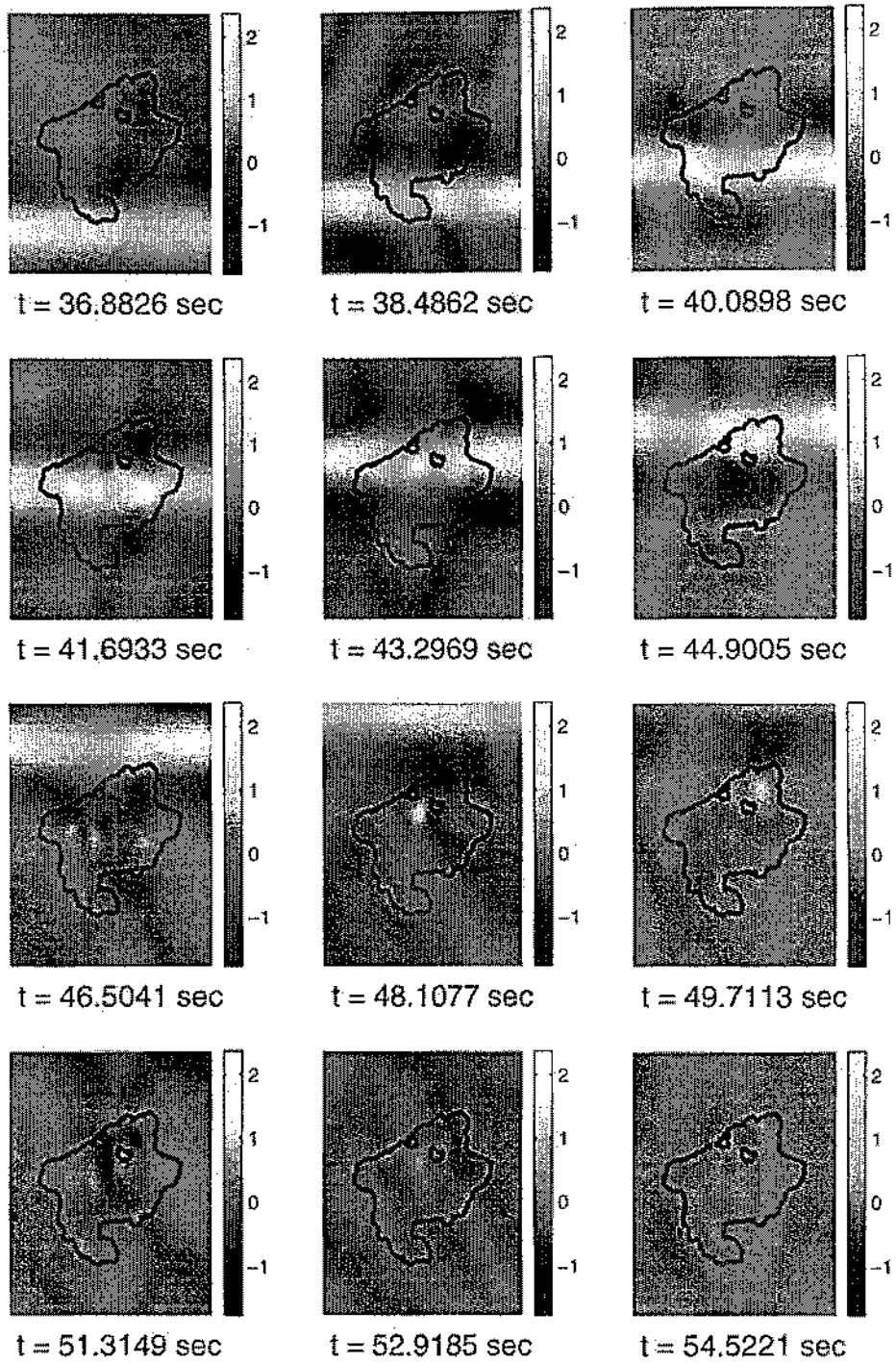

Figure 8. Same as Fig. 6, but for an incident *SV* wave.

ment vectors with time. The Rayleigh waves, showing little energy, can be identified in the later arrivals, with their characteristic elliptical and retrogade motion. This is the case not only for a half-space but also for the fundamental Rayleigh mode in a layer as well.

Part of the effects observed in the Granada Basin are consistent with those obtained by Olsen *et al.* (1995), who simulated the 3D wave propagation in the Salt Lake Basin (Utah), and other aspects of our computations are similar to the results of Frankel (1993) from 3D finite-difference modeling of the San Bernardino valley (California). Whereas in the Salt Lake Basin the resonating energy is radiated into the bedrock surrounding the sediments without generating any well-developed, coherent surface waves or trapped body-wave phases in the basin, in the San Bernardino model, clear, large-amplitude surface waves were generated at the

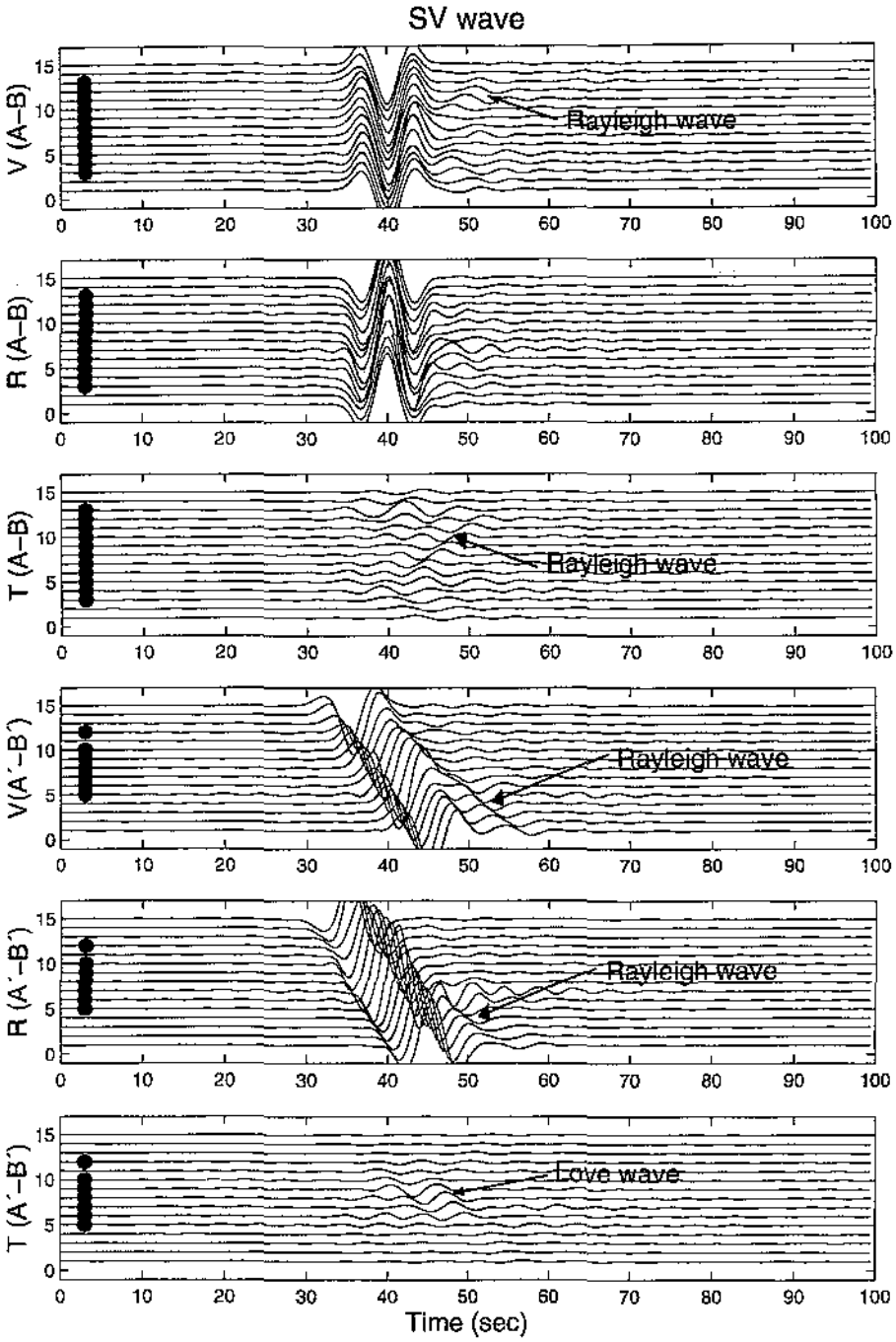

Figure 9. Seismograms of the vertical (V), radial (R), and tangential (T) components of displacement at the 15 receivers of the A′–B′ profile and the 15 receivers of the A–B profile. The seismograms that have a solid circle are located inside the Granada Basin.

edges of the basin. The Granada Basin has an average behavior between these two models. In our computations, part of the energy observed after the incident wave, in the synthetic seismograms of the profiles A–B and A′–B′, is not well developed, and although surface waves have been detected inside and outside the Granada Basin, these waves do not propagate with large amplitudes, as has occurred in the San Bernardino valley. This average behavior can be explained by various similitudes and differences among the three models: (1) The low-impedance contrast between the sediments and the bedrock in the Granada Basin (equal to 2.45) produces similar effects to those in the Salt Lake Basin (with impedance contrast equal to 2.69). In contrast, the impedance contrast in the San Bernardino Basin is higher (equal to 4.3). The effects produced by the impedance contrast are well known and have been defined. As has been

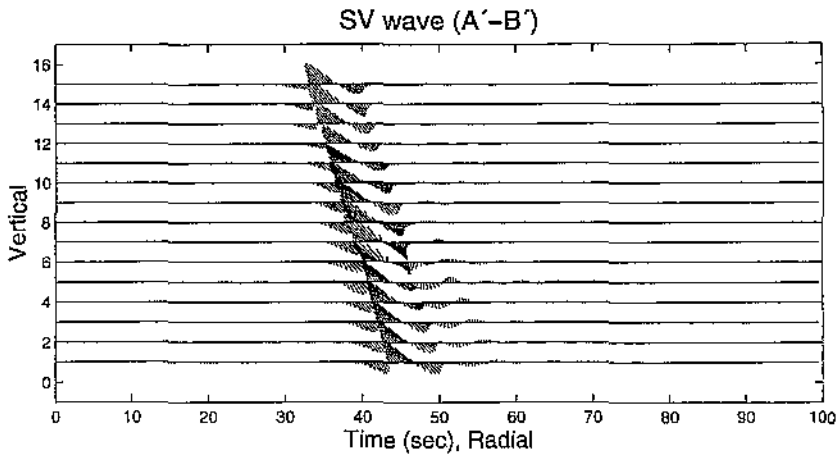

Figure 10. Polarigrams in the radial–vertical plane for the incidence of *SV* waves at the 15 receivers of the A′–B′ profile.

pointed out by previous authors (see e.g., Bard and Bouchon, 1980; Sánchez-Sesma *et al.*, 1993), when high-impedance contrast exists, surface waves are very efficiently generated and reflected at the edges of the basin. (2) As was showed by Hill *et al.* (1990), energetic surface waves can be generated at steeper basin slopes as well. The Granada Basin has many zones where the slope of the basement is ~30%, in particular the northern part, in which this type of wave can be generated. This is similar to the San Bernardino Basin, where exist slopes ~30% near the southern part of the San Jacinto fault. In contrast, the model of the Salt Lake Basin, which does not produce well-developed coherent surface waves, has slopes of ~10%. (3) The incident wave field of the Granada Basin (plane waves) considered in this work is similar to that of Olsen *et al.* (1995), who used *P*-plane waves in the Salt Lake Basin. Conversely, Frankel (1993) used a kinematic time- and space-varying source function simulating an *M* 6.5 earthquake occurring on the edge of the basin. This author observed that the largest velocities in the San Bernardino Basin were dependent on the direction of rupture propagation of the seismic source and that maximum shaking was also dependent on asperity positions and radiation pattern.

Conclusions

We have computed the seismic response of the 3D basement structure of a model of the Granada Basin by using the IBEM for incident *P*-and *S*-plane waves. In this study, we have solved the linear system of equations by using a partition matrix method, which is different from the classic LU decomposition that has been used in previous articles. The advantage of the partition matrix method used here is that it is possible to calculate, on the same computer and with the same model configuration, the solution corresponding to approximately twice the frequency computed with the classic LU.

We have analyzed the results in both frequency and time domains, and for the range of frequencies that we have been able to compute, it has been observed that the most relevant site effects are due to the local amplifications produced inside the sediments. For *SH* waves, the amplification factor reaches values near 10 times the amplitude of the incident wave for some specific frequencies and locations. In the other case, for the characteristic period considered in this work for the incident *P*-wave Ricker pulse, the amplification arrives at some specific times and positions around 8. In general, for the incident plane waves considered in this work, the amplification levels are not too large, because the impedance contrast between the sediments and the bedrock (equal to 2.45) is relatively low.

The geometry of the basin contributes in a deterministic way to the response. Where basement depths are >3 km, we see a characteristic seismic response in the range of frequencies dealt with in this study that cannot be predicted using a 1D model. The amplification patterns of the displacement observed for incident *P*, *SV*, and *SH* waves have maximum levels at those locations where the depths of the basin are larger. Moreover, according to our model, the Granada Basin is likely to produce and emit surface waves with little energy, as we observed in the synthetic seismograms and their corresponding polarigrams. These waves in this basin do not cause large displacements. The generation of these surface waves is a common feature that has been observed in many basins around the world by using real records and that have been reproduced using numerical methods for modeling of the seismic response of similar geological structures (see, e.g., Hatayama and Fujiwara, 1998).

One of the more important conclusions that we can obtain from this work is that a simple 3D model allows us to point out important site effects that may influence the seismic motion at future earthquakes in the Granada Basin between 0 and 0.312 Hz. Therefore, it is necessary to allocate resources and effort in three directions: (1) setting an adequate accelerograph array to cover the basin in an efficient way, particularly in those places where we have observed the major amplifications in this study; (2) the development of specific and controlled experiments to improve the basin's model to obtain the complete geometry and physical properties of the different sediments that fill the basin; and

(3) the consideration of more realistic aspects into numerical modeling, such as the sedimentary layering, to obtain the seismic response of the Granada Basin for higher frequencies, or the use of nearby sources, which can change the response because of the direction of rupture propagation or the radiation pattern, as was shown by Frankel (1993) in the San Bernardino Basin. With the IBEM and the appropriate Green's functions, it is possible to take into account a layered structure or a medium with a velocity gradient, as was done by Luzón *et al.* (unpublished results, 2001) in 2D alluvial basins with a vertical gradient of velocity. On the other hand, the inclusion of near sources can be performed by constructing the kinematic model of a finite fault with a set of point sources with their appropriate rupture velocity. Each of these point sources can be constructed with the corresponding Green's functions, as was done by Luzón *et al.* (1999), who computed the displacements produced by near seismic point sources to 3D mountains with the IBEM. All of this could provide us with good estimations of seismic motion with which to compare the records of ground acceleration, with the aim of understanding the complex seismic response of the Granada Basin.

Acknowledgments

We thank W. J. Stephenson and T. Kagawa for their helpful suggestions and reviews of the manuscript. Thanks are given to Z. al Yuncha for his help in the digitization of part of the Granada Basin. This work was performed during the visit of S. A. Gil-Zepeda to the University of Almería, Spain. Part of the computations were done with the computers of the DMPN Institute de Physique du Globe de Paris, France; the kindness of Prof. Jean-Pierre Vilotte is greatly appreciated. This work was partially supported by CICYT, Spain, under Grants AMB99-1015-CO2-02 and AMB99-0795-CO2-01; by DGAPA-UNAM, Mexico, under Project IN104998; and by the research teams RNM-194 and RNM-103 of Junta de Andalucía, Spain.

References

Aki, K. (1988). Local site effects on strong ground motion, in *Earthquake Engineering and Soil Dynamics II—Recent Advances in Ground Motion Evaluation*, J. Lawrence Von Thun (editor), American Society of Civil Engineering, New York, 103–155.

Bard, P.-Y., and M. Bouchon (1980). The seismic response of sediment-filled valleys, part 1: the case of incident *SH* waves, *Bull. Seism. Soc. Am.* **70,** 4, 1263–1286.

Canas, J. A., F. De Miguel, F. Vidal, and G. Alguacil (1988). Anelastic Rayleigh wave attenuation in the Iberian Peninsula, *Geophys. J. Int.* **95,** 391–396.

De Miguel, F., F. Vidal, G. Alguacil, and J. M. Guirao (1989). Spatial and energetics trends of the microearthquakes activity in the central Betics, *Geodin Acta*, **3,** 87–94.

Frankel, A. (1993). Three-dimensional simulations of ground motions in the San Bernardino Valley, California, for hypothetical earthquakes on the San Andreas fault, *Bull. Seism. Soc. Am.* **83,** 1020–1041.

Frankel, A., and W. Stephenson (2000). Three-dimensional simulations of ground motions in the Seattle region for earthquakes in the Seattle fault zone, *Bull. Seism. Soc. Am.* **90,** 1251–1262.

García Dueñas, V., and J. C. Balanyá (1986). Estructura y naturaleza del arco de Gibraltar. *Maleo-Bol. Inf. Soc. Geol.* **2,** 23 (in Spanish).

Hatayama, K., and H. Fujiwara (1998). Excitation of secondary Love and Rayleigh waves in a three-dimensional sedimentary basin evaluated by the direct boundary element method with normal modes, *Geophys. J. Int.* **133,** 260–278.

Hill, J., H. Benz, M. Murphy, and G. T. Schuster (1990). Propagation and resonance of *SH* waves in the Salt Lake Valley, Utah. *Bull. Seism. Soc. Am.* **80,** 23–42.

Horike, M. (1985). Inversion of phase velocity of long-period microtremors to the *S*-wave-velocity structure sown to the basement in urbanized areas, *J. Phys. Earth* **33,** 59–96.

Ibáñez, J., J. Morales, F. De Miguel, F. Vidal, G. Alguacil, and A. Posadas (1991). Effect of a sedimentary basin on estimations of Q_c and Q_{Lg}, *Phys. Earth Planet. Interiors* **66,** 244–252.

Kagawa, T., and Group for Spanish-Japanese joint work on microzonation of Granada basin (1996). Microtremor array observation in the Granada basin, southern Spain, in *Homenaje en Honor del Profesor Fernando de Miguel Martínez*. F. Vidal, M. Espinary J. A. Esquivel (Editors), Universidad de Granada, Granada, Spain, 287–304 (in Spanish).

Luzón, F., F. J. Sánchez-Sesma, J. L. Rodríguez-Zúñiga, A. M. Posadas, J. M. García, J. Martín, M. D. Romacho, and M. Navarro (1997). Diffraction of P, S and Rayleigh waves by three-dimensional topographies, *Geophys. J. Int.* **129,** 571–578.

Luzón, F., F. J. Sánchez-Sesma, A. Gil, A. Posadas, and M. Navarro (1999). Seismic response of 3D topographical irregularities under incoming elastic waves from point sources, *Phys. Chem. Earth (A)*, **24,** 231–234.

Morales, J. (1991). Caracterización de la respuesta sísmica local en las cuencas de Granada (España) y Ciudad Guzmán (México) mediante el análisis espectral de microterremotos y terremotos. *Ph.D. Thesis.* University of Granada, Spain, 276 Pp (in Spanish).

Morales, J., F. Vidal, F. De Miguel, G. Alguacil, A. Posadas, J. Ibáñez, J. M. Guzmán, and J. M. Guirao (1990). Basement structure of the Granada basin, Betic Cordilleras, southern Spain, *Tectonophysics* **177,** 337–348.

Morales, J., K. Seo, T. Samano, J. A. Peña, J. Ibáñez, and F. Vidal (1993). Site response on seismic motion in the Granada basin (southern Spain) based on microtremor measurement, *J. Phys. Earth* **41,** 221–238.

Morales, J., S. K. Singh, and M. Ordaz (1996). Analysis of Granada, Spain earthquake of 24 June, 1984 ($M = 5$) with emphasis on seismic hazard in the Granada basin, *Tectonophysics* **257,** 253–263.

Norma de Construcción Sismorresistente NCSE-94, (1995). Boletín Oficial del Estado, February 8. Ministerio Obras Públicas, Transportes y Medio Ambiente, 3935–3980 (in Spanish).

Olsen, K. B. (2000). Site amplification in the Los Angeles basin from three-dimensional modeling of ground motion. *Bull. Seism. Soc. Am.* **90,** 6B, S77–S94.

Olsen, K. B., and R. J. Archuleta (1996). Three-dimensional simulation of earthquakes on the Los Angeles fault system. *Bull. Seism. Soc. Am.* **86,** 575–596.

Olsen, K. B., J. C. Pechmann, and G. T. Schuster (1995). Simulation of 3D elastic wave propagation in the Salt Lake basin. *Bull. Seism. Soc. Am.* **85,** 1688–1710.

Ortiz-Alemán, C., F. J. Sánchez-Sesma, J. L. Rodríguez-Zúñiga, and F. Luzón (1998). Computing topographical 3D site effects using a fast IBEM/conjugate gradient approach, *Bull. Seism. Soc. Am.* **88,** 393–399.

Press, W. H., S. A. Teukolsky, W. T. Vetterling, and B. P. Flannery (1992). *Numerical Recipes in Fortran*, Cambridge University Press.

Reicherter, K. R. (2001). Paleoseismologic advances in the Granada basin (Betic cordilleras, southern Spain). *Acta Geol. Hisp.* **36,** 278–281.

Ricker, N. H. (1977). *Transient Waves in Visco-Elastic Media*, Elsevier, Amsterdam, Holland.

Rodríguez Fernández, C., C. Sanz de Galdeano, and J. Fernández (1989). Genesis and evolution of the Granada Basin (Betic Cordillera, Spain). *International Symposium on Intermontane Basins, Geology & Resources*, Chiang Mai, Thailand, 294–305.

Sánchez-Sesma, F. J. (1996). Strong ground motion and site effects, in *Computer Analysis of Earthquake Resistant Structures*, D. E. Beskos

and S. A. Anagnostopoulos (editors), Comp. Mech. Publications, Southampton, 200–229.

Sánchez-Sesma, F. J., and F. Luzón (1995). Seismic response of three dimensional alluvial valleys for incident *P*, *S* and Rayleigh waves, *Bull. Seism. Soc. Am.* **85,** 269–284.

Sánchez-Sesma, F. J., J. Ramos-Martínez, and M. Campillo (1993). An indirect boundary element method applied to simulate the seismic response of alluvial valleys for incident P, S and Rayleigh Waves, *Earthquake Eng. Struct. Dyn.* **422,** 279–295.

Sanz de Galdeano, C., and J. A. Vera (1992). Stratigraphic record and paleogeographical context of the Neogene basins in the Betic Cordillera, Spain, *Basin Res.* **4,** 21–36.

Vidal, F. (1986). Sismotectónica de la región Béticas-Mar de Alborán, *Ph.D. Thesis*, University of Granada, Spain, 450 Pp (in Spanish).

Departamento de Física Aplicada
Universidad de Almería
Cañada de San Urbano
s/n 04120 Almería, Spain
(F.L.)

Instituto Andaluz de Geofísica y Prevención de Desastres Sísmicos
Universidad de Granada
Campus Universitario de Cartuja
s/n 18071 Granada, Spain
(F.L., J.M.)

Instituto de Ingeniería, UNAM
Cd. Universitaria, Apdo. 70-472
Coyoacán
04510 México D.F., México
(S.A.G.-Z., J.A., F.J.S.-S.)

Instituto Mexicano del Petróleo
Eje Central 152
07730, México D.F., México
(C.O.-A)

Manuscript received 12 October 2001.

Apéndice B

Simulación tridimensional del movimiento del suelo en la cuenca de Zafarraya (Sur de España) 1.335 Hz., bajo la incidencia de ondas planas.

La Cuenca de Zafarraya es una de las cuencas de las montañas Béticas del sur de España, localizada en una de las regiones con el mayor nivel de movimiento sísmico en la Península Ibérica. En este trabajo se utiliza el Método Indirecto de Elementos en la Frontera (IBEM por sus siglas en inglés Indirect Boundary Elements Method), para calcular el movimiento tridimensional de la Cuenca de Zafarraya bajo la incidencia de ondad P y S. Se ha resuelto el sistema de ecuaciones lineales obtenidas en el IBEM utilizando el método de partición de matrices que ha sido más eficiente que el tradicional método LU, utilizado en trabajos previos. Los resultados muestran que los desplazamientos horizontales son amplificados tanto en amplitud como en duración en las componentes donde el movimiento directo existe (radial para ondas P, SV, y transversal para las ondas SH). En cualquier caso, los otros desplazamientos horizontales donde el movimiento directo no existe no son despresiables. Las amplificaciones más importantes son producidas en el sur de la Cuenca de Zafarraya donde hay dos importantes características: la primera es donde la profundidad de la cuenca es mayor, y la segunda, donde están cerca de las fronteras en el sur. Algunas de las ondas que han producido el incremento en la duración han sido interpretadas como ondas superficiales, las cuales en algunos casos provocan patrones característicos de polarización.

Geophys. J. Int. (2004) **156**, 584–594 doi: 10.1111/j.1365-246X.2004.02142.x

Three-dimensional simulation of ground motion in the Zafarraya Basin (Southern Spain) up to 1.335 Hz under incident plane waves

F. Luzón,[1,2] S. A. Gil-Zepeda,[3,4] F. J. Sánchez-Sesma[3] and C. Ortiz-Alemán[5]

[1] *Departamento de Física Aplicada, Universidad de Almería, Cañada de San Urbano s/n,* 04120 *Almería, Spain. E-mail: fluzon@ual.es*
[2] *Instituto Andaluz de Geofísica y Prevención de Desastres Sísmicos Universidad de Granada, Campus Universitario de Cartuja s/n,* 18071 *Granada, Spain*
[3] *Instituto de Ingeniería, UNAM; Cd. Universitaria, Apdo. 70-472, Coyoacán* 04510, *México D.F, Mexico*
[4] *Instituto Tecnológico de Tehuacán, Libramiento Instituto Tecnológico de Tehuacán s/n, Col. Santo Domingo, Tehuacán, Pue., C.P. 75770 A.P. 247, Mexico*
[5] *Instituto Mexicano del Petróleo, Eje Central* 152, 07730, *México D.F, Mexico*

Accepted 2003 September 30. Received 2003 June 25; in original form 2002 November 11

SUMMARY

The Zafarraya Basin is one of the intramountain Neogene basins of the Betic mountains (Southern Spain) located in one of the regions with the highest hazard level in the Iberian Peninsula. In this paper we use the indirect boundary element method (IBEM) to compute the 3-D ground motion of the Zafarraya Basin under incident *P* and *S* waves. We solve the linear system of equations obtained in the IBEM by using a partition matrix method that has been found more efficient than the classic $L \cdot U$ decomposition used in previous works. Our results show that the horizontal displacements are greatly amplified both in amplitude and duration in those components where direct motion exists (radial for *P* and *SV* waves, and transverse for *SH* waves). In any case, the other horizontal displacements where no direct motion exists are not negligible. The most important amplifications are produced at the south of the Zafarraya Basin, where two features characterize these sites: first the depth of the basin is the largest, and second, these locations are near the end of the basin where a very steep boundary exists. Some of the waves that have produced the increase in duration have been interpreted as surface waves, which in some cases provide characteristic polarization patterns.

Key words: boundary element method, inelastic waves, local seismic effects, numerical modelling, 3-D propagation, Zafarraya Basin.

INTRODUCTION

Throughout history, many of the earthquakes known as destructive have been influenced by site effects often combined with the effects of finite-extent sources. Some notable examples are: the Andalusian earthquake of 1884 near the Zafarraya Basin (Southern Spain); the San Francisco (USA) earthquakes in 1906 and 1957; those of Kanto, Tonankai, Niigata and Kobe (Japan) in 1923, 1944, 1964 and 1995, respectively; the earthquakes of 1957, 1975, 1985 and 1989 in Mexico; in Caracas (Venezuela) in 1967; and in Blackish Hill (USA) in 1989. These local effects can produce large spatial variations of seismic ground motion and structural damage when lateral irregularities of the soil exist, as is the case for sedimentary basins.

Once these kinds of seismic local effects were identified as the causes of great damage around the world, the International Association of Seismology and Physics of the Earth's Interior (IASPEI) and the International Association for Earthquake Engineering (IAEE) formed a Joint Working Group on the Effects of Surface Geology (ESG). This group proposed that a set of international 'blind' prediction experiments were the best way to assess the various methods used to predict local effects. The first experiment was performed using weak motion data recorded at Turkey Flat in California (USA). The second one was conducted using weak and strong motion data from the Ashigara Valley (Japan). The results of both experiments were presented in the International Symposium on the effects of surface geology on seismic motion held in Odawara (Japan) in 1992 (IASPEI–IAEE Joint Working Group on ESG 1992). The second, and actually last, ESG Symposium was celebrated in Yokohama (Japan) in 1998. In this Symposium, the recent studies taking in this topic since 1992 were summarized (IASPEI–IAEE Joint Working Group on ESG 1998). The meeting was also focused on comparing the prediction methods and the results through the simultaneous simulation of ground motion for the Kobe earthquake using common data distributed prior to the Symposium.

In order to obtain a good characterization and understanding of the seismic response of sedimentary basins, both experimental and numerical analyses have been used in last years. One recent paper dealing with observational studies concerning site effects is that of Chávez-García *et al.* (2002) using a high quality data set from a temporary digital seismograph network in a small alluvial basin in New Zealand. These authors observed locally generated surface waves

which propagated in stable directions inside this valley. Chávez-García *et al.* (2002) concluded as necessary the improvement of the knowledge of 3-D site effects, provided by the geometry of the basin, to incorporate them into the building codes. In other work, Rovelli *et al.* (2001) studied the seismograms recorded in a three-component array deployed in the Colfiorito Basin (Central Italy). They observed 1 s coherent wave trains which were interpreted as locally generated surface waves that were diffracted from the nearby basin edges, and proposed that the 3-D numerical modelling of wave propagation will help to understand the observations and to solve the uncertainties that still remain.

Several numerical techniques for the estimation of the seismic response in complex geological configurations have been recently developed. The flexibility and versatility of these techniques have increased following the improvement of the computational systems, and they altogether have allowed the use of 3-D geometries to model several sedimentary basins around the world: Olsen & Archuleta (1996) and Olsen (2000) used finite-differences to simulate ground motion in the Los Angeles Basin; Olsen *et al.* (1995) studied the propagation of *P* waves in the Salt Lake Basin; Frankel & Stephenson (2000) computed ground motions in the Seattle region with the finite-differences method; and Gil-Zepeda *et al.* (2002) used the indirect boundary element method (IBEM) to calculate the 3-D seismic response of the Granada Basin (Southern Spain).

In this work, we use the IBEM to simulate the propagation of seismic waves in a 3-D model of the Zafarraya Basin (Southern Spain) (see Fig. 1). This basin is located in one of the regions with the highest hazard level in the Iberian Peninsula as shown in the Spanish Seismic Building Code (Norma de Construcción Sismorresistente NCSE-94 1995). Available historical records indicate that in the

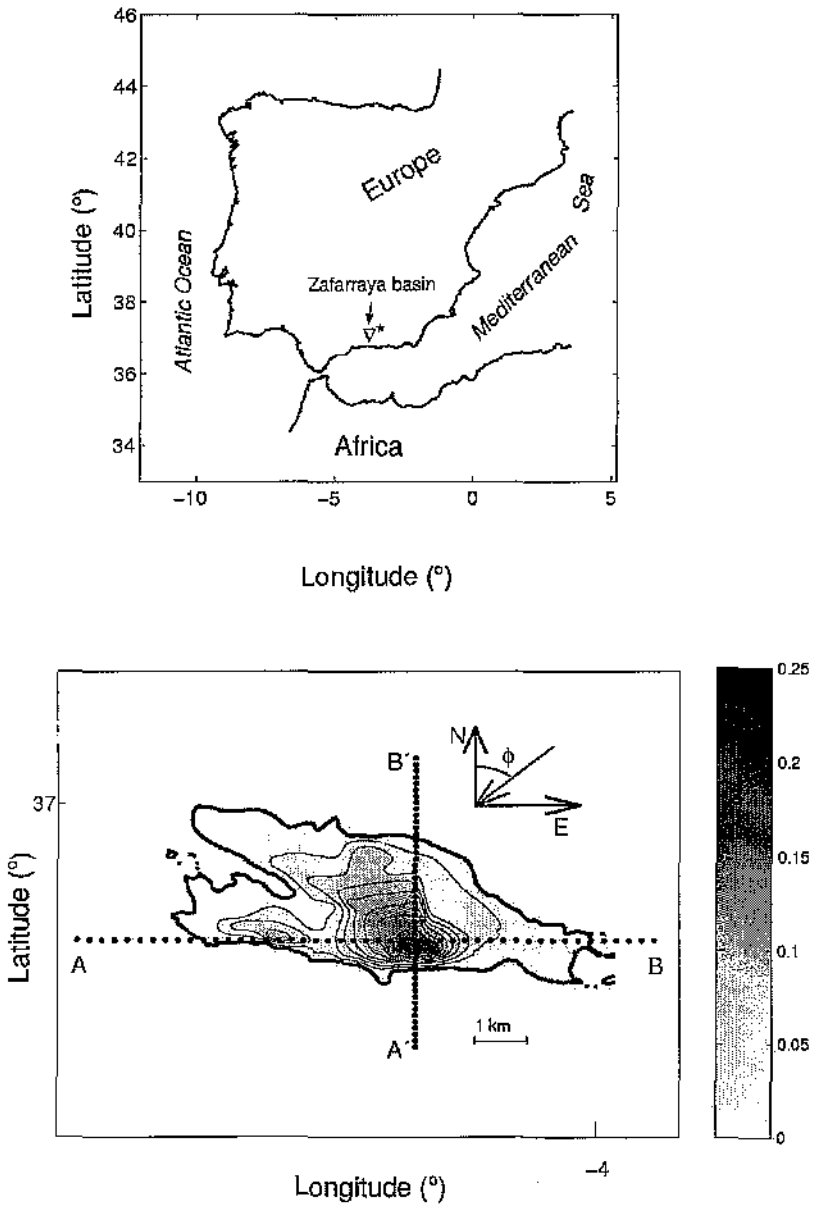

Figure 1. Top, map showing the location of the Zafarraya Basin. Bottom, depth of the basement of Zafarraya Basin with the locations of the receivers of the profiles A–B and A′–B′ on the planar free-surface. The contours have an interval of 25 m. The units of the depth scale bar are in km. The latitude and longitude are expressed in degrees. The incident waves have an azimuth equal to ϕ. The asterisk near of the Zafarraya Basin notes the location of the Andalusian earthquake of 1884 December 24.

last 2000 yr the south of the Iberian Peninsula has been affected by major earthquakes with MSK intensities from VII to X (Reicherter, 2001).

Large amplifications that can be attributed to site effects have been observed in the basin (Morales 1991). To analyse its response we study the amplification patterns and the peak-ground-motion calculated at the free planar surface of the model of the Zafarraya Basin. We use polarization patterns and two profiles (labelled as A–B and A′–B′ in Fig. 1) to illustrate part of the effects of the sedimentary basin.

THE ZAFARRAYA BASIN

The Zafarraya Basin is one of the intramountain Neogene basins of the Betic mountains, and is more precisely located at the most southern sub-Betic sector. The shape of this basin follows a general NW–SE trend as can be observed in Fig. 1. The geology and geological evolution of this sedimentary inclusion has been the subject of various works (see Morales *et al.* 1991, and references therein), and in particular, the 3-D basement geometry of the basin was defined by Morales (1991) by means of the interpretation of resistivity changes previously carried out by Chirlaque *et al.* (1987).

Southern Spain has the highest seismic hazard in the Iberian Peninsula, as shown in the maximum horizontal acceleration map for a return period of 500 yr (Norma de Construcción Sismorresistente NCSE-94 1995), with maximum values around 2.45 m s^{-2}. This seismic hazard is a consequence of the collision between the Euroasiatic and African plates on a regional scale. Most of the seismic energy is released by earthquakes with magnitude less than 5.0; however, catastrophic earthquakes occurred in the past. In fact, one of the most destructive earthquakes in Spain occurred on 1884 December 25 along the Ventas de Zafarraya Fault (VZF) located in the Central Betic Cordilleras. The normal VZF cuts the contact between the Alboran and the South Iberian domains in the Betic Cordilleras and the most important deformations and secondary features, such as landslides and liquefaction, are related to the activity of the VZF (Reicherter *et al.* 2002). This great earthquake, known as the 'Andalusian earthquake' was near Alhama de Granada, in the north–east of the Zafarraya Basin (see Fig. 1), and produced large damages throughout the region having an epicentral intensity of $I_0 = X$ (Vidal 1986). From the point of view of the seismic hazard, local effects have been studied by Morales *et al.* (1991) by means of a microtremors analysis. These authors showed that the dominant frequency of the basin was almost constant near 2.8 Hz (with small variations between 2.5 and 3.5 Hz), independently of the depth of the sediment at each point. They concluded that it is impossible to predict the seismic response using 1-D models and proposed that the response had to be controlled by the 2- and 3-D geometry of the basin.

Luzón (1995) used a 2-D profile of the Zafarraya Basin to model numerically its seismic response under the incidence of plane waves and obtained a good qualitative agreement with the results of Morales *et al.* (1991). Luzón (1995) concluded that the amplifications observed by Morales *et al.*, at different positions, were related to the surface waves generated at the edges of the basin. On the other hand, Schenková & Zahradník (1996) used the finite-differences method to calculate the transfer functions at various 2-D models of Zafarraya Basin under incident plane waves, and found that the observed features by Morales *et al.* (1991) could be explained satisfactorily by a 2-D model with a horizontally layered basin fill.

Table 1. Physical properties for the 3-D model of Zafarraya Basin.

Medium	α (m s^{-1})	β (m s^{-1})	ρ (g cm^{-3})	Q_α	Q_β
Clay-marl sediment	1140	650	2.1	150	100
Carbonatic rock	3500	2000	2.5	150	100

Until now, no specific experiment has been done to determine the elastic properties of the Zafarraya Basin such as seismic wave velocities, rock densities, etc. Nevertheless, the materials which form this basin and the surrounding bedrock are known from field observations (Morales 1991). These observations propose that the bedrock is a carbonate rock, whereas great part of the filling of the basin is composed by clay marl sediments. The physical properties for our 3-D model correspond to those used in the previously cited work of Schenková & Zahradník (1996) for this kind of materials in the Zafarraya Basin (Table 1).

To account for anelastic attenuation we have set constant quality factors ($Q_{\alpha,\beta}$) equal to 150 for P- and to 100 for S-waves in both the hard rock and the basin. The value for Q_β has been adopted regarding the models of Q for S waves proposed by Canas *et al.* (1988), for the south of Spain, who used a generalized inversion technique applied to the attenuation of Rayleigh waves. As a result of the uncertainty on Q_α we selected the above value taking into account that its higher limit was that provided by the expression

$$Q_\alpha = \frac{4}{3}\left(\frac{\beta}{\alpha}\right)^2 Q_\beta \approx 230, \tag{1}$$

which corresponds with the case when the energetic losses in dilatation are negligible compared with those in shear (Kennett 1983).

SHORT DESCRIPTION OF THE IBEM

The IBEM, based on the boundary integral representation of displacements and tractions, formulates the problem of the diffraction and refraction of elastic waves in terms of boundary-force densities.

Consider an alluvial valley R on the surface of a half-space which is named the external region E. Assuming harmonic excitation, the refracted displacement component $u_i^r(\mathbf{x})$ inside the basin can be expressed as (see Sánchez-Sesma & Campillo 1991)

$$u_i^r(\mathbf{x}) = \int_{S_R} \phi_j^R(\xi) G_{ij}^R(\mathbf{x}, \xi)\, dS_\xi, \tag{2}$$

where $G_{ij}^R(\mathbf{x}, \xi)$ = Green's function of the elastic region R (the Green function is the displacement produced in the direction i at x due to the application of a harmonic unit force at the point ξ in the direction j), $\phi_j^R(\xi)$= force density in the direction j at ξ and S_R = boundary of region R. In this equation and hereafter the explicit frequency dependence $e^{-i\omega t}$ is omitted. The total wavefield in the half-space is the sum of the so-called *free-field* and *diffracted* wave

$$u_i(\mathbf{x}) = u_i^{(0)}(\mathbf{x}) + u_i^{(d)}(\mathbf{x}) = u_i^{(0)}(x) + \int_{S_E} \phi_j^E(\xi) G_{ij}^E(\mathbf{x}, \xi)\, dS_\xi, \tag{3}$$

where $u_i^{(0)}(\mathbf{x})$ = displacement associated to the free-field, i.e. the motion in absence of any irregularity, which includes incident and reflected waves by the half-space free surface, $u_i^{(d)}(\mathbf{x})$ = displacement produced by the diffracted waves, and $G_{ij}^E(\mathbf{x}, \xi)$ = Green's function of the region E. Tractions can be obtained by direct application of Hooke's law and by equilibrium considerations around an

internal neighbourhood of the boundary as,

$$t_i(\mathbf{x}) = k\phi_i(\mathbf{x}) + \int_S \phi_j(\xi) T_{ij}(\mathbf{x}, \boldsymbol{\xi})\, dS_\xi, \tag{4}$$

where T_{ij} $(\mathbf{x}, \boldsymbol{\xi})$ = traction Green's function; k is equal to zero if $\mathbf{x}$ is not at the boundary of the elastic space, and equal to $1/2$ or $-1/2$ if $\mathbf{x}$ tends to the boundary from inside or outside of the space, respectively. Eq. (4) is used to compute the tractions for both media: the half-space E (plus incident traction one), and the sedimentary basin R.

Boundary conditions

Boundary conditions are established by considering that tractions equal zero on the free surface and the continuity of displacements and tractions at the common interface between both media. The continuity of displacements and tractions can be expressed by the following equations:

$$u_i^r(\mathbf{x}) = u_i^{(0)}(\mathbf{x}) + u_i^{(d)}(\mathbf{x}) \tag{5}$$

that is

$$\int_{S_R} \phi_j^R(\boldsymbol{\xi}) G_{ij}^R(\mathbf{x}, \xi)\, dS_\xi = u_i^{(0)}(\mathbf{x}) + \int_{S_E} \phi_j^E(\xi) G_{ij}^E(\mathbf{x}, \xi)\, dS_\xi \tag{6}$$

for the displacements, and

$$t_i^r(x) = t_i^{(0)}(\mathbf{x}) + t_i^{(d)}(\mathbf{x}) \tag{7}$$

that is

$$k\phi_i^R(\mathbf{x}) + \int_{S_R} \phi_j^R(\xi) T_{ij}^R(\mathbf{x}, \xi)\, dS_\xi = t_i^{(0)}(\mathbf{x}) + k\phi_i^E(\mathbf{x}) + \int_{S_E} \phi_j^E(\xi) T_{ij}^E(\mathbf{x}, \xi)\, dS_\xi \tag{8}$$

for the tractions. On the other hand, zero tractions on the free surface of the basin and of the half-space, provide the next equations,

$$t_i^{(0)}(\mathbf{x}) + t_i^{(d)}(\mathbf{x}) = 0 \tag{9}$$

or

$$t_i^{(0)}(\mathbf{x}) + k\phi_i^E(\mathbf{x}) + \int_{S_E} \phi_j^E(\xi) T_{ij}^E(\mathbf{x}, \xi)\, dS_\xi = 0 \tag{10}$$

for the free surface of E, and

$$t_i^{(r)}(\mathbf{x}) = 0 \tag{11}$$

that is

$$k\phi_i^R(\mathbf{x}) + \int_{S_R} \phi_j^R(\xi) T_{ij}^R(\mathbf{x}, \xi)\, dS_\xi = 0 \tag{12}$$

valid on the free surface of R. Eqs (6), (8), (10) and (12) form a linear system of integral equations for boundary sources, i.e. those producing the diffracted and the refracted fields. The discretized versions of these equations, as shown in the next section, provide a system of linear equations that once is solved, the diffracted and refracted displacement fields at any point inside and outside of the sedimentary inclusion can be computed.

Discretization of the surfaces

Consider that M, L and K are the number of elements in the discretized part of the flat surface of the half-space E, the common interface shared by the spaces E and R, and the free surface of region R, respectively. It becomes clear that the total number of equations is $3M + 6L + 3K$, which is the same as the number of unknowns, $\phi_i^{R,E}$. If we assume that the force densities $\phi_i^{R,E}$ are constant over each of the boundary elements, it is possible to discretize the system of integral equations, as discussed in the precedent section, to construct a system of linear equations. In order to clarify these ideas, let us consider the discretized versions of the diffracted displacements and tractions. The displacements can be expressed as

$$u_i^{(d)}(\mathbf{x}) = \sum_{l=1}^{N} \phi_j^E(\xi_l) g_{ij}^E(\mathbf{x}, \xi_l) \tag{13}$$

with $N = M + L$ and

$$g_{ij}^E(\mathbf{x}, \xi_l) = \int_{\Delta S_l} G_{ij}^E(\mathbf{x}, \xi_l)\, dS_\xi. \tag{14}$$

The tractions are represented as

$$t_i^{(d)}(\mathbf{x}) = \sum_{l=1}^{N} \phi_j^E(\xi_l) t_{ij}^E(\mathbf{x}, \xi_l), \tag{15}$$

where

$$t_{ij}^E(\mathbf{x}_n, \xi_l) = k\delta_{ij}\delta_{nl} + \int_{\Delta S_l} T_{ij}^E(\mathbf{x}_n, \xi_l)\, dS_\xi, \tag{16}$$

and δ_{ij} is the Kronecker delta. The integrals in eq. (14) are computed numerically with a Gaussian integration rule, except in the case when x is in the neighbourhood of ξ_l, for which analytical expressions can be obtained (for more details see Sánchez-Sesma & Luzón 1995, hereafter referred to as SSL). The integral in eq. (16) can be also computed numerically by using Gaussian integration, except when $x_n = \xi_l$. In this case, we have

$$t_{ij}^E(\mathbf{x}_n, \xi_l) = k\delta_{ij}. \tag{17}$$

Let us express eqs (6), (8), (10) and (12) in terms of the discretized versions of the displacements and of the tractions as defined in (13) and (15). In this way, boundary conditions lead to the following linear system of equations

$$\sum_{l=1}^{N} \phi_j^E(\xi_l) g_{ij}^E(\mathbf{x}, \xi_l) - \sum_{l=1}^{N'} \phi_j^R(\xi_l) g_{ij}^R(\mathbf{x}, \xi_l) = -u_i^{(0)}(\mathbf{x}) \tag{18}$$

$$\sum_{l=1}^{N} \phi_j^E(\xi_l) t_{ij}^E(\mathbf{x}, \xi_l) - \sum_{l=1}^{N'} \phi_j^R(\xi_l) t_{ij}^R(\mathbf{x}, \xi_l) = -t_i^{(0)}(\mathbf{x}) \tag{19}$$

$$\sum_{l=1}^{N} \phi_j^E(\xi_l) t_{ij}^E(\mathbf{x}, \xi_l) = 0 \tag{20}$$

$$\sum_{l=1}^{N'} \phi_j^R(\xi_l) t_{ij}^R(\mathbf{x}, \xi_l) = 0, \tag{21}$$

where $N' = L + K$. After solving this system, we are able to compute the diffracted and refracted displacement fields by using again the discretized representation of the displacements in each space. The accuracy of this approach has been verified by SSL where analytical expressions of the Green functions in the 3-D full space can be found as well. The IBEM seems to be a very efficient method as the only approximation involved for its implementation comes from the discretization stage, and any irregular geometry can be handled as well as any type of incident wave.

We have discretized all the surfaces evolved in the problem dynamically, that is we did not set a unique discretization, but we did a

discretization process for each frequency computed, in such a way that we always had at least 4.5 boundary elements per wavelength of S waves in each space. As a result of the surface geometry of the basin, the flat free surface of the bedrock was discretized up to distances r, from the centre of the model, smaller than

$$r \leq \frac{x^2}{a^2} + \frac{y^2}{b^2} - 1. \tag{22}$$

In this ellipsoidal constrain, x and y correspond to the East and North directions, respectively, and $a = 8$ km, and $b = 5$ km.

THE MATRIX STATIC CONDENSATION ALGORITHM

In order to reduce the floating-point operations and storage requirements involved by the IBEM we use the matrix static condensation algorithm (MSCA). Let us express eqs (17), (18), (19) and (20) in the following matrix form

$$\begin{pmatrix} G_{L_R}^{M_E} & G_{L_R}^{L_E} & G_{L_R}^{L_R} & G_{L_R}^{K_R} \\ T_{L_E}^{M_E} & T_{L_E}^{L_E} & T_{L_E}^{L_R} & T_{L_E}^{K_R} \\ T_{M_E}^{M_E} & T_{M_E}^{L_E} & 0_{M_E}^{L_R} & 0_{M_E}^{K_R} \\ 0_{K_R}^{M_E} & 0_{K_R}^{L_E} & T_{K_R}^{L_R} & T_{K_R}^{K_R} \end{pmatrix} \begin{pmatrix} \phi_{M_E} \\ \phi_{L_E} \\ \phi_{L_R} \\ \phi_{K_R} \end{pmatrix} = \begin{pmatrix} -u_{L_R} \\ -t_{L_E} \\ 0_{M_E} \\ 0_{K_R} \end{pmatrix}, \tag{23}$$

where each block $0_{M_E}^{L_R}$, $0_{M_E}^{K_R}$, $0_{K_R}^{M_E}$ and $0_{K_R}^{L_E}$ is a zero submatrix, and every term 0_{M_E} and 0_{K_R} is a zero subvector. Note that when solving this linear system of eq. (23) the number of elements that has this matrix is $[(3M + 6L + 3K)]^2$. This can be resolved for example using an $L \cdot U$ decomposition (see e.g. Press *et al.* 1992) as was done by SSL who calculated the response of 3-D alluvial basins up to relatively low frequencies.

However, in this kind of problems the size of the coefficient matrix, corresponding to the linear system, grows with the square of the frequency, and therefore the computational requirements can be too large for some real sedimentary deposits. The paper of Ortiz-Alemán *et al.* (1998) worked along this line, and using a threshold criteria in which the contributions from the boundary elements located outside a distance ratio from the point of tractions evaluation were removed, the full matrix was converted into a sparse one. After, using a biconjugate gradient approach reproduced the results of Luzón *et al.* (1997) who studied the diffraction of P, S and Rayleigh waves by 3-D topographies.

With the algorithm used in this work, the linear system of equations written above becomes into several small linear systems of equations that can be solved with less amount of memory than the original system. The MSCA is based on an implicit factorization of the coefficient matrix by taking advantage of the structure of the matrix and taking out the zero blocks from the computations. Let us define the following matrices

$$\left[T_{M_E}^{M_E}\right]^{-1} T_{M_E}^{L_E} = A_1 \tag{24}$$

$$\left[T_{K_R}^{K_R}\right]^{-1} T_{K_R}^{L_R} = A_2. \tag{25}$$

In this way, we can use the third and fourth block-rows of the system presented in (23) to obtain

$$\phi_{M_E} = -A_1 \phi_{L_E} \tag{26}$$

$$\phi_{K_R} = -A_2 \phi_{L_R}, \tag{27}$$

which can be used to calculate ϕ_{M_E} and ϕ_{K_R} once known ϕ_{L_E} and ϕ_{L_R}. Defining now the following matrices

$$G_{L_R}^{L_E} - G_{L_R}^{M_E} A_1 = B_{11} \tag{28}$$

$$G_{L_R}^{L_R} - G_{L_R}^{K_R} A_2 = B_{12} \tag{29}$$

$$T_{L_E}^{L_E} - T_{L_E}^{M_E} A_1 = B_{21} \tag{30}$$

$$T_{L_E}^{L_R} - T_{L_E}^{K_R} A_2 = B_{22} \tag{31}$$

it is possible to express the first and second block-rows of the system (23) as

$$\begin{pmatrix} B_{11} & B_{12} \\ B_{21} & B_{22} \end{pmatrix} \begin{pmatrix} \phi_{L_E} \\ \phi_{L_R} \end{pmatrix} = \begin{pmatrix} -u_{L_R} \\ -t_{L_E} \end{pmatrix}. \tag{32}$$

This is a new compact system of linear equations with only $6L$ unknowns. Once resolved, the final step in the algorithm consists in the computation of the already unknown vectors, ϕ_{M_E} and ϕ_{K_R} using eqs (26) and (27). The system of eqs (32), that is now resolved using the $L \cdot U$ decomposition, is the greatest system that it is necessary to calculate with the MSCA, and therefore the memory requirements of the computer used are lower. For example, in the Zafarraya Basin the full matrix corresponding to the frequency of 1.004 Hz requires around 1372 Mb, whereas the matrix in (32) used with the MSCA need only 441 Mb. In fact, with this algorithm it is possible to compute, with the same RAM and with the same 3-D problem, the solution corresponding to approximately twice the highest frequency calculated using the system of (23) and preserving the same accuracy as resolving this full system.

RESULTS FOR THE 3-D ZAFARRAYA BASIN MODEL

We computed, in the frequency domain, the seismic response of the Zafarraya Basin for 90 frequencies up to 1.335 Hz, for incident P, SV and SH plane waves with an azimuth angle $\phi = 60°$. The first results that we present here are the amplification patterns for incident SH waves. We have selected an incident angle of 30° with respect to the vertical. The results can be seen in Fig. 2, for the three components of the displacement: radial, transverse and vertical components. These plots correspond to the displacements produced in the free surface when an incident SH wave with amplitude equal to one is considered. Therefore, for the transverse component of the displacement in the free surface of the half-space, the amplitude of the observed motion is approximately twice the incident one, as is expected.

For the sake of comparison, the amplification patterns for the selected frequencies (0.602, 0.909 and 1.19 Hz.) are displayed at the same range of amplitudes for each component. Note that the 3-D response of Zafarraya Basin is more complex than the obtained using 1- or 2-D models. As is known, the radial and vertical components in 1- and 2-D models are equal to zero, whereas our 3-D results show that the vertical displacement is comparable to the amplitude of the incident-transverse one, and that the radial is almost twice at 0.909 Hz over the southern part of our model. Moreover, in the radial motion, the amplification of the soil motion rises to the value of 8 at the frequency of 1.19 Hz inside the basin. On the other hand, for the transverse component the basin produces large amplifications. In particular, for the frequencies of 0.909 and 1.19 Hz the amplification reaches up to nearly 12 times the amplitude of the incoming wave at those places where the depths of the basin are larger, whereas the 1-D response for a flat layer without damping predicts a maximum amplification equal to 2 times the impedance contrast, that is $2 \cdot 3.66 = 7.32$.

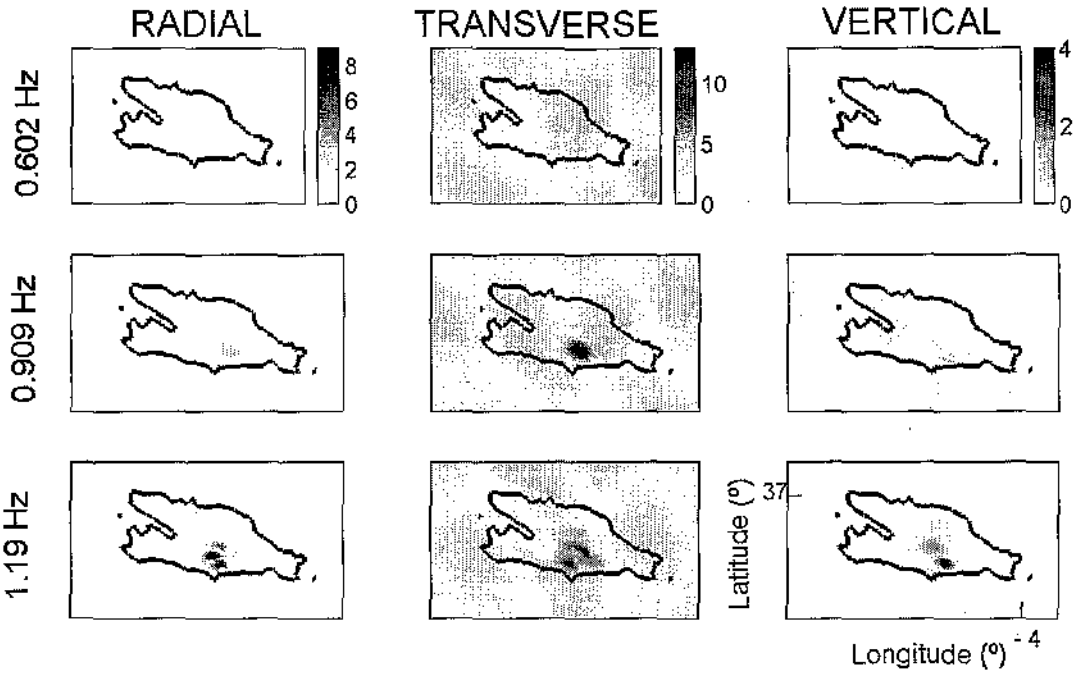

Figure 2. Amplifications of the three components of the displacement at various frequencies in the Zafarraya Basin for an incident *SH* wave with 30° respect to the vertical, and with an azimuthal angle of $\phi = 60°$. The latitude and longitude are expressed in degrees. It is shown the level contour of depth zero of the basin for reference.

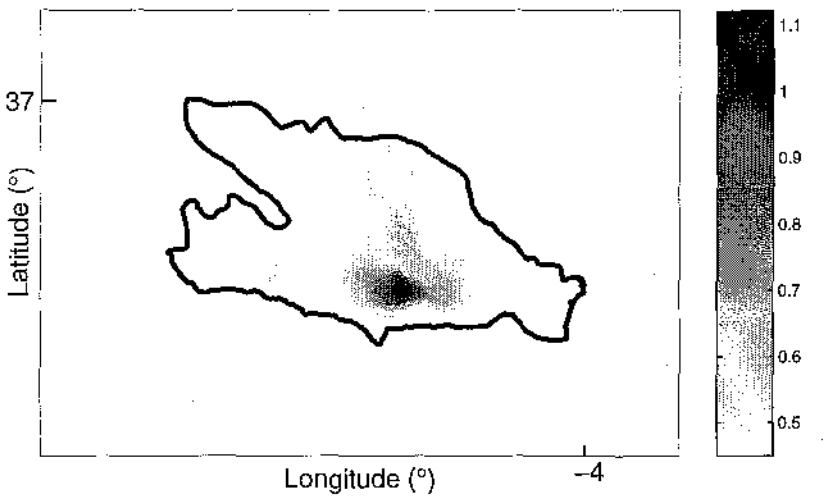

Figure 3. Maximum absolute values of the radial displacements in the Zafarraya Basin produced by a *P* wave propagating with an azimuthal angle of $\phi = 60°$ and with 30° with respect to the vertical. The zero-depth contour of the basin is shown for reference. The characteristic period to compute the synthetic temporal history is of $t_p = 1.5$ s, and the time-lag of $t_s = 20$ s.

In order to simulate ground motion with the time we used the FFT algorithm to compute synthetic seismograms on the free surface of the model. The input source function used was a Ricker wavelet, which waveform has a temporal dependence given by

$$R(t) = \left[a(t) - \frac{1}{2}\right] e^{-a(t)}, \tag{33}$$

where

$$a(t) = \left[\frac{\pi(t - t_s)}{t_p}\right]^2 \tag{34}$$

where t_p = characteristic period and t_s = time-lag, that is, the time at which the minimum of the wavelet reaches the origin of the reference system. In our computations we used a $t_p = 1.5$ s (or characteristic frequency of 0.6666 Hz) and $t_s = 20$ s.

Using these results, we have calculated the peak-ground-motion in the case of the incidence of *P* waves coming from the north–east and with an incidence angle of 30° relative to the vertical. This is shown in Fig. 3, where the maximum absolute values of the radial displacement can be observed. The strongest ground motion is found at sites where the basin is deeper and about its centre. This effect is more prominent for the radial component than for the vertical and transverse ones (not shown here). The same type of results for incident *SV* waves with the same incident angle of 30° are shown in Fig. 4. The amplifications for the *SV* incidence are greater than those produced by the longitudinal waves. Anyway, the zones where

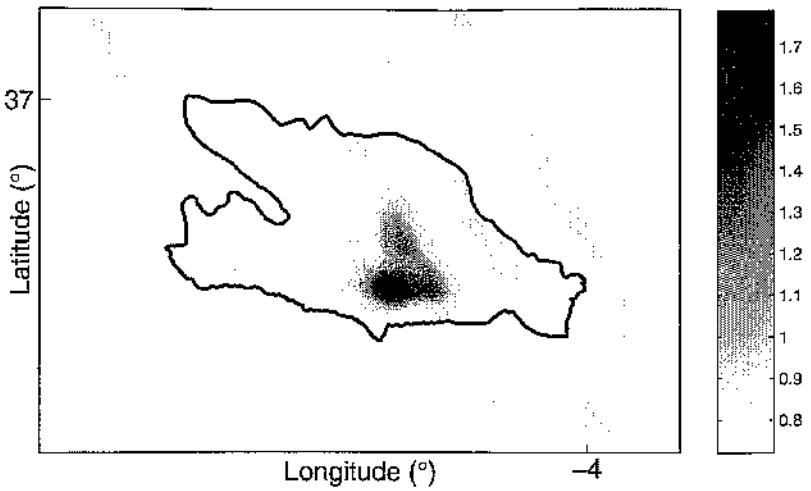

Figure 4. Same as Fig. 3 but for an incident *SV* wave.

the motion is more amplified inside the basin are the same for both *P* and *SV* waves. For a better understanding of the behaviour of our 3-D model for these incident *SV* waves, we represent in Fig. 5 the horizontal particle trajectories in an array of selected points inside and outside the sediments for the whole time history. Also it is noted that the projection of particle motion of the incident wave for reference. These plots are known as polarization diagrams or hodograms. At those places where the basin has greater depths the horizontal polarization patterns shows a little rotation with more amplitudes in the radial direction of the incident wave. The rotation of the horizontal motion of a particle has been observed in México city using real records, and has been interpreted as being due to the interference of locally generated surface waves at México valley (Sánchez-Sesma *et al.* 1993). Another interesting feature corresponds to the energy in the N–S displacements observed at the stations located on the south and outside of the basin. As the direct wave produces only energy in the radial (and vertical) displacements, the amplitudes observed in the N–S displacements have to be generated by the influence of the sedimentary inclusion. In fact, the south part of the basin has a very steep slope almost with east–west direction, and it acts as a very good diffractor producing the emission of energy at least to the south. Similar effects associated with the diffraction of seismic waves by similar structures have been observed previously, as for example the generation of surface waves in a very steep interface of the Salt Lake valley, Utah (Hill *et al.* 1990). The polarization diagrams produced in the radial-vertical plane for the same receivers as in the Fig. 5 are shown in Fig. 6. In this case the energy radiated from the basin on this plane is not only towards to the south of the half-space, but also towards the west and south–west. That is, in the contrary part where the incident waves are shooting the basin. As we can observe in Fig. 6, the ground motion inside the sedimentary part is generally more complex than that observed on the hard rock. At those places where the model is deeper the surface displacements at the radial-vertical section are characterized by a rotation pattern of great amplitude in comparison with the observed in the particle motion of the incident wave.

In order to study the motion at the receivers of the two perpendicular profiles A–B and A′–B′ of Fig. 1, we computed the synthetic seismograms of vertical (V), radial (R) and transverse (T) components of the displacement produced by the incidence of *SV* waves in Fig. 7. At these synthetics some numerical noise before the incident wave is observed. Anyway, it is negligible and takes values less that 1 per cent of the maximum amplitudes in the signals. As has been observed in previous results (Figs 4–6), the maximum displacements for both profiles A–B and A′–B′ are on the radial component and in those stations where the model has the highest depths. In these receivers and for the radial motion the signal duration is also amplified when compared with the direct incident pulse. In fact, important displacements exist even up to 26 s, which are interpreted as interferences of surface waves reflected at the edges of the basin. The energy is emitted in all directions and is detected on the vertical and transverse seismograms as well. Part of the energy on these rebounds is refracted to the hard-rock as can be observed at the stations located on the free surface of the half-space. Anyway, the amplitude of the waves emitted to the basement is low in comparison with the direct one and those that propagate inside the basin later.

CONCLUDING REMARKS

We have computed the seismic response of a 3-D model of the Zafarraya Basin using the IBEM for incident *P* and *S* plane waves. With MSCA we solve the linear system of equations that arise in this technique. We reordered rows and columns of the matrix in order to have block matrices and found the system has a particular structure that can be easily constructed by using a static matrix condensation scheme. Some of the blocks are all zeros and can be completely eliminated in numerical computations, and therefore gives the possibility of computing higher frequencies in a 3-D problem.

In both *P* and *S* incident waves, the greatest displacements are produced on the excited component of the direct waves (radial for *P* and *SV* waves, and transverse for *SH* waves). This emphasizes the importance of the location of the seismic source or the azimuth of the incident waves, as the radial and transverse displacements are defined by the azimuthal angle.

The 3-D response of Zafarraya for incident *SH* waves produces important amplitudes over the receivers located at the south of the model in the three components of the motion and, for example, some displacements observed on the radial motion are approximately equal to the maximum expected value for the transverse component when a 1-D model of the Zafarraya Basin is used. The seismograms computed for incident *SV* waves show that the horizontal (transverse and radial) motion is greatly amplified both in amplitude and duration at those receivers where the depths of the basin are larger. Some of the waves that have produced the increase

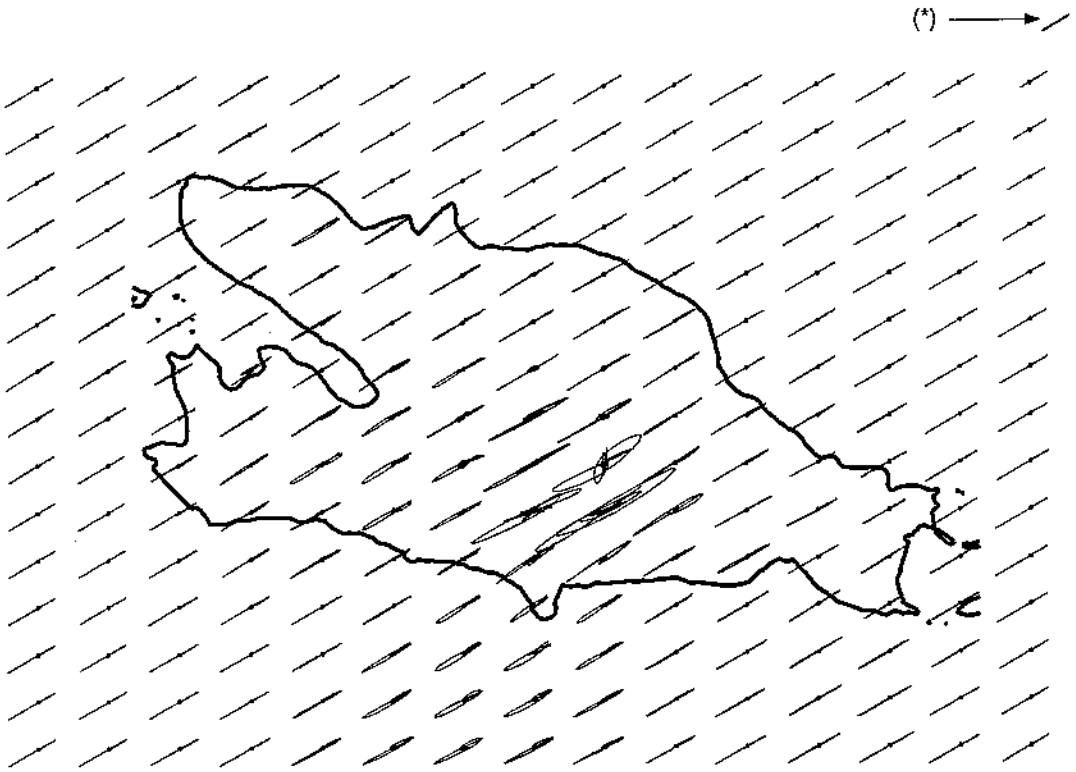

Figure 5. Horizontal particle motion due to the incidence of *SV* waves propagating with an azimuthal angle of $\phi = 60°$ and with 30° with respect to the vertical. The characteristic period is of $t_p = 1.5$ s, and the time-lag of $t_s = 20$ s. (*) In the upper-right part is noted with an arrow the projection of particle motion of the incident wave for reference.

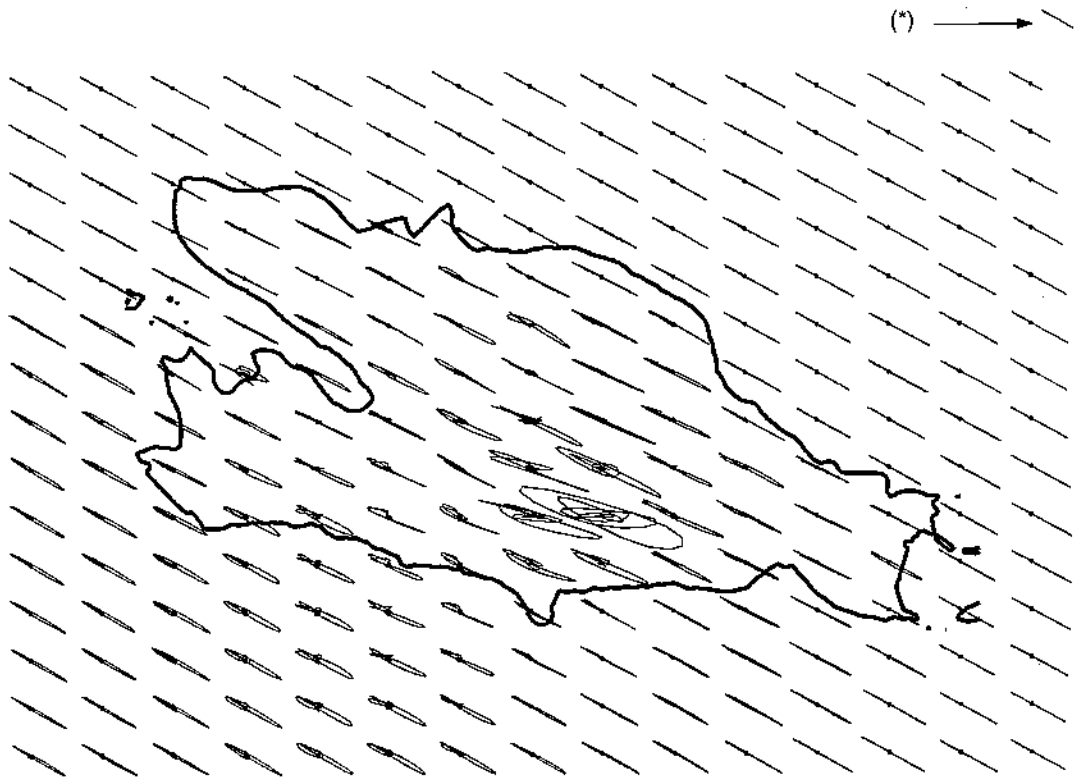

Figure 6. Vertical-radial particle motion due to the incidence of *SV* waves propagating with an azimuthal angle of $\phi = 60°$ and with 30° with respect to the vertical. The vertical axis represents the vertical motion, whereas in the horizontal axis the radial displacement is shown. The characteristic period is of $t_p = 1.5$ s, and the time-lag of $t_s = 20$ s. (*) In the upper-right part is noted with an arrow the projection of particle motion of the incident wave for reference.

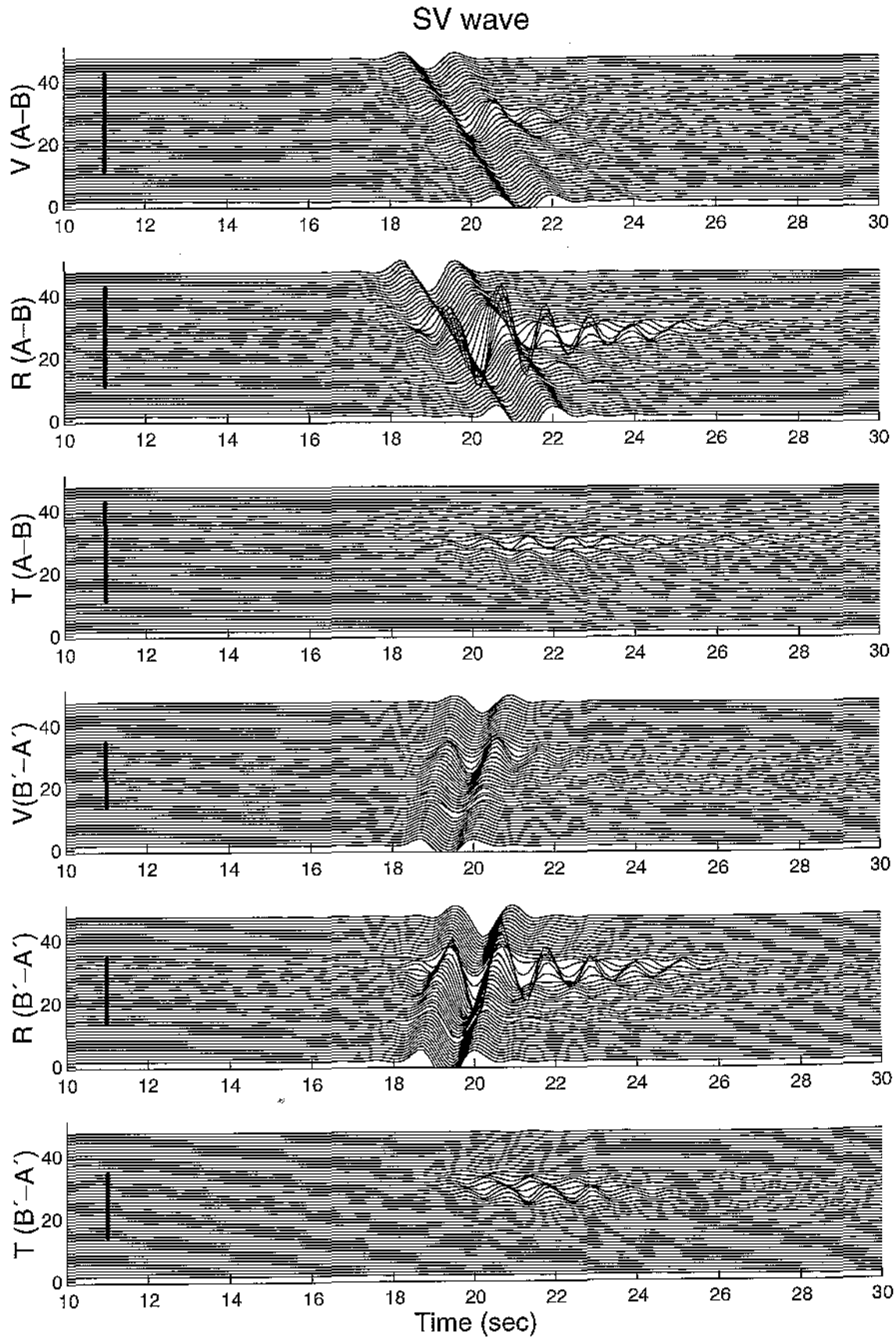

Figure 7. Seismograms of the vertical (V), radial (R) and transverse (T) components of the displacement at the 47 receivers of the A′–B′ and A–B profiles. The seismograms corresponding to receivers located inside the Zafarraya Basin are marked with a black line bar at the left. The characteristic period is of $t_p = 1.5$ s, and the time-lag of $t_s = 20$ s.

in the duration are interpreted as surface waves and their reflections at the edges of the basin, which produce characteristic polarization patterns showing the particle rotation at both the horizontal and vertical-radial planes.

The results we had, are not only a significant contribution in the knowledge of the complex seismic response of the Zafarraya Basin, but it is of interest for other similar sedimentary basins. Of course, the seismic response of each 3-D basin has its own amplification patterns and depends strongly on the properties of the basin, such as the impedance contrast, wave velocities or the geometry of the structure, and therefore each behaviour is not quantitatively portable from one basin to other. Various features characterize the Zafarraya Basin, which could be observed in other sedimentary structures; that is, it is a medium–small basin with maximum depths approximately 200 m, with an impedance contrast of 3.66, and with a very strong slope in one edge. Qualitatively speaking, two characteristics in the seismic response have been observed in the range of frequencies dealt with in this study: first, the amplification patterns of the displacement for all the incident waves have their maximum levels at those locations where the depths of the basin are larger, and second, the very pronounced slope in the edges of the model acts as a very good diffractor producing the emission of waves inside and outside of the sedimentary inclusion.

Finally, one of the more important conclusions that we can obtain from this work is that a simple 3-D model allows us to point out important site effects that may influence the seismic motion of future earthquakes in the Zafarraya Basin up to 1.335 Hz. These results can be regarded as preliminary, but they indicate that is necessary to take into account the 3-D character of nature and should stimulate further research. Future studies have to be aimed towards the consideration of other aspects that provide a more realistic description of the seismic response of this basin: the use of nearby sources considering an appropriate rupture propagation and radiation patterns; the inclusion of a sedimentary layering in future models as was proposed by Schenková & Zahradník (1996); and the use of improved numerical methods to compute the solution for higher frequencies. Of course, the calibration of these and other numerical results with records obtained with permanent or temporal seismic stations is a necessary step to assess the complex response of a 3-D sedimentary structure such as the Zafarraya Basin, as has been recently pointed by Rovelli *et al.* (2001).

ACKNOWLEDGMENTS

We thank De Martin-Barry's family for a review of the manuscript, and Dr I. Oprsal and an anonymous reviewer for their helpful suggestions. This work was partially supported by CICYT, Spain, under grant REN2002-04198-C02-02/RIES, by the European Community with FEDER, by the research team of *Geofísica Aplicada* (RNM194) of Junta de Andalucía, Spain and by CONACYT, Mexico, under Project NC-204.

REFERENCES

Canas, J.A., De Miguel, F., Vidal, F. & Alguacil, G., 1988. Anelastic Rayleigh wave attenuation in the Iberian Peninsula, *Geophys. J. Int.* **95**, 391–396.

Chávez-García, F.J., Castillo, J. & Stephenson, W.R., 2002. 3D site effects: a thorough analysis of a high-quality dataset, *Bull. seism. Soc. Am.*, **92**, 1941–1951.

Chirlaque, M., Díaz, M., García, A.J., García, E., Guillén, F. & Jiménez, J.C., 1987. *Estudio geoeléctrico del polje de Zafarraya,* Facultad de Ciencias, Dpto. de Geodinámica. University of Granada, Spain, p. 129 (in Spanish).

Frankel, A. & Stephenson, W., 2000. Three-dimensional simulations of ground motions in the Seattle region for earthquakes in the Seattle fault zone, *Bull. seism. Soc. Am.*, **90**, 1251–1267.

Gil-Zepeda, S.A., Luzón, F., Aguirre, J., Morales, J., Sánchez-Sesma, F.J. & Ortiz-Alemán, C., 2002. 3-D Seismic Response of the deep basement structure of the Granada Basin (Southern Spain), *Bull. seism. Soc. Am.*, **92**, 2163–2176.

IASPEI–IAEE Joint Working Group on ESG, Japanese National Working Group on ESG, Earthquake Engineering Research Liaison Committee, Science Council of Japan & Association for Earthquake Disaster Prevention, 1992. *Proc. Int. Symp. on the Effects of Surface Geology on Seismic Motion,* March 25–27, 1002, Odawara, Japan.

IASPEI–IAEE Joint Working Group on ESG, Japanese National Working Group on ESG & Association for Earthquake Disaster Prevention, 1998. *Proc. 2nd Int. Symp. on the Effects of Surface Geology on Seismic Motion,* eds Irikura, K., Kudo, K., Okada, H. & Sasatani, T., December 1–3, 1998, Yokohama, Japan.

Kennett, B.L.N., 1983. *Seismic Wave Propagation in Stratified Media.* Cambridge University Press, Cambridge.

Hill, J., Benz, H., Murphy, M. & Schuster, G.T., 1990. Propagation and resonance of *SH* waves in the Salt Lake Valley, Utah, *Bull. seism. Soc. Am.*, **80**, 23–42.

Luzón, F., 1995. Determinación de la respuesta sísmica de estructuras geológicas superficiales mediante el método indirecto de elementos en la frontera, *PhD thesis,* University of Granada, Spain (in Spanish).

Luzón, F., Sánchez-Sesma, F.J., Rodríguez-Zúñiga, J.L., Posadas, A.M., García, J.M., Martín, J., Romacho, M.D. & Navarro, M., 1997. Diffraction of *P, S* and Rayleigh waves by three-dimensional topographies, *Geophys. J. Int.* **129**, 571–578.

Morales, J., 1991. Caracterización de la respuesta sísmica local en las cuencas de Granada (España) y Ciudad Guzman (Mexico) mediante el análisis espectral de microterremotos y terremotos, *PhD thesis,* University of Granada, Spain (in Spanish).

Morales, J., Vidal, F., Peña, J.A., Alguacil, G. & Ibáñez, J., 1991. Microtremor study in the sediment filled basin of Zafarraya, Granada (Southern Spain), *Bull. seism. Soc. Am.*, **81**, 687–693.

Norma de Construcción Sismorresistente NCSE-94, 1995. *Boletín Oficial del Estado* February 8. Ministerio Obras Públicas, Transportes y Medio Ambiente, 3935–3980, Madrid (in Spanish).

Olsen, K.B., 2000. Site amplification in the Los Angeles Basin from three-dimensional modeling of ground motion, *Bull. seism. Soc. Am.*, **90**, S77–S94.

Olsen, K.B. & Archuleta, R.J., 1996. Three-dimensional simulation of earthquakes on the Los Angeles fault system, *Bull. seism. Soc. Am.*, **86**, 575–596.

Olsen, K.B., Pechmann, J.C. & Schuster, G.T., 1995. Simulation of 3D elastic wave propagation in the Salt Lake Basin, *Bull. seism. Soc. Am.*, **85**, 1688–1710.

Ortiz-Alemán, C., Sánchez-Sesma, F.J., Rodríguez-Zúñiga, J.L. & Luzón, F., 1998. Computing topographical 3D site effects using a fast IBEM/Conjugate gradient approach, *Bull. seism. Soc. Am.*, **88**, 393–399.

Press, W.H., Teukolsky, S.A., Vetterling, W.T. & Flannery, B.P., 1992. *Numerical Recipes in Fortran. The Art of Scientific Computing,* Cambridge University Press, New York.

Reicherter, K.R., 2001. Paleoseismologic advances in the Granada Basin (Betic cordilleras, Southern Spain), *Acta Geológica Hispánica,* **36**, 278–281.

Reicherter, K., Jabaloy, A., Galindo-Zaldívar, J., Ruano, P., Becker-Heidmann, P., Morales, J., Reiss, S. & González-Lodeiro, F., 2002. Holocene palaeoseismic history of the Ventas de Zafarraya Fault (Central Betic Cordilleras, SE Spain), *Proc. Symp., 100 años de Simología en Granada,* University of Granada.

Rovelli, A., Scognamiglio, L., Marra, F. & Caserta, A., 2001. Edge-diffracted 1-s surface waves observed in a small-size intramountain basin (Colfiorito, Central Italy), *Bull. seism. Soc. Am.*, **91**, 1581–1866.

Sánchez-Sesma, F.J. & Campillo, M., 1991. Diffraction of *P*, *SV*, and Rayleigh waves by topographic features: a boundary integral formulation, *Bull. seism. Soc. Am.*, **81**, 2234–2253.

Sánchez-Sesma, F.J. & Luzón, F., 1995. Seismic response of three dimensional alluvial valleys for incident *P, S* and Rayleigh waves, *Bull. seism. Soc. Am.*, **85**, 269–284.

Sánchez-Sesma, F.J., Pérez-Rocha, L.E. & Reinoso, E., 1993. Ground motion in Mexico city during the April 25, 1989, Guerrero earthquake, *Tectonophysics*, **218**, 127–140.

Schenková, Z. & Zahradník, J., 1996. Interpretation of the microtremor spectra at the Zafarraya Basin, southern Spain, *Soil Dynam. Earthq. Eng.*, **15**, 69–73.

Vidal, F., 1986. Sismotectónica de la Región Béticas-Mar de Alborán., *PhD thesis*, University of Granada, Spain (in Spanish).

Apéndice C

Un método híbrido del elemento indirecto en la frontera – número de onda discreto aplicado a la simulación de la respuesta sísmica de valles aluviales estratificados.

Un método híbrido de elemento indirecto de frontera – número de onda discreto se presenta y es aplicado para el modelado del movimiento del suelo en valles aluviales estratificados bajo la incidencia de ondas planas SH para un semiespacio elástico. El método está basado en una representación integral de un estrato simple para ondas difractadas. Las ondas refractadas en la región estratificada horizontalmente pueden ser expresada como una solución de superposisión lineal para un conjunto de números de onda discretos. Estas soluciones son obtenidas en términos de propagadores de Thomson -Haskell.

ELSEVIER

Soil Dynamics and Earthquake Engineering 23 (2003) 77–86

SOIL DYNAMICS AND EARTHQUAKE ENGINEERING

www.elsevier.com/locate/soildyn

A hybrid indirect boundary element—discrete wave number method applied to simulate the seismic response of stratified alluvial valleys

S.A. Gil-Zepeda, J.C. Montalvo-Arrieta, R. Vai, F.J. Sánchez-Sesma*

Instituto de Ingeniería, UNAM, Ciudad Universitaria, Apdo. 70-472, Coyoacán, 04510 México, DF, Mexico

Accepted 13 July 2002

Abstract

A hybrid indirect boundary element – discrete wavenumber method is presented and applied to model the ground motion on stratified alluvial valleys under incident plane SH waves from an elastic half-space. The method is based on the single-layer integral representation for diffracted waves. Refracted waves in the horizontally stratified region can be expressed as a linear superposition of solutions for a set of discrete wavenumbers. These solutions are obtained in terms of the Thomson–Haskell propagators formalism. Boundary conditions of continuity of displacements and tractions along the common boundary between the half-space and the stratified region lead to a system of equations for the sources strengths and the coefficients of the plane wave expansion. Although the regions share the boundary, the discretization schemes are different for both sides: for the exterior region, it is based on the numerical and analytical integration of exact Green's functions for displacements and tractions whereas for the layered part, a collocation approach is used. In order to validate this approach results are compared for well-known cases studied in the literature. A homogeneous trapezoidal valley and a parabolic stratified valley were studied and excellent agreement with previous computations was found. An example is given for a stratified inclusion model of an alluvial deposit with an irregular interface with the half-space. Results are displayed in both frequency and time domains. These results show the significant influence of lateral heterogeneity and the emergence of locally generated surface waves in the seismic response of alluvial valleys.

Keywords: Collocation; Diffraction; Earthquakes; Elastodynamics; Green's functions; Indirect boundary element method; Locally generated surface waves; Seismic ground motion; Seismic response; Site effects; Synthetic seismograms; Stratified alluvial valley; Thomson–Haskell propagators

1. Introduction

Local geological conditions may generate significant amplification of ground motion and concentrated damage during earthquakes. There are important advances in the evaluation of such effects [1–3]. In most situations local amplification can be inferred reasonably using simple one-dimensional (1D) shear models. However, lateral heterogeneity may give rise to focusing and to locally generated surface waves; therefore, the estimates for local amplification using 1D models may be wrong. Although the physics of this phenomenon is now reasonably well understood, most of the rigorous procedures require large amounts of computer resources. We believe there is a lack of practical methods for the assessment of local amplification.

Boundary element methods (BEM) have gained increasing popularity. Recognized advantages over domain approaches are the dimensionality reduction, the relatively easy fulfillment of radiation conditions at infinity and the high accuracy of results. Excellent surveys of the available literature on BEM in elastodynamics are by Manolis and Beskos [4]; Beskos [5,6]. One useful approach is the indirect boundary element method (IBEM), which formulates the problem in terms of force densities at the boundaries [7–9].

On the other hand, in their pioneering work, Aki and Larner [10] introduced a numerical method based on a discrete superposition of homogenous and inhomogeneous plane waves. Using this technique, Bard and Bouchon [11, 12] studied alluvial valleys and pointed out the significant role of basin-induced surface waves in the valley's response and studied the resonant characteristics of these configurations as well. The Aki–Larner's technique is the departure of discrete wavenumber approximations. The combination of discrete wavenumber expansions for Green's functions with boundary integral representations has been successful in various studies of elastic wave propagation [13–15].

* Corresponding author.
E-mail address: sesma@servidor.unam.mx (F.J. Sánchez-Sesma).

0267-7261/03/$ - see front matter © 2002 Elsevier Science Ltd. All rights reserved.
PII: S0267-7261(02)00092-1

The combination of a BEM-type approach with a discrete wavenumber formulation to compute the Green's function is particularly attractive: the singularities of Green's functions are not present in each one of the terms of the discrete wavenumber expansion [14,16]. The integration along the boundary effectively makes the singularities to vanish and improves convergence as well. However, such procedures require considerable amount of computer resources. An alternative that may be welcomed for some applications could be the IBEM, with analytical Green's functions for the half-space, and a discrete wavenumber expansion for the layered part. A similar idea, that uses line sources close to the boundary, propagators for the layered part and the least-squares method, was proposed by Bravo et al. [17].

In this work we extend the Bravo et al. [17] approach by placing the sources at the very boundary [7] so that the singularities of the sources are dealt with analytically. Therefore, the IBEM is applied for the half-space. The sources strengths and the coefficients for the discrete wavenumber expansion equal in number the conditions (continuity of displacements and tractions) at the collocation points in the interface.

2. Formulation of the problem

Consider a horizontally stratified deposit in a homogenous half-space. Elastic materials occupy the entire domain. With reference to Fig. 1, we designate by S the boundary between the region R, which is the stratified medium, and the exterior domain **E**. In Fig. 1 we show also the cross-section of the stratified model and the harmonic incident SH wave. In order to compute the displacement field at the free surface, we treat the two regions separately. Continuity of displacement and traction at S will then be imposed.

2.1. Domain E

As far as the domain E is concerned, the ground motion comes from the interferences of incoming waves with reflected and diffracted ones. The total motion in the half-space is the superposition of the free-field and the so called diffracted waves:

$$v^{\mathrm{E}} = v^{(0)} + v^{(\mathrm{d})}, \tag{1}$$

where $v^{(0)}$ is the free field displacement, i.e. the solution in the absence of the irregularity. The free-field displacement at a point $\mathbf{x} = (x, z)$ is

$$v^{(0)}(\mathbf{x}) = \mathrm{e}^{-\mathrm{i}(kx-\eta z)} + \mathrm{e}^{-\mathrm{i}(kx+\eta z)}, \tag{2}$$

where $k = (\omega/\beta)\sin\gamma$ and $\eta = (\omega/\beta)\cos\gamma$ are the horizontal and vertical wavenumbers, respectively, ω is the angular frequency, β the shear waves velocity in the domain E, γ the incidence angle. We are dealing with antiplane SH waves, i.e. all of the displacement are perpendicular to the x–z plane.

Let us discretize the surface S by N straight segments of longitude ΔS and call $\xi_l = (x_l, z_l)$ the midpoint of the segment l. Neglecting body forces, the diffracted field can be written as

$$v^{(d)}(\mathbf{x}) = \sum_{l=1}^{N} \phi(\xi_l) g(\mathbf{x}, \xi_l), \tag{3}$$

where $\phi(\xi_l)$ is the unknown force density assumed to be constant (ϕ_l) along the corresponding ΔS;

$$g(\mathbf{x}, \xi) = \int_{\Delta S_l} G(\mathbf{x}, \xi)\mathrm{d}S_\xi, \tag{4}$$

where $G(\mathbf{x},\xi)$ is the Green's function of a line source in a half-space, i.e. the displacement at point $\mathbf{x}$ due to the application of two unit forces at point $\xi = (x_l, z_l)$ and at its image $\xi' = (x_l - z_l)$. Therefore, one has

$$G(\mathbf{x}, \xi) = \frac{1}{\mathrm{i}4\mu}\left[H_0^{(2)}\left(r_l\frac{\omega}{\beta}\right) + H_0^{(2)}\left(r_l'\frac{\omega}{\beta}\right)\right], \tag{5}$$

where $H_0^{(2)}(\cdot)$ is Hankel's function of the second kind and zero order, r_l and r_l' are the distances between the point $\mathbf{x}$ and the sources ξ_l and its image ξ_l', respectively. The use of an image source guarantees that the boundary conditions of null tractions at the half-space free surface are automatically satisfied in Eq. (3).

The integral in Eq. (4) is performed on the variable ξ; Gaussian integration is used. $G(\mathbf{x},\xi)$ presents a logarithmic integrable singularity at $\mathbf{x} = \xi$; where $\mathbf{x}$ is in the neighborhood of ξ, the second right term of Eq. (5) is treated numerically, while for the first one we obtained the analytical expressions from the ascending series for Hankel's functions [18]. Sánchez-Sesma and Campillo [7] presented an example for such expressions where only the leading terms of the series are retained. We considered up to quadratic terms, which is enough if the number of segments per wavelength is larger than about five.

The quantities $\phi(\xi_l)\Delta S$ represent a force distribution at the boundary. Eq. (3) is simply the discretized form of a single layer integral, that can be obtained from Somigliana identity [7], and has been studied by Kupradze [19] from the point of view of potential theory. He showed that

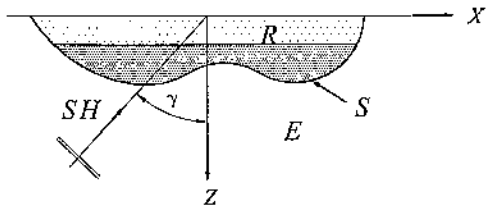

Fig. 1. Half-space, E, with a horizontally stratified alluvial valley, R. The incidence of SH waves with angle γ is depicted. The only discretization needed is along the interface S. In the free surface of the layered part and the flat surface of the half-space the boundary conditions are satisfied by construction.

the displacement field (3) continuous across S if $\phi(\xi)$ is continuous along S. The scalar 2D version that we are using is also called the Kirchhoff–Helmhotz representation [20].

Likewise the displacement field, we express the tractions in the half-space as the superposition of the contributions from the free-field and the diffracted one:

$$t^{\mathrm{E}} = t^{(0)} + t^{(\mathrm{d})}. \tag{6}$$

Since we are dealing with an antiplane problem the traction vector can be represented by a scalar quantity, when a vector $\mathbf{n}$ lying in the plane is specified. In fact, applying Hooke's law we have:

$$t^{\mathrm{E}} = \mu \frac{\partial v}{\partial \mathbf{n}}, \tag{7}$$

where $\mathbf{n}$ is assumed to be specified. Developing Eq. (7) we find Cauchy's equation:

$$t^{\mathrm{E}} = \mu \frac{\partial v}{\partial \mathbf{n}} = \mu\left(\frac{\partial v}{\partial x}\frac{\partial x}{\partial \mathbf{n}} + \frac{\partial v}{\partial z}\frac{\partial z}{\partial \mathbf{n}}\right)$$

$$= \mu\left(\frac{\partial v}{\partial x}n_x + \frac{\partial v}{\partial z}n_z\right) = \sigma_{yx}n_x + \sigma_{yz}n_z. \tag{8}$$

Therefore, the free-field traction is expressed by:

$$t^{(0)}(\mathbf{x}) = [-\mathrm{i}kn_x + \mathrm{i}\eta n_z]\mathrm{e}^{-\mathrm{i}(kx-\eta z)} - [\mathrm{i}kn_x + \mathrm{i}\eta n_z]\mathrm{e}^{-\mathrm{i}(kx+\eta z)}, \tag{9}$$

which clearly displays in the two groups of terms: the incident and reflected waves, respectively. In analogous terms the diffracted tractions can be computed by means of:

$$t^{(\mathrm{d})}(x) = \sum_{l=1}^{N} \phi(\xi_l) t(\mathbf{x}, \xi_l), \tag{10}$$

where $t^{(d)}(\mathbf{x})$ is the traction at point $\mathbf{x}$, $\phi(\xi_l) = \phi_l$, $t(\mathbf{x}, \xi)$ is given by:

$$t(\mathbf{x}, \xi) = \int_S T(\mathbf{x}, \xi)\mathrm{d}S_\xi, \tag{11}$$

where $T(\mathbf{x},\xi)$ is the traction Green's function, i.e. the traction at point $\mathbf{x}$ on the boundary S with normal $\mathbf{n}(\mathbf{x})$ (assumed to be specified and pointing outside E) due to the application of two unit forces at point ξ and at its image ξ'. Its formal expression is

$$T(\mathbf{x}, \xi_l) = \frac{\mathrm{i}\omega}{4\beta}\left[\frac{\partial r_l}{\partial \mathbf{n}}H_l^{(2)}\left(r_l\frac{\omega}{\beta}\right) + \frac{\partial r_l'}{\partial \mathbf{n}}H_l^{(2)}\left(r_l'\frac{\omega}{\beta}\right)\right], \tag{12}$$

where $H_l^{(2)}(\cdot)$ is the Hankel's function of the second kind and first order. The integral in Eq. (11) is also computed numerically using Gaussian integration. The traction Green's function presents a singularity of the form $1/r$ when $x_j = \xi_l$, in this case we obtain

$$t(\mathbf{x}_j, \xi_l) = 0.5\delta_{jl} + \int_{\Delta S_l} \frac{\mathrm{i}\omega}{4\beta}\left[\frac{\partial r_l'}{\partial \mathbf{n}}H_l^{(2)}\left(r_l'\frac{\omega}{\beta}\right)\right]\mathrm{d}S_{\xi'} \tag{13}$$

$j = l$.

δ_{jl} is the Kronecker symbol ($= 1$ if $j = l$, $= 0$ if $j \neq l$). The formal contribution from the source ξ to the integral is null because the discretization segment is a straight line and ξ_l is the midpoint. In fact, it can be verified that, under this circumstance, such part of the integrand is a singular odd function on the segment. Therefore, its Cauchy's principal value is zero. The contribution of singularity has been already taken into account in the first term of Eqs. (11) and (13). This result has also been found by Kupradze [19]. In its scalar version, the result appeared first in a paper by Fredholm in 1900 [21].

2.2. Domain R

The ground motion in the region R is generated by waves refracted at S and at the interfaces of the layers. For the solution in the stratified medium, we combine Thomson–Haskell's propagator matrices ([22,23]) in the framework of a discrete wavenumber representation. In this way, the refracted field in the region R can be written as:

$$v^{(r)}(\mathbf{x}) = \sum_{m=-M}^{M} B_m l_1(k_m, z, \omega)\mathrm{e}^{-\mathrm{i}k_m x}, \tag{14}$$

where B_m are the unknown complex coefficients and $l_1(k_m, z, \omega)$ is the first element of the motion-stress vector for Love waves [24] for the horizontal discrete wavenumber k_m. The function $l_1(k_m, z, \omega)\mathrm{e}^{-\mathrm{i}k_m x}$ is solution of the 2D Helmholtz equation within the layered system. If, for example, we make

$$v(\mathbf{x}) = l_1(k, z, \omega)\mathrm{e}^{-\mathrm{i}kx} \tag{15}$$

and define the traction at horizontal planes as:

$$\mu\frac{\partial v}{\partial z} = l_2(k, z, \omega)\mathrm{e}^{-\mathrm{i}kx}, \tag{16}$$

where l_1 and l_2 are continuous functions of z. Then it can be shown Ref. [24] that, in a medium composed of horizontal homogeneous layers, the motion-stress vector at depth z can be written in terms of the propagator matrix and the motion-stress vector at depth z_0 as

$$\begin{bmatrix} l_1 \\ l_2 \end{bmatrix}_z = \mathbf{P}(z, z_0)\begin{bmatrix} l_1 \\ l_2 \end{bmatrix}_{z_0}. \tag{17}$$

The propagator matrix for a homogeneous medium is given by

$$\mathbf{P}(z, z_0) = \begin{bmatrix} \cos\eta(z - z_0) & (\eta\mu)^{-1}\sin\eta_j(z - z_0) \\ -\eta\mu\sin\eta_j(z - z_0) & \cos\eta(z - z_0) \end{bmatrix}, \tag{18}$$

where $\eta = \sqrt{\omega^2/\beta^2 - k^2}$.

From the repeated application of Eq. (17), if we assume that $z_0 = 0$ corresponds to the free surface, we have

$$\mathbf{P}(z, z_0) = \mathbf{P}(z, z_{j-1})\mathbf{P}(z_{j-1}, z_{j-2})\ldots\mathbf{P}(z_1, z_0), \tag{19}$$

for $z_j \geq z \geq z_{j-1}$ that is, for z in the jth stratum. The form of Eq. (19) guarantees satisfaction of continuity of stress and displacement between adjacent layers. To satisfy the boundary condition at the free surface, we make $l_2 = 0$ at $z = 0$. Without loss of generality, we can choose $l_1 = 1$ at the free surface.

The displacement is directly related to the first component of the motion-stress vector (see Eq. (15)), while the traction associated to a vector $\mathbf{n} = (n_x, n_z)^{\mathrm{T}}$, considering Eqs. (15) and (16), can be expressed as

$$t = \mu\frac{\partial v}{\partial \mathbf{n}} = \mu\left(\frac{\partial v}{\partial x}n_x + \frac{\partial v}{\partial z}n_z\right) = -\mathrm{i}\mu k l_1 n_x \mathrm{e}^{-\mathrm{i}kx} + l_2 n_z \mathrm{e}^{-\mathrm{i}kx}. \tag{20}$$

2.3. Coupling regions E and R

To guarantee perfect bonding between regions E and R we impose continuity of displacement and tractions, i.e.

$$v^{(\mathrm{r})} = v^{(0)} + v^{(\mathrm{d})} \tag{21}$$

at S, and

$$t^{(\mathrm{r})} = t^{(0)} + t^{(\mathrm{d})} \tag{22}$$

at S.

These conditions can be expressed for a point $\mathbf{x}$ on (the common interface) S by means of

$$\sum_{l=1}^{N} \phi_l g(\mathbf{x}, \xi_l) - \sum_{m=-M}^{M} B_m l_l(k_m, z, \omega)\mathrm{e}^{-\mathrm{i}k_m x} = -v^{(0)}(\mathbf{x}), \tag{23}$$

and

$$\sum_{l=1}^{N} \phi_l t(\mathbf{x}, \xi_l) + \sum_{m=-M}^{M} B_m(-\mathrm{i}\mu n_x l_l(k_m, z, \omega) + n_z l_2(k_m, z, \omega))\mathrm{e}^{-\mathrm{i}k_m x} = -t^{(0)}(\mathbf{x}), \tag{24}$$

respectively. If we impose these conditions on a set of points along the boundary S we can speak of a collocation scheme. Assume we chose $\mathbf{x} = (x_j, z_j)$, $j = 1, \ldots, N$, evenly distributed S. Then in order to obtain a square system of equation we set $N = 2M + 1$. It becomes clear that the total number of equations is $2N$ which is the same as the number of unknowns.

The choice of N is guided by the following considerations. In the region E it is convenient to have at least five elements per wavelength. This criterion comes from previous experiences using IBEM [7] and it is somewhat conservative. For shallow valleys one can approximately obtain $N > 5\eta$, where $\eta = (\omega a)/(\pi\beta_{\mathrm{E}})$ is the normalized frequency and a the half-width of the valley. If the sediments were to be treated with IBEM too, then an estimate of the lower bound for N in the layered region could be $N > 5\eta(\beta_{\mathrm{E}}/\beta_{\min})$, which, for valleys with very soft layers may produce very large N and this gives unnecessarily dense sampling for both the half-space and the valley. This statement is clear of one considers the global nature of the discrete wavenumber expansion which is given in terms of $\mathrm{e}^{\mathrm{i}k_m x}$. Moreover, it is convenient to assume that Δk is less than π/a, to avoid spurious periodicities, and that only homogeneous waves are allowed in the softer layer (this means $k_{\max} = \omega/\beta_{\min}$ and implies that inhomogeneous waves can exist in the other layers). Then, we have $M > \eta(\beta_{\mathrm{E}}/\beta_{\min})$, which gives $N > 2\eta(\beta_{\mathrm{E}}/\beta_{\min}) + 1$. Obviously, this value is less restrictive but still it can very easily dominate the choice of N. If the amount of allowed inhomogeneous waves in the softer layer is increased (this means $k_{\max} > \omega/\beta_{\min}$), N becomes larger.

For low frequencies, oversampling is not a serious problem. Actually, it is convenient and the solution is very stable. When frequency increases the different character of the involved representations requires care. A moderate amount of inhomogeneous waves may give good results for intermediate frequencies. Sometimes undersampling is a good solution. However, all this requires further scrutiny. The formulation for the P–SV waves case, would be part of another research.

3. Testing of the method

The accuracy of our approach is tested here using a solution that has been verified extensively [14]. These authors used direct boundary elements with the Green's function computed using the discrete wavenumber method. Their results have been tested by Ramos-Martinez [25] and Zahradnik [26], among others. Therefore, we regard these results as trustworthy.

Kawase and Aki [14] studied the trapezoidal valley shown in Fig. 2. Comparisons with their results are provided here for vertical incidence of plane SH waves. The model response is

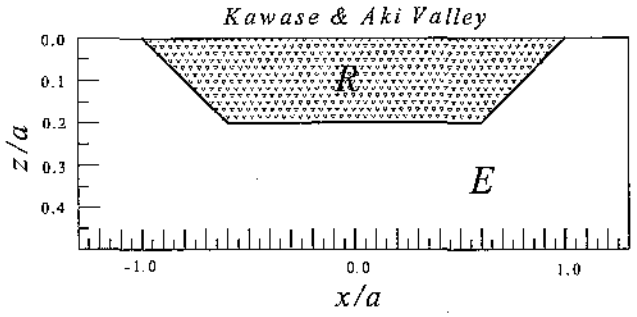

Fig. 2. Model studied by Kawase and Aki [14]. The regions E and R are shown and the coordinates are normalized in terms of the half-width $a = 5$ km. Incidence of harmonic SH waves. Material properties are given in the text.

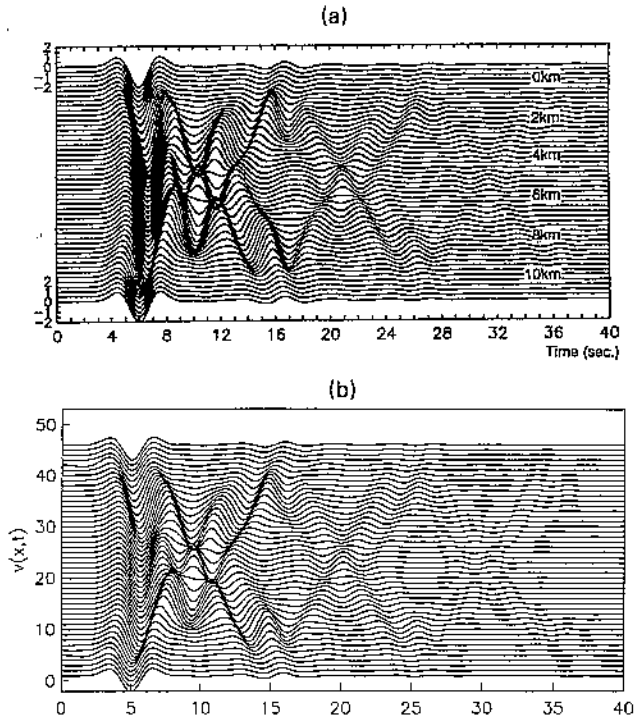

Fig. 3. Synthetic seismograms at the surface of Kawase and Aki's model [14] for vertical incidence of plane SH waves with time variation given by a Ricker pulse with characteristic period of 4 s. (a) Kawase and Aki [12] and (b) the presented approach.

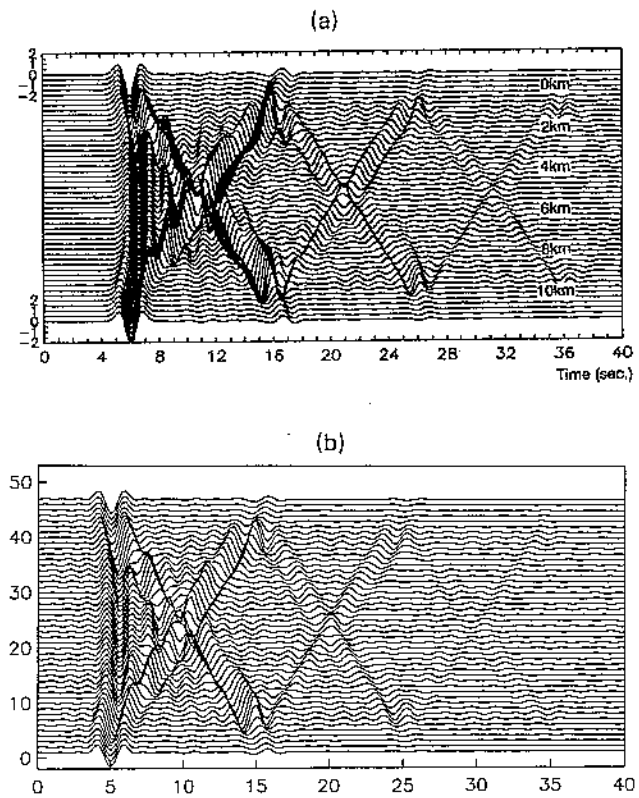

Fig. 4. Same as Fig. 3 but with characteristic period of 2 s.

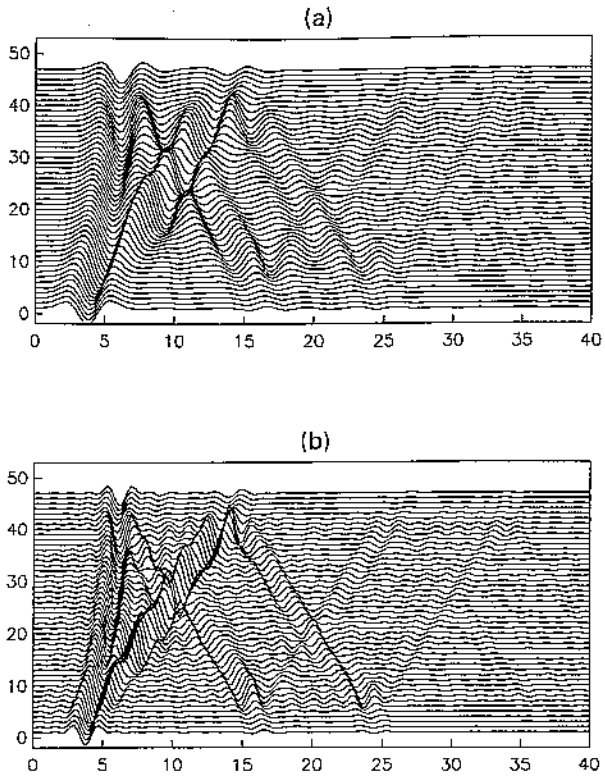

Fig. 5. Synthetic seismograms at the surface of Kawase and Aki's model [14], computed with the presented approach, for oblique incidence ($\gamma = 30°$) of plane SH waves with time variation given by a Ricker pulse with characteristic period of (a) 4 and (b) 2 s.

computed in frequency domain and the synthetic seismograms are computed using the FFT algorithm. It was assumed an incident Ricker wavelet. The comparison in time domain is a good test as many frequencies have to be computed and synthesized to provide the results. The synthetic seismograms obtained from both methods for vertical incidence are shown in Figs. 3 and 4 for characteristic periods $t_p = 4$ and 2 s, respectively. The agreement is excellent. We computed also the synthetics for an incidence angle of 30° with respect to the vertical and Fig. 5 shows the seismograms at the free

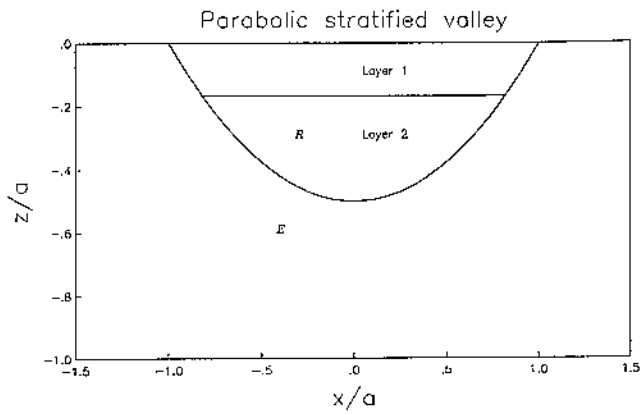

Fig. 6. Model studied by Bravo et al. [17]. Ratios of velocities of S waves and mass densities considered are: $\beta_1/\beta_E = 1/3$, $\beta_1/\beta_E = 2/3$ and $\rho_1/\rho_E = 3/4$, $\rho_2/\rho_E = 0.85$.

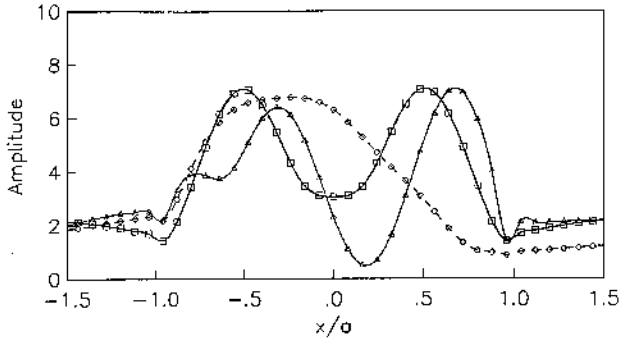

Fig. 7. Comparison of displacement amplitudes on the surface of the parabolic stratified deposit of Fig. 6. Normalized frequency is $\eta = 1.0$ and incident angles are $\gamma = 0$, 30 and 60°. Lines are for Bravo et al., and symbols are our approach.

surface for characteristic periods $t_p = 4$ and 2 s, respectively. These results clearly display the great significance of locally generated surface waves at the valley's edges.

We compared our approach also with the results by Bravo et al. [17]. These authors studied the response of a stratified parabolic deposit depicted in Fig. 6. Region R consists of two homogeneous strata, the top layer being 1. Maximum thickness are $H_1 = a/6$ and $H_2 = a/3$, where a is the half-width of the deposit. Shear-wave velocities and mass densities, referred to those of the half-space, are $\beta_1/\beta_E = 1/3$, $\beta_1/\beta_E = 2/3$ and $\rho_1/\rho_E = 3/4$, $\rho_2/\rho_E = 0.85$. Figs. 7 and 8 show the comparisons with their results.

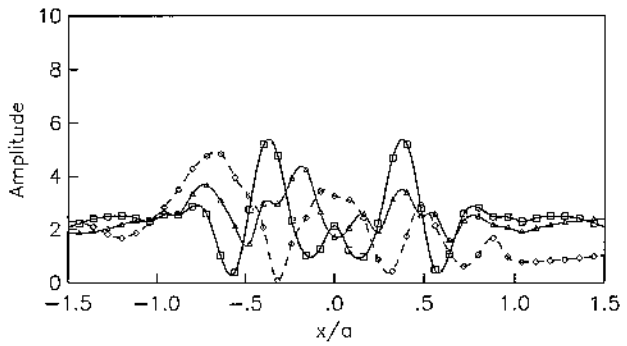

Fig. 8. Same as Fig. 7 but for a normalized frequency of $\eta = 1.0$.

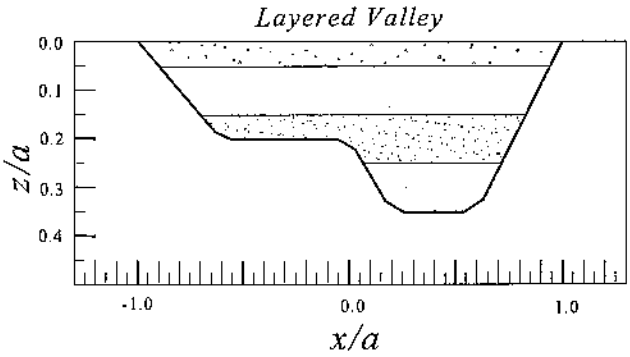

Fig. 9. Model of a layered valley. The coordinates are normalized in terms of the half-width $a = 1$ km. Incidence of harmonic SH waves. Material properties are given in the text.

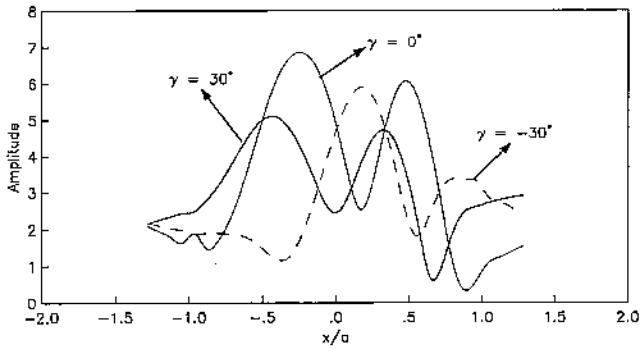

Fig. 10. Displacement amplitude at surface receivers at the layered valley along the x-axis for three incidences. Normalized frequency $\eta = 0.8$.

Three angles of incidence $\gamma = 0$, 30 and 60° were considered, and two normalized frequencies $\eta = 1.0$ and 2.0, respectively. The agreement is excellent.

4. Example

4.1. A layered soft deposit

In order to illustrate a complete set of results we analyze the response of a stratified valley with irregular interface for three incident angles in both frequency and time domains. The model is shown in Fig. 9. The half-width is of 1 km and

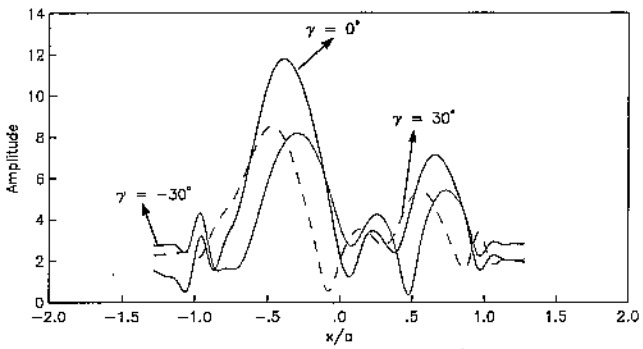

Fig. 11. Displacement amplitude at surface receivers at the layered valley along the x-axis for three incidences. Normalized frequency $\eta = 1.0$.

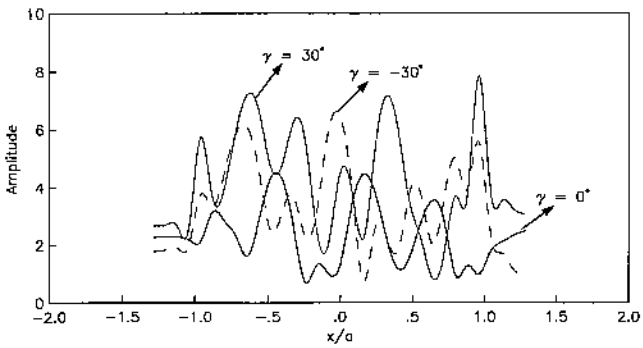

Fig. 12. Displacement amplitude at surface receivers at the layered valley along the x-axis for three incidences. Normalized frequency $\eta = 1.5$.

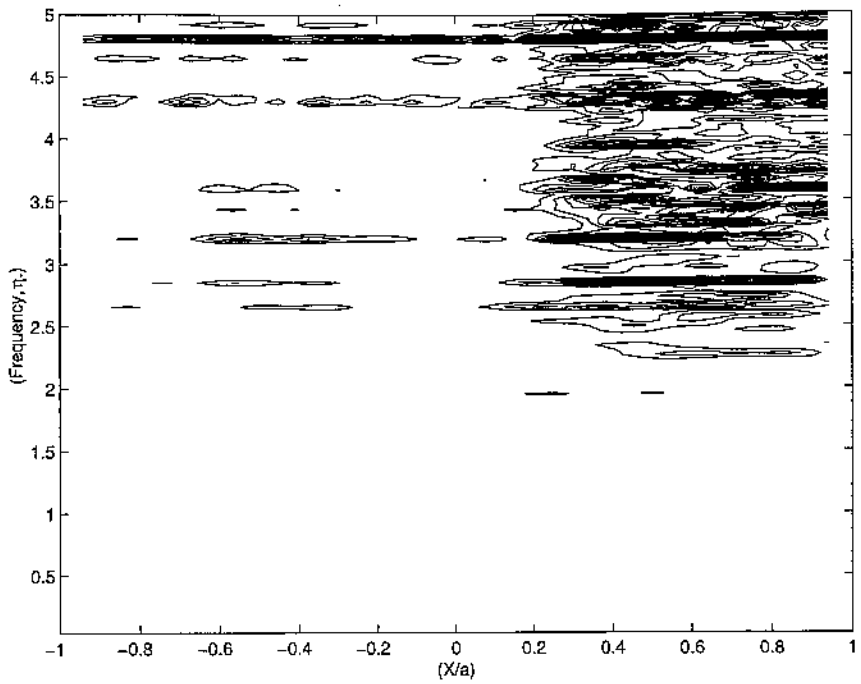

Fig. 13. Contours of displacement amplitude for surface receivers along the x-axis against frequency. Layered valley under vertical incidence of SH waves.

maximum depth is 0.35 km. The shear wave velocity assumed for the half-space is $\beta = 2$ km/s, while the velocities of the four layers, from top to bottom, are 0.8, 0.6, 1.0 and 1.2 km/s, the corresponding thicknesses of the four layers are 50, 100, 100 and 100 m, respectively, and the quality factor used are 50, 100, 150 and 200, respectively. Three angles of incidence $\gamma = 0$, 30 and $-30°$ were considered. Figs. 10–12 shows the surface displacement amplitudes for normalized frequencies $\eta = 0.8$, 1.0 and 1.5, respectively. Because of the properties of the model these frequencies have the same numerical value in Hz. The various plots clearly illustrate the spatial variation of amplification and the effect of incidence angle.

In order to give a clearer idea of the response, Figs. 13–15 show the contours of displacement amplitudes at surface receivers along the x-axis, between $x = -0.94$

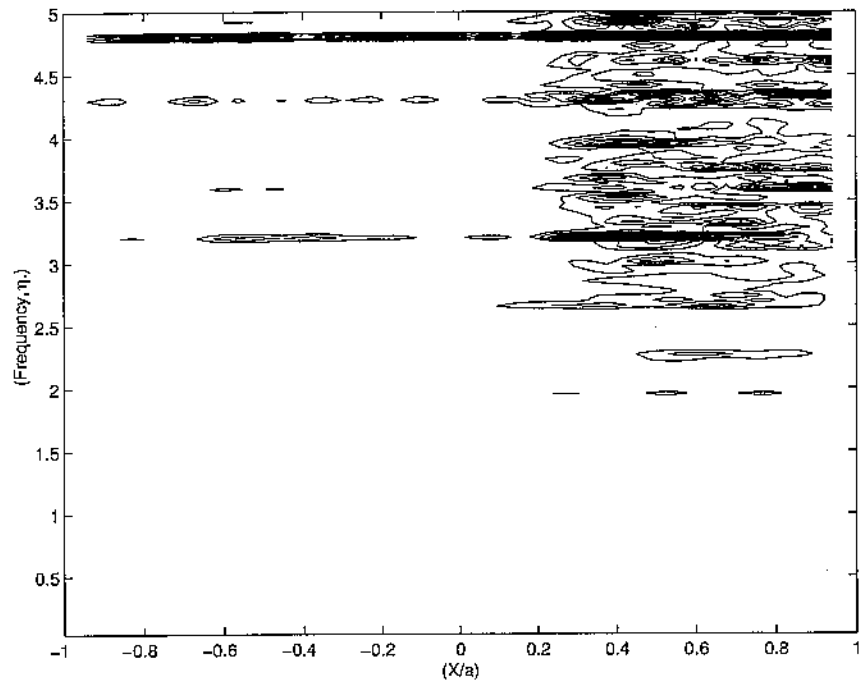

Fig. 14. Contours of displacement amplitude for surface receivers along the x-axis against frequency. Layered valley under oblique incidence ($\gamma = 30°$) of SH waves.

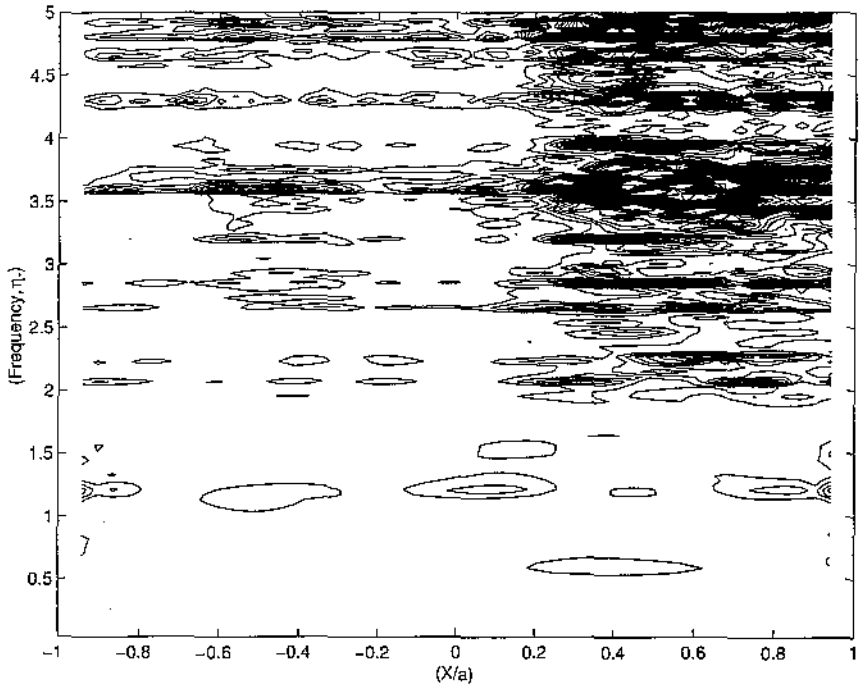

Fig. 15. Contours of displacement amplitude for surface receivers along the x-axis against frequency. Layered valley under oblique incidence ($\gamma = -30°$) of SH waves.

km and $x = 0.94$ km, against normalized frequency. These f–x diagrams display the transfer function (relative to the amplitude of incident waves) for all receivers and provide a good description of the frequency behavior of the valley. The plots also evince lateral resonances, which sometimes are clear when a series of peaks are distributed in space for a given frequency. This effect has been identified before [8]. The layering and the irregular profile tend to produce a complicated response. The resonant patterns vary with incidence angle. For instance, a resonant frequency of about 2.7 is clear for vertical incidence, but such a frequency is little excited by the oblique incidences.

The maximum value of displacement amplitudes is of about 12 for a frequency of about 1 Hz. This amplification, relative to the horizontal free-field surface displacement, is of about 6.5, nearly three times the average impedance ratio. On the other hand, the frequency is almost two times the 1D shear resonant frequency for a flat layer of the left side of the valley depth of 200 m). The same effects can be seen at the right side and can well be explained in terms increased stiffness due to lateral confinement. The 1D model gives surface amplitudes of about 4. Thus, we are led to interpret that the large amplification is associated to the lateral effects. These in turn, are due to focusing and to locally generated surface waves.

From frequency domain results we computed synthetic seismograms using the FFT algorithm for a Ricker wavelet with characteristic period of 3.3 s and vertical and oblique incidences (0, 30 and $-30°$). In Figs. 16–18 such time series are plotted for 49 receivers equally spaced between

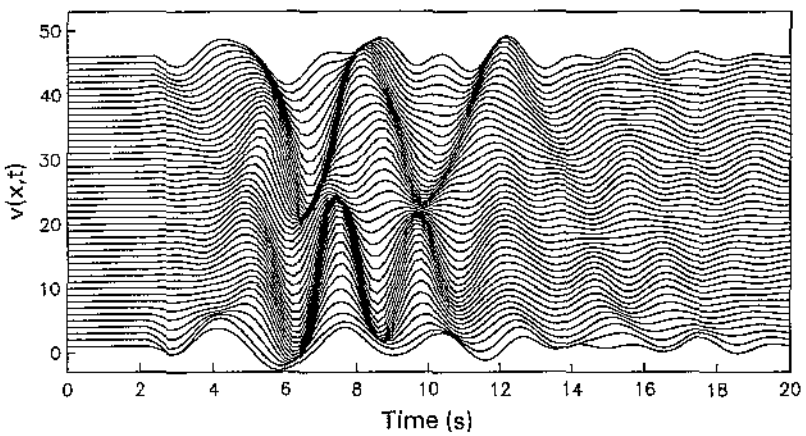

Fig. 16. Synthetic seismograms at the surface of the layered valley model, computed with the presented approach, for vertical incidence (γ=0°) of plane SH waves with time variation given by a Ricker pulse with characteristic period of 3.3 s.

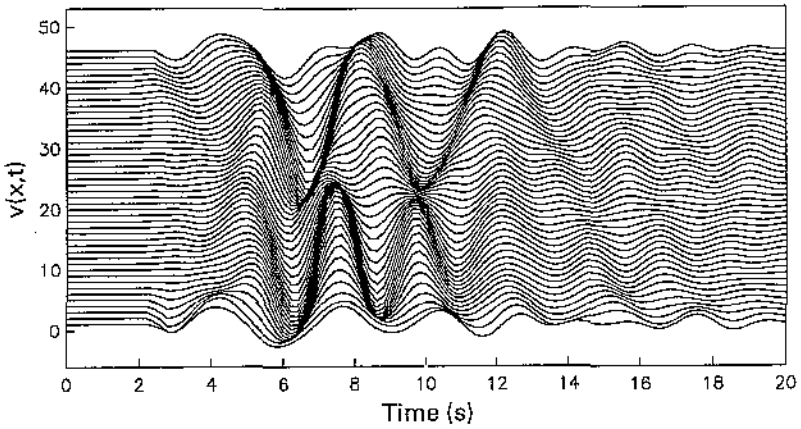

Fig. 17. Same as Fig. 13 but for oblique incidence ($\gamma = -30°$).

$x = -0.94$ km and $x = 0.94$ km. The amplification effect seen in the frequency domain is also clear in the synthetics. The traces show some 'ringing' which is probably due to errors in the computation of transfer functions and/or to the fact that we interpolated frequency response to obtain the synthetics.

5. Conclusions

A hybrid indirect boundary element-discrete wavenumber method has been presented and applied to study the seismic response of horizontally stratified alluvial valleys of arbitrary shape for incidence of plane SH waves. The method is based upon the integral representation of scattered and diffracted elastic waves at the half-space in terms of single layer boundary sources. For this IBEM approach, the Green's function was selected to be the one for the half-space and the discretization is restricted to the contact between the regions. For the stratified region the field is constructed using a set of solutions for homogeneous and inhomogeneous plane waves that correspond to horizontal discrete wavenumbers (DWN). These solutions satisfy all the boundary conditions at the layers interfaces and are obtained in terms of Thomson–Haskell propagators formalism.

While simple and intuitively appealing, this hybrid approach may suffer of some drawbacks and particular care is required from the analyst. The two approximations are different in character. On one hand, the IBEM description is local (we seek for local physical quantities: the force densities), on the other hand, the DWN linear superposition is global (the needed coefficients represent harmonic patterns). This may give rise to large differences in the entries of the coefficient matrix that results from the collocation scheme for boundary conditions, thus producing large rounding errors. By limiting the amount of allowed inhomogeneous wave and sampling the horizontal wavenumber domain in such a way that spatial periodicities less than $2a$ are avoided we may restrict the extent of numerical errors. This may result for some problems a kind of undersampling. In order to fully automate this procedure some more scrutiny is required.

Some examples are given for the response of simple models of stratified alluvial valleys in an elastic half-space. We confirmed the appearance of complicated patterns for surface displacements even in simple cases. In the examples the generation of Love surface waves can easily be seen.

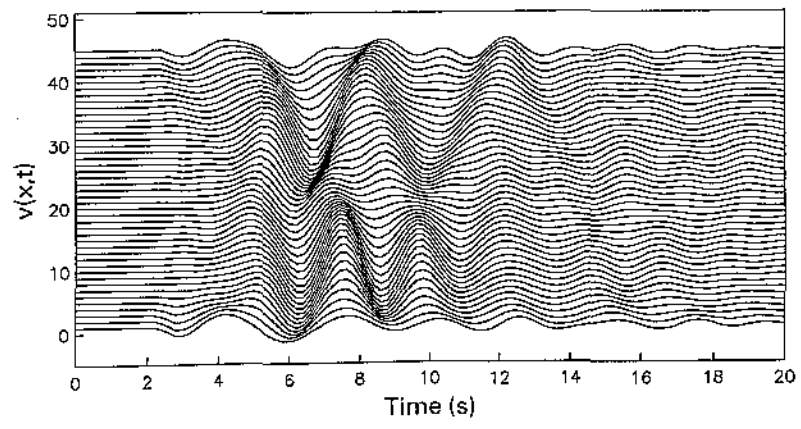

Fig. 18. Same as Fig. 13 but for oblique incidence ($\gamma = -30°$).

Synthetics for the irregular valley show a variety of complex patterns. Focusing of energy at low frequencies generally takes place at the deeper parts. Very large amplification was found in the sediments; more than three times the 1D prediction from the impedance contrast.

Our results suggest that variations in layer properties may produce important effects in the response. Strong impedance contrasts and the response at higher frequencies are among the issues that require attention.

The method is generally fast and accurate but it is not error-free and requires care from the analyst. Some more work is still needed for automatical choice of the calculation parameters.

Acknowledgements

We gratefully acknowledge the comments of two anonymous reviewers. Thanks are given to M. Ordaz and V.J. Palencia for their critical reviews and to M. Mucciarelli, F. Pacor, A. Mendez, for their comments and suggestions. This work was partially supported by ISMES SpA of Bergamo, Italy and by DGAPA-UNAM, Mexico, under project IN104998.

References

[1] Sánchez-Sesma FJ. Site effects on strong ground motion. Soil Dyn Earthquake Engng 1987;6:124–32.

[2] Aki K. Local site effects on strong ground motion in earthquake engineering and soil dynamics II. Recent advances. In: Von Thun JL, editor. Ground motion evaluation in geotechnical special publication, vol. 20. New York: American Society of Civil Engineers; 1988. p. 103–55.

[3] Sánchez-Sesma FJ. Strong ground motion and site effects. In: Beskos DE, Anagnostopoulos SA, editors. Computer analysis and design of earthquake resistant structures, Southampton: Computatinal Mechanics Publications; 1996.

[4] Manolis GD, Beskos DE. Boundary element methods in elastodynamics. London: Unwin Hyman Ltd; 1988.

[5] Beskos DE. Boundary element methods in dynamic analysis. Appl Mech Rev 1987;40:1–23.

[6] Beskos DE. Boundary element methods in dynamic analysis: Part II (1986–1996). Appl Mech Rev 1997;50:149–97.

[7] Sánchez-Sesma FJ, Campillo M. Difraction of P, SV Rayleigh waves by topographic features: a boundary integral formulation. Bull Seismol Soc Am 1991;81:2234–53.

[8] Sánchez-Sesma FJ, Ramos-Martínez J, Campillo M. An indirect boundary element method applied to simulate the seismic response of alluvial valleys for incident P, S and Rayleigh waves. Earthquake Engng Struct Dyn 1993;22:279–95.

[9] Sánchez-Sesma FJ, Luzón F. Seismic response of three-dimensional alluvial valleys for incident P, S and Rayleigh waves. Bull Seismol Soc Am 1995;85:269. see also p. 284.

[10] Aki K, Larner KL. Surface motion of a layered medium having an irregular interface due to incident plane SH waves. J Geophys Res 1970;75:1921–41.

[11] Bard P-Y, Bouchon M. The seismic response of sediment-filled valleys. Part 1. The case of incident SH waves. Bull Seismol Soc Am 1980;70:1263–86.

[12] Bard P-Y, Bouchon M. The seismic response of sediment-filled valleys. Part 2. The case of incident P and SV waves. Bull Seismol Soc Am 1980;70:1921–41.

[13] Bouchon M, Campillo M, Gaffet S. A boundary integral equation—discrete wavenumber representation method to study wave propagation in multilayered media having irregular interfaces. Geophysics 1989;54:1134–40.

[14] Kawase H, Aki K. A study on the response of a soft basin for incident. S, P and Rayleigh waves with special reference to the long duration observed in Mexico City. Bull Seismol Soc Am 1989;79:1361–82.

[15] Papageorgiou AS, Kim J. Study of the propagation and amplification of seismic waves in Caracas Valley with reference to the 29 July 1967 earthquake: SH waves. Bull Seismol Soc Am 1991;81: 2214–33.

[16] Kawase H. Time-domain response of a semicircular canyon for incident SV, P, and Rayleigh waves calculated by the discrete wavenumber boundary element method. Bull Seismol Soc Am 1988; 78:1415–37.

[17] Bravo MA, Sánchez-Sesma FJ, Chávez-García FJ. Ground motion on stratified alluvial deposits for incident SH waves. Bull Seismol Soc Am 1988;78:436–50.

[18] Abramowitz M, Stegun IA. Handbook of mathematical functions. New York: Dover; 1972.

[19] Kupradze VD. Dynamical problems in elasticity. In: Sneddon IN, Hill R, editors. Progress in solid mechanics, vol. III. Amsterdam: North Holland; 1963.

[20] Kouoh-Bille L, Sánchez-Sesma FJ, Wirgin A. Response resonante d'u'une montagne cylindrique a une onde sismique SH. CR Acad Sci Paris 1991;312(II):849–54.

[21] Webster AG. Partial differential equations in mathematical physics. New York: Dover; 1955.

[22] Thomson WT. Transmission of elastic waves through a stratified solid medium. J Appl Phys 1950;21:89–93.

[23] Haskell NA. Dispersion of surface waves on multilayered media. Bull Seismol Soc Am 1953;43:17–34.

[24] Aki K, Richards PG. Quantitative seismology. Theory and methods. San Francisco: W.H. Freeman; 1980.

[25] Ramos-Martínez J. Simulación numérica de la respuesta sísmica de valles aluviales. MSc Thesis, Institute of Geophysics, UNAM; 1992.

[26] Zahradnik J. Simple elastic finite-difference scheme. Bull Seismol Am 1995;85:1879–87.